# Influence of pressure on Leidenfrost effect

**Druckeinfluss auf den Leidenfrost-Effekt**
Zur Erlangung des akademischen Grades Doktor-Ingenieur (Dr.-Ing.)
genehmigte Dissertation von Dipl.-Wirtsch.-Ing. Ilja Buchmüller aus Togliatti
Juli 2014 — Darmstadt — D 17

TECHNISCHE
UNIVERSITÄT
DARMSTADT

Fachbereich Maschinenbau
Institute of Fluid Mechanics
and Aerodynamics
Spray group

Influence of pressure on Leidenfrost effect
Druckeinfluss auf den Leidenfrost-Effekt

Genehmigte Dissertation von Dipl.-Wirtsch.-Ing. Ilja Buchmüller aus Togliatti

1. Gutachten: Prof. Dr.-Ing. Cameron Tropea
2. Gutachten: Prof. Dr.-Ing. Peter Stephan
3. Gutachten: PD Dr.-Ing. Ilia V. Roisman

Tag der Einreichung: 5.5.2014
Tag der Prüfung: 1.7.2014

Darmstadt — D 17



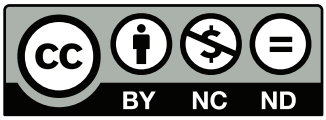

# Abstract

The Leidenfrost effect influences substantially the contact of a liquid droplet with a hot surface. Contact between the liquid and solid is crucial for cooling applications such as fire-fighting, hot-mill steel rolling, thermal power plants and microprocessor cooling. In automotive or aerospace internal combustion engines, the combustion chamber is pressurized prior to ignition. Despite various effects of elevated pressure, the combustion process needs to be controlled. The reaction time in a combustion chamber is limited, but mixture preparation involves prior evaporation. Fuel in contact with a combustion chamber wall evaporates in a uncontrolled manner. Furthermore, the fuel reacts with lubricants and decomposes into coke residue.

The fundamental physics of the Leidenfrost effect are yet to be fully understood. This applies especially to the influence of pressure on the Leidenfrost effect. For the question, if injected water droplets would stay in contact with the heated combustion chamber wall, current models would need to be extrapolated from ambient pressure, although there is no validation experiment available.

This experimental study addresses the influence of elevated pressure on the Leidenfrost effect, providing observations and measurements suitable to validate theories, hence extending the knowledge about the Leidenfrost effect. The experiment is implemented inside a pressure chamber and results for single water droplets impinging onto a hot aluminium substrate are presented. The droplet impingement Weber number was $5$. The experiments were conducted at chamber pressures from $1$ to $25$ bar ($0.1$ to $2.5$ MPa) and wall temperatures from $100$ to $460$ °C ($373$ to $733$ K).

Based on video observations, phenomenological boiling states are identified and mapped on a pressure-temperature diagram. The various states of impact behaviour shift to higher temperatures with increasing pressure. Nucleate boiling and critical temperature models of the bulk liquid serve as the lower and the upper bounds for the transition for all observed states of droplets, respectively.

A new nucleation model, accounting for the fluid flow inside the impacting droplet, agrees reasonably well with experimental results for the nucleate boiling in the experiment.

All previous theories and correlations predict transition temperatures which are constant or deviate from experimental values at elevated pressures. Therefore, the

theoretical part of this study tests refined hypotheses for transition from nucleate boiling to film boiling.

A Landau instability model and a bubble percolation model propose explanations for transitions in the boiling phenomena, but these models deviate from experimental results. Refinement of these approaches is still needed with respect to the characteristic length of instability and the active nucleation site count.

The experimentally observed onset of the transition state exhibits a linearity between the reduced pressure value and the reduced contact overheat.

The boiling states are further quantified with the measurement of the residence time upon the target. In the wetting state at ambient pressure, the residence time is equal to the evaporation time of the droplets. Residence time is lower for the transition and the Leidenfrost rebound states. The droplet detaches from the surface prior to complete evaporation.

Residence time thresholds mark the observed transition state. Asymptotic rebound time marks the rebound state. The time thresholds follow the state borders in the pressure-temperature map.

Secondary droplets are detected with the shadowgraph technique. Characterization of the secondary droplets has been achieved using a new image processing algorithm. It is based on the irradiance model of a semi infinite screen. The Sauter mean diameter of the secondary droplets in transition boiling state increases with increasing pressure. An increasing trend of the Sauter mean diameter of secondary droplets to the bubble departure diameter was observed.

# Zusammenfassung

Der Leidenfrost-Effekt beeinflusst substantiell den Kontakt eines flüssigen Tropfens mit einer heißen Oberfläche. Der Kontakt zwischen der Flüssigkeit und dem Feststoff ist entscheidend bei Kühlungsanwendungen, wie Feuerbekämpfung, Walzstahlproduktion, Wärmekraftanlagen und Mikroprozessorkühlung. In mobilen und stationären Verbrennungskraftmaschinen steht die Brennkammer kurz vor der Zündung unter Druck. Trotz verschiedener Effekte des erhöhten Drucks muss der Verbrennungsvorgang kontrolliert werden. Die Reaktionszeit in einer Brennkammer ist begrenzt, jedoch bezieht die Gemischaufbereitung die vorhergehende Verdampfung ein. Treibstoff, der an der Kammerwand haftet, verdampft unkontrolliert. Desweiteren reagiert der Treibstoff mit Schmierstoffen und verkokt bei Zersetzung.

Die grundlegende Physik des Leidenfrost-Effekts muss noch vollständig verstanden werden. Dies trifft insbesondere für den Druckeinfluss auf den Leidenfrost-Effekt zu. Für die Frage, ob bei einer Wassereinspritzung die Tropfen im Kontakt mit der geheizten Brennkammerwand bleiben würden, müssten die aktuellen Modelle vom Standarddruck ausgehend extrapoliert werden, auch wenn kein Validations-Experiment vorhanden ist.

Die experimentelle Untersuchung richtet sich auf den Einfluss des erhöhten Drucks auf den Leidenfrost-Effekt, liefert Beobachtungen und Messungen, die zur Theorie-Validierung geeignet sind, und erweitert somit das Wissen zum Leidenfrost-Effekt. Das Experiment ist in einer Hochdruckkammer implementiert, Ergebnisse für einzelne Wassertropfen, die auf ein heißes Substrat aufprallen, werden gezeigt. Die Weber-Zahl des Tropenaufpralls ist $5$. Die Experimente sind durchgeführt bei Kammerdrücken von $1$ bis $25$ bar ($0.1$ bis $2.5$ MPa) und Wandtemperaturen von $100$ bis $460$ °C ($373$ bis $733$ K).

Durch Videobeobachtung sind einige Abschnitte des Siedens phänomenologisch identifiziert und in einem Druck-Temperatur-Diagramm angeordnet. Die verschiedenen Siedeabschnitte verschieben sich zu höheren Temperaturen bei Druckzunahme. Modelle für das Blasensieden und die kritische Temperatur stellen die jeweils untere und obere Schranke für den Übergang für alle beobachteten Siedeabschnitte dar.

Ein neues Keimsiedemodell, mit Berücksichtigung der Strömung im Inneren des aufprallenden Tropfens, stimmt gut mit den experimentellen Ergebnissen zum Einsetzen des Keimsiedens überein.

Alle vorhergehenden Modelle und Korrelationen sagen Übergangstemperaturen, die mit Druckerhöhung konstant bleiben oder von den experimentellen Ergebnissen

abweichen, voraus. Deshalb werden im theoretischen Teil dieser Arbeit erweiterte Hypothesen für den Übergang vom Keimsieden zum Filmsieden getestet.

Ein Landau-Instabilität-Modell und ein Blasen-Perkolations-Modell schlagen Erklärungen der Übergänge der Siedephänomene vor, diese Modelle weichen jedoch aktuell von den Messungen ab. Eine Verfeinerung dieser Ansätze im Bezug auf charakteristische Länge der Instabilität und die Anzahl aktiver Siedekeime ist weiter notwendig.

Der experimentell beobachtete Beginn des Übergangsbereichs zeigt eine Linearität zwischen dem reduzierten Druck und der reduzierten Kontaktüberhitzung.

Die Siedeabschnitte sind zusätzlich quantifiziert mithilfe der Messung von Verweilzeit auf dem Ziel. Im benetzten Siedeabschnitt ist die Verweilzeit gleich der Verdampfungszeit, wie von anderen Autoren berichtet. Für den Übergangs- und den Leidenfrost-Abschnitt ist die Verweilzeit kürzer. Der Tropfen hebt vor der kompletten Verdampfung von der Oberfläche ab.

Verweilzeitschwellen grenzen den beobachteten Übergangsabschnitt ein. Die asymptotische Abprallzeit markiert den Abprall-Siedeabschnitt. Die Schwellen folgen den Abschnittsgrenzen im Druck-Temperatur-Diagramm.

Sekundäre Tropfen sind detektiert mit der Schattenaufnahme-Technik. Die Charakterisierung der Sekundärtropfen wurde mit einem neu entwickelten Bilderkennungsalgorhytmus erreicht. Dieser basiert auf dem Strahlungs-Intensitätsmodell einer semi-infiniten Blende. Der Sauter-Durchmesser der Sekundärtropfen im Übergangsabschnitt des Siedens erhöht sich bei wachsendem Druck. Steigender Trend des Sauter-Durchmessers der Sekundärtropfen zum wachsenden Blasendurchmesser wurde beobachtet.

# Erklärung zur Dissertation

Hiermit versichere ich, die vorliegende Dissertation ohne Hilfe Dritter nur mit den angegebenen Quellen und Hilfsmitteln angefertigt zu haben. Alle Stellen, die aus Quellen entnommen wurden, sind als solche kenntlich gemacht. Diese Arbeit hat in gleicher oder ähnlicher Form noch keiner Prüfungsbehörde vorgelegen.

Darmstadt, den 5. Mai 2014

(I. Buchmüller)

## Contents

# 1 Introduction

The behaviour of a water droplet, impinging on a metal surface heated above $250$ °C is in some respects counter-intuitive. For instance in the kitchen one could drop water onto a hot pan and observe the droplet rolling around with astonishing mobility, as long as the pan stays "hot enough".

When a droplet of water falls on a cool polished metal surface, it wets the surface. On the other hand, when the same surface is heated well above the Leidenfrost temperature of water, the droplet bounces off and floats above the polished metal surface without friction. The edges of the droplet become round and the surface is smoothed by the surface tension, as shown in figure 1.1. Here a water droplet with the diameter of $14$ mm is floating upon the aluminum surface with the temperature of $300$ °C ($573$ K) at ambient pressure. The droplet is centered by a copper ring, which is placed on top of the aluminium surface. The temperature of the ring is close to the temperature of the aluminum surface, therefore the ring is repelling the droplet in the same manner like the aluminum surface. With suitable geometry of the hot body, significant mass of liquid can be suspended in the floating state.

First recognized experiments on evaporation of droplets on a hot surface were carried out by *Leidenfrost* in $1756$, placing a water droplet on a red-hot iron spoon (Leidenfrost, 1756). In the Leidenfrost state, the water droplet is highly mobile on the heated metal, it has round edges and apparently does not wet the surface, furthermore the evaporation time of the droplet becomes very long, approximately $2$ minutes for a droplet with a diameter of $2.4$ mm.

The non-wetting is a frequent issue for both the bulk liquid and the impinging droplet systems. Engineers of heat exchangers need the fluid to stay in contact with the exchanger's wall. Fire fighters need to effectively cool down tanks to prevent Boiling Liquid Expanding Vapor Explosion (BLEVE) accidents. The hydrophobic state of water leads to explosions of boilers (Fairbairn, 1851) and other power equipment (Vakarelski et al., 2012) in industrial use. Many fluids, water being the most common example, experience such a change in wetting mode. Hence cooling effectiveness of droplets is limited if the temperature of the surface rises above, or pressure drops below, certain values.

When the surface temperature is higher than required for onset of nucleate boiling, the boiling heat transfer is stable and quite reliable (Mayinger, 1984). With evaporation of water, heat flux levels of $1$ MW/m$^2$ can be achieved at ambient pressure (VDI, 2010). But after reaching the critical value of surface temperature,

**Figure 1.1.:** A stationary Leidenfrost droplet on metal surface

boiling of bulk liquids becomes unstable in terms of fluid flux and with even higher temperatures boiling becomes unstable in terms of the insulating vapor layer.

Elevating the inside pressure of a boiling tank up to 100 bar is a widely used measure to mitigate the de-wetting of the heat exchangers (Mayinger, 1984), but even for bulk liquids the theory of boiling and bubble departure at different pressures is far from complete (Dhir et al., 2007).

Spraying droplets instead of pumping the bulk liquid is one of the typical means of heat transfer enhancement at high temperatures. Impacting droplets rise experience a dynamic pressure increase on impact, the momentum of the droplets enhances forced convection and the evaporation area of a spray is higher than of the bulk liquid.

In experimental investigations, the experimental change in temperature is often achieved by electrical heating, and most publications on droplets and the Leidenfrost effect investigate the temperature dependency at ambient pressure (Leidenfrost, 1756; Gottfried et al., 1966; Bernardin & Mudawar, 1999; Manzello & Yang, 2002; Gradeck et al., 2013). The pressure dependency of the droplet rebound effect is less studied. Investigations on boiling at different pressures are conducted with bulk liquids (Nukiyama, 1934; Kutateladze, 1979; Basu et al., 2002), without

considering droplets. The only known study on the Leidenfrost effect on droplets at different pressures was conducted with hydrocarbons (Temple-Pediani, 1969).

In general, the droplet wets the target surface at temperatures below the saturation temperature. Above a certain critical temperature no wetting is apparent. Both temperatures are affected by the surrounding pressure. The phenomena in the transition region between the two temperatures, under different given pressures, are the focus of the present study.

The experiments in this study are conducted under standard and elevated pressure. Droplet impacts are observed in order to detect the relevant parameters, including the size and velocity of the incoming droplets along with the temperature of the droplet and the metal plate prior to impact. Based on these observations, the interaction time of the droplet with the target surface is measured; results are documented over the entire range of pressures.

The case studied is suitable for a range of applications: fuel evaporation in combustion chambers of internal combustion engines, in combustion chambers of aircraft turbines, high-flux cooling in metal production, cooled microelectronics and heat exchangers.

The theoretical part of this study focuses on an analytical description of the phenomena in the droplet and the surrounding vapour. For different boiling stages known models from prior research on bulk liquids and ambient pressure are extrapolated and evolved.

For temporal measurements, the quantity residence time is introduced in the scope of this study. The residence time of a droplet upon the surface $t_{inc}$ is defined as the time during which the droplet is in the vicinity of the heated wall and there is no light passing through a possible gap between the wall and the droplet in the shadow image. The time is measured by counting of the corresponding images in the recording. The temporal resolution of the measurement is therefore $0.25$ ms with the maximal amount of steps equal to the maximal amount of images in the recording, $8184$ images. The temporal linearity of measurement is relying on the stability of the quartz time base of the high speed camera, estimated to have a $10^{-6}$ relative time error.

Residence time is different from the evaporation time of the droplet, which is used in cited publications, as the droplet may detach from the heated wall prior to complete evaporation, especially in the Leidenfrost state. In this case the residence time is the time of the first contact, while the evaporation time includes the time of flight of the droplet between the succeeding impacts and the time of floating above the heated wall on the macroscopic time scale of $0.5$ to $120$ s.

This thesis is organized in the following manner: Known publications and relevant approaches on the involved phenomena, namely water droplet impact, liquid-

wall interactions, nucleation, film boiling, involved characteristic scales and the expected influence of elevated pressure are reviewed in the next chapter.

In the third chapter, the experimental setup is presented with details on the implementation and uncertainty of the measurements.

Next, the observed results of the phenomenological boiling states are presented. Existing and new models are presented and discussed. Correlations of the measured state transitions and model predictions are shown.

In the fifth chapter, time measurements are shown and results on the residence time are provided for further quantification of the boiling states.

Characterization of secondary droplets is presented along with novel methods for image and data processing to characterize the secondary droplets in chapter six.

The results are summarized in the final chapter, providing also an outlook for future research.

# 2 Fundamentals and literature survey

## 2.1 Transient heat conduction

A contact of two finite bodies with only thermal conduction as a heat transfer mechanism can be modeled using the solution of two semi-infinite bodies (Baehr & Stephan, 2006b; Fourier, 1822). The temperature of the contact point $T_c$, shown in figure 2.1, is in this case time-independent.

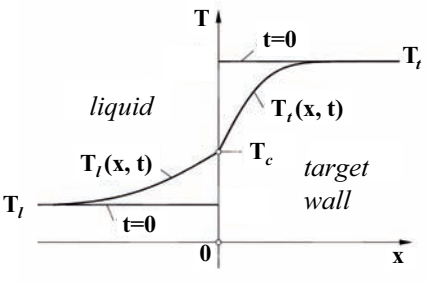


**Figure 2.1.:** Contact temperature of two semi-infinite bodies

The contact temperature is determined only by the initial temperatures of the liquid droplet and the target, $T_l$, $T_t$, and their thermal properties, expressed in the respective thermal effusivities $e = \sqrt{\kappa\, c\, \rho}$ where $\kappa$ is the thermal conductivity, $c$ is the specific heat capacity and $\rho$ is the density:

$$T_c = \frac{e_t\, T_t + e_l\, T_l}{e_t + e_l} \tag{2.1}$$

The contact temperature in equation (2.1) does not depend on the time elapsed after the contact initiation, as long as the bodies are "large enough" for the assumed semi-infiniteness to be valid. The expected value for the minimal duration of the

validity is about 100 ms for this experiment, estimated as in (Baehr & Stephan, 2006b, p. 169).

The highest temperature of the fluid in the semi-infinite body problem is the contact temperature, but experimentally, the target temperature before impact is measured, since the sensor influences the mesurement by itself. Equation (2.1) can be used to recalculate the target temperature measurements from experiments with different materials and initial liquid temperatures to the respective fluid contact temperatures, as remarked in chapter on communications of (Temple-Pediani, 1969) and in (Baumeister & Simon, 1973, eq. (27)).

If the target plate temperature is above the saturation temperature, but the initial contact temperature is below the saturation temperature, the metal surface will be wetted by the fluid and no boiling is expected at the first instance. While the heat propagates through the droplet, the contact temperature asymptotically rises up to the target temperature, since on a macroscopic time scale, the droplet is a small heat sink. Eventually, this may lead to boiling of the droplet.

Furthermore, if the temperature of the target is such, that the contact temperature is higher than the saturation temperature, the fluid becomes promptly overheated in the contact region, but still, vapor bubbles and boiling need nucleation.

## 2.2 Liquid-wall interaction with phase change

An assessment of theories on the Leidenfrost temperature at ambient pressure (LFP) (Bernardin & Mudawar, 1999) concludes that:

> *"The disagreement between the experimental LFP values and those predicted by the various models suggests that an accurate and robust theoretical model which effectively captures the LFP mechanisms is currently unavailable."*

The models evaluated in the assessment are the Taylor instability model, the metastable liquid model, the non-equilibrium model and the wettability model. All applied models, although using fitted coefficients, show differences to the experimental value of the Leidenfrost temperature, ranging from, $8$ K to $148$ K at ambient pressure. At different pressure levels, even larger deviations occur. The same authors report on refined models for the Leidenfrost temperature and spray cooling (Bernardin & Mudawar, 2002, 2004, 2007), although without considering elevated pressures. The complexity of the Leidenfrost effect is underlined in recent reviews (Yarin, 2005; Marengo et al., 2011; Quéré, 2013).

Typically, four heat transfer states are distinguished in an experiment on bulk liquid: convection, nucleate boiling, transition boiling and film boiling. The film boiling regime imposes limits on technical feasibility of high power evaporators and cooling devices. Experiments on horizontal heated wires submerged in a liquid were taken to explore the instable regime and introduced the concept of the boiling curve (Nukiyama, 1934), as shown in figure 2.2 (Mayinger, 1984).

Nucleate boiling consists of macroscopically visible bubbles which, with rising temperature of the wall, coagulate to form jets and columns. As the coagulated vapor bubbles obstruct the flow of cooling liquid, this behavior is named the flow crisis or the first heat transfer crisis (Mayinger, 1984). The inflection point in the figure 2.2 marks the beginning of obstructed flow. In this context, departure from nucleate boiling (DNB) is the second heat transfer crisis or boiling crisis, which takes place above a critical, i.e. maximal, heat flux.

The macroscopic instability and the hysteresis of this temperature region frequently impose technical problems with increasing temperature. Evaporative systems experience a drop in vapor generation performance. Heat exchangers become instable in temperature, thus overheating to the extent of destruction. Fluid cooling systems become ineffective. Even with decreasing temperature there are challenges in the instable region, as the evaporation rate rises, as soon the hot surface is re-wetted and nucleate boiling starts. Temperature stress on wall material increases, leading to distortions or cracks. More vapor mass is generated after re-wetting. Vapour expansion can also lead to an explosion, as in a steam vessel (Fairbairn,

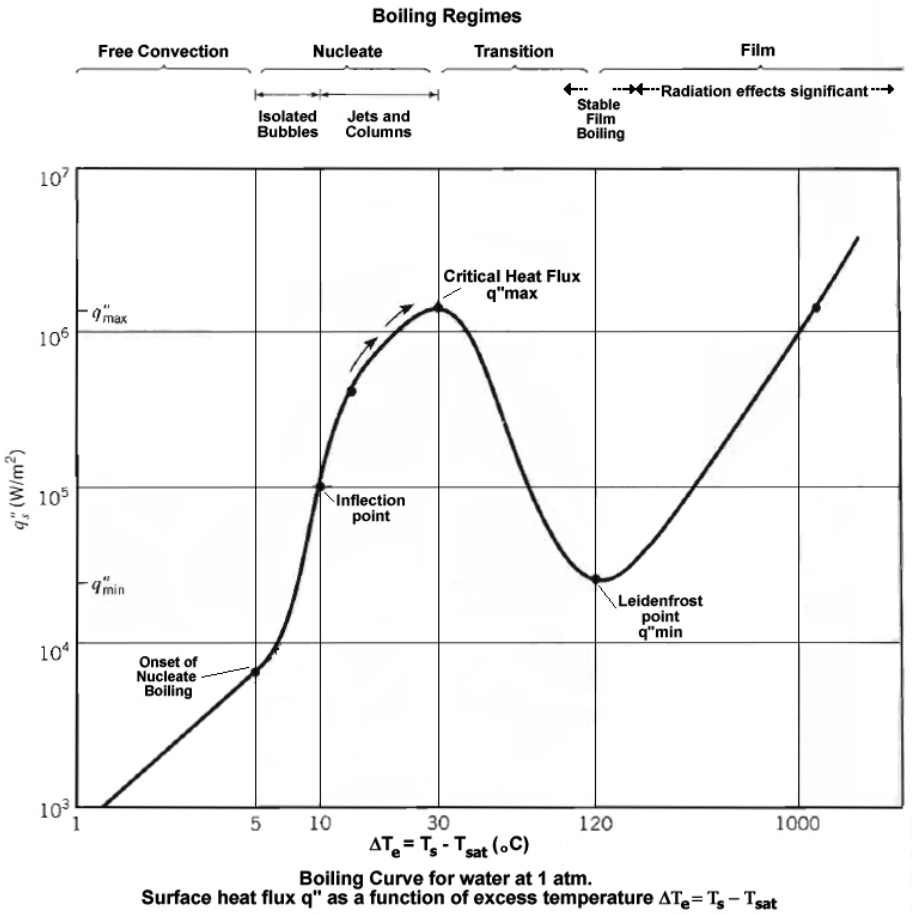


**Figure 2.2.:** Boiling curve of water (Mayinger, 1984)

1851) or a BLEVE event. Additionally, spreading of burning material may occur, as in water quenching of liquid hydrocarbon fires.

To quantify the Leidenfrost effect, usually a macroscopic variable, like the evaporation time of a single droplet is measured. This is done by observation and a stop watch, as in (Leidenfrost, 1966; Gottfried et al., 1966; Anokhina, 2010), or by reviewing of a video recording with a known time base, as in (Biance et al., 2003; Temple-Pediani, 1969).

Experiments are conducted sequentially with different initial wall temperatures and the evaporation time is plotted over temperature, as shown in following figure 2.3 (Takashima & Iida, 1998).

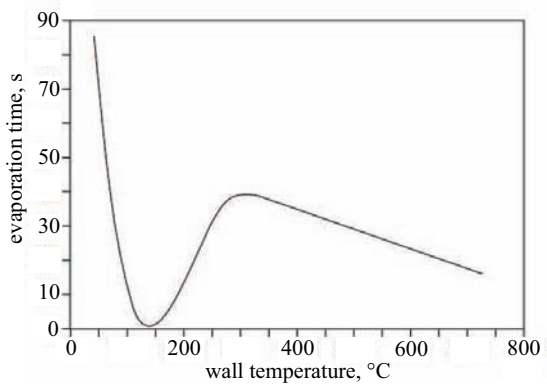


**Figure 2.3.:** Evaporation time of $2.5$ mm-diameter water droplets at ambient pressure (Takashima & Iida, 1998)

Steady-state evaporation of a droplet can only occur in a phase region where the liquid phase and the gas phase coexist. As shown on the phase diagram in figure 2.4, this is possible on the saturation line, between the triple point and the critical point of the fluid. In this study, the concept of equilibrium vapor pressure $p_{sat}$ at saturation temperature $T_{sat}$ is referred to as the saturation temperature hypothesis, $hS$.

At temperatures below the saturation temperature in the contact region, $hS$-line, no boiling phenomena are expected over any time scale. When the temperature of the fluid is above the $hS$-line, it is overheated, and evaporation can take place, for example on existing phase interfaces. If such interfaces are not existent or generated, liquids can persist in the meta-stable overheated state macroscopic amounts of time. The heat is stored in molecular vibrations and the molecules in the liquid phase are influenced by intra-molecular attraction forces. How a stable nucleus for a bubble and evaporation is possible, is discussed in section 2.2.1. Under certain conditions, bubbles form and evaporation takes place on the surface of the bubbles.

The phase diagrams and heat transfer phenomena of different fluids can be compared by the use of the extended principle of corresponding states (Shamsundar & Lienhard, 1993; Hederer et al., 1976). For this, the temperature and the pressure are divided by the respective critical values of the fluids. Heat transfer estimates can be made based on dimensionless correlations (VDI, 2010, pp. 761 ff.).

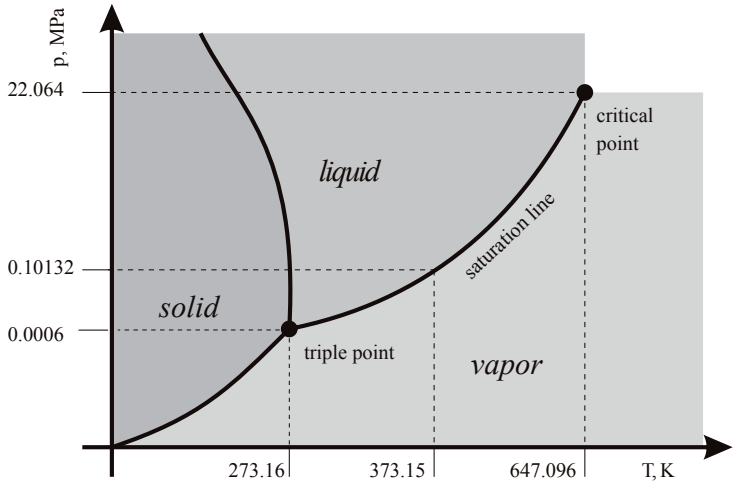


**Figure 2.4.:** $p$, $T$ phase diagram of water

While moving towards the target surface the droplet has approximately a spherical shape, because of the surface tension and capillary length of water. A small mass of vapor condenses on the sub-cooled droplet and it is heated through radiation from the target; both droplet non-sphericity and radiation are considered negligible in the scope of the present study.

### 2.2.1 Heterogeneous nucleation

Vapor can be created at either the existing free phase interface or inside a bulk liquid. The first evaporative effect is shown in the high-speed photograph in figure 2.5. Fluid molecules need energy to overcome intermolecular attraction on the surface, this energy is called latent heat of evaporation $h_{ev}$. At some distance from the droplet, the vapor cools down and re-condenses partially, generating traces of fog in the shadowgraph.

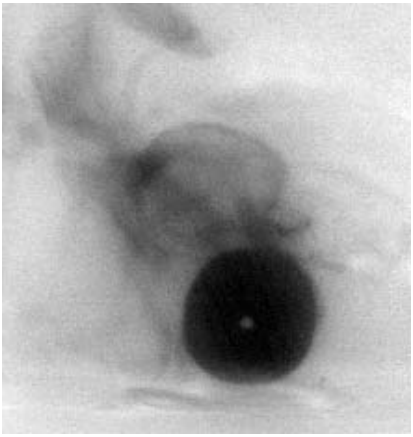

**Figure 2.5.:** Evaporation fumes after rebound at $p = 0.9$ MPa, $T_t = 623$ K

The second evaporative effect is triggered by nucleation, which is either homogeneous or heterogeneous. For both kinds of nucleation local overheat of the liquid above the saturation temperature is necessary(Baehr & Stephan, 2006b), otherwise a vapor nucleus cannot grow. A small vapor bubble of spherical shape at the ambient pressure $p$ has a higher inner pressure $p_i$ due to the surface tension at the bubble surface. The pressure difference $\Delta p_{Y-L}$ is called the *Laplace pressure* and can be expressed with the *Young-Laplace* equation:

$$\Delta p_{Y-L} = p_i - p = \sigma \left(\frac{1}{R_1} + \frac{1}{R_2}\right) = \frac{2\sigma}{R_1}, \tag{2.2}$$

where $R_1 = R_2$ are the radii of the spherical interface.

A homogeneous nucleus of water has an estimated size of $4000$ molecules (Lienhard & Karimi, 1981). Having a diameter of estimated $3$ nm, the nucleus has to

overcome an inner pressure estimated as more than $4$ MPa. A bubble can continue to grow only if the local temperature of the liquid phase is above the corresponding saturation temperature by the amount of $\Delta T_{Y-L}$, which is derived from equation (2.2) with the *Clausius-Clapeyron* equation for vapor (Baehr & Stephan, 2006b, eq. (4.82)), using latent heat of evaporation $h_{ev}$, density of vapor $\rho_v$ and the fluid saturation temperature $T_{sat}$:

$$\Delta T_{Y-L} = T - T_{sat} = \frac{2\sigma T_{sat}}{R_1 \rho_v h_{ev}} \tag{2.3}$$

In equations (2.2) and (2.3) the bubble radius $R_1$ has either to be measured or deduced. Equation (2.3) can be solved for $R_1$ if $\Delta T_{Y-L}$ is known. The value of the bubble radius is also an estimate of the vapor hemisphere radius above a nucleation site.

The saturation temperature $T_{sat}$ is pressure dependent. In the experiment the pressure is measured at the chamber wall. The pressure of the liquid in the droplet is slightly higher in accordance to equation (2.2). This overpressure for a water droplet with the diameter of $2.4$ mm is approximately $120$ Pa.

On real surfaces depressions are present which, after macroscopic wetting during impact, can host nanometer-sized bubbles of entrapped gas and vapor. When a cavity's geometry is suitable for the specific range of hemisphere sizes for a given temperature, the corresponding nucleation site becomes active and serves as a starting point for chains of bubbles.

Further analysis of heterogeneous nucleation is carried out with the help of the approach shown by *Hsu*, where a thermal boundary layer with a constant temperature gradient is considered (Hsu, 1962). The bubble radius is related to the distance of the bubble tip from the hot wall and the coldest point in the surrounding fluid, which will be touched if the cavity of that particular size is filled with vapor and activated (Basu et al., 2002). This model is a good tool for investigations on structured heat exchangers. However, it introduces the thermal boundary layer thickness as a parameter, the measurement of which inside a moving droplet is very difficult and quite uncertain in accuracy. It should be noted that this thickness is reported to be influenced by the fluid motion and the flow velocity at the surface of the droplet. A good overview of the knowledge about heterogeneous nucleation sites and further assumptions are given in (Basu et al., 2002).

The correlations based on Hsu's criterion generally underestimate the superheat value for the beginning of nucleate boiling, as remarked in (Basu et al., 2002). The main reason for this underestimation is the absence of cavities in the assumed place due to limited droplet contact area. This is accounted for in chapter 4.2.1.1. The

point, when these conditions are met and boiling starts, is called onset of nucleate boiling (ONB).

### 2.2.2 Homogeneous nucleation

For homogeneous nucleation the radius $R_1$, which is assumed to be within the range of thermal fluctuations, can be modelled with kinetic theory. The statistical approach of *Lienhard* in (Lienhard & Karimi, 1981) accounts for the probability of a thermal fluctuation leading to a small vapor bubble. The concept is empirically supported by experiments on pulse heated wire filaments in (Skripov et al., 1980).

If thermal vibration of molecules leads to a nucleation event, homogeneous nucleation takes place. This vibration must generate a stable nucleus by pushing aside neighbour molecules, before this fluctuation is dissipated during the relaxation time. The typical relaxation time is estimated to $10$ subsequent collisions. Geometrical considerations lead to a probability $j_n \leq 2 \times 10^{-5}$ events/collisions, above which nucleation is noticed macroscopically. The criterium for homogeneous nucleation is according to (Lienhard et al., 1986, eq. (15)) dependent only on known fluid properties:

$$-ln(2 \times 10^{-5}) = 10.8 = \frac{16\ \pi\ \sigma^3}{3(k\ T_{crit})(p_{sat} - p)^2(1 - \rho_v/\rho_l)^2} \tag{2.4}$$

where $\rho_v$ and $\rho_l$ are the equilibrium densities of vapor and liquid at local pressure $p$, respectively, $T_{crit}$ is the critical temperature of the fluid, $k$ is the Boltzmann constant and $p_{sat}$ is the equilibrium saturation vapor pressure at the local temperature.

Homogeneous nucleation dictates a maximal overheat temperature applicable for the bulk liquid, above which it would lose its stability and start evaporating at nucleation sites within itself. As the initial stable size of the nucleus is estimated to consist of 4000 molecules (Lienhard & Karimi, 1981), with the size of $\approx 3$ nm, the superheat effect of non-occurrence of potentially suitable fluctuations is negligible for droplets of sizes above $1$ $\mu$m, as in this experiment.

The nucleation criterion is equal to the spinodal line equation (2.5), within an accuracy of $1$ K in (Lienhard et al., 1986, fig. 6), and therefore homogeneous nucleation for boiling can be calculated by the spinodal line equation. In a $p$, $T$ diagram, one can mark the instability region for the bulk liquid by spinodal lines using reduced temperatures as in (Lienhard et al., 1986, eq. (18))

$$\underline{T}_{hom} = (T_c - T_{sat})/T_{crit} = (0.923 - T_{sat}/T_{crit} + 0.077(T_{sat}/T_{crit})^9) \tag{2.5}$$

This equation has a pressure dependency through the fluid properties of water in $T_{sat}$. The thermal properties of the target surface are accounted through $T_c$ as per

equation (2.1). Equation (2.5) is shown as $hH$-line in the discussion of the results as comparison of the impact of homogeneous nucleation on the boiling phenomena of a droplet.

If the contact temperature of the droplet is above saturation temperature by a threshold, corresponding to nucleation, then the droplet is expected to boil at the active nucleation sites. The growing vapor bubbles are expected to interact with the fluid flow in the droplet, as they penetrate the liquid phase. After traveling through the liquid, the bubbles collapse, releasing the vapor. At this state, generation of secondary droplets is expected, induced by the collapsing bubble lamellas. With rising temperatures, a transition of the multiple separated bubbles to a connected singular vapor layer could cause the macroscopic appearance of a levitated droplet and the Leidenfrost effect.

### 2.2.3 Film boiling

At temperatures above DNB and the transition state, the fluid is separated from the solid with a thin film of vapor, therefore this state is depicted film boiling regime in experiments on bulk liquids. This state is considered equivalent to the Leidenfrost state for the experiments on droplets. The droplets float on the thin vapor layer and become spheroidally shaped due to surface tension.

Due to numerous investigations on water droplets and the Leidenfrost regime, there are different definitions of the Leidenfrost temperature and accordingly, different criteria marking the effect, so care should be taken, when comparing results, as the criteria may not be the same.

Heat flux measurements in the Leidenfrost regime are reported in (Anokhina, 2010) for bulk water heated by wires or cylinders, along a comparison to water droplets. A local maximum in heat flux marks the departure from nucleate boiling at ambient pressure with a heat flux of $1.1$ MW/m$^2$ at $125$ °C, i.e. at $398$ K.

The local minimum in heat flux of $0.6$ MW/m$^2$ marks the onset of film boiling at $141$ °C, i.e. at $414$ K. The onset of film boiling is attributed to the Leidenfrost effect, it can be quantified by the temperature which corresponds to droplets adopting a spherical shape in (Anokhina, 2010). Measurements of non-stationary heat fluxes to droplets, although quite difficult in implementation, are being realized due to the availability of fast thermal imaging technology, like in (Chatzikyriakou et al., 2011). These measurements reveal short-term heat extraction as high as $4$ MW/m$^2$ in the first two milliseconds of droplet impact.

In a recent review, *Quéré* uses a sharp rise in evaporation time of a droplet as the criterion for a critical temperature, which is then called Leidenfrost temperature (Quéré, 2013). For a water droplet with the size of $1$ mm this temperature is approximately $145$ °C, i.e. $418$ K.

Several authors use the temperature with a local maximum of the droplet's evaporation time as the Leidenfrost temperature, as the droplet can then be readily observed. Different values are reported here, starting with $100$ s at $150$ °C, i.e. $423$ K, for water droplets with the diameter of $1$ mm in (Biance et al., 2003). A local maximum temperature of $423$ K is reported in (Baumeister & Simon, 1973). The local maximum of the evaporation time is $128$ s for a $51$ mg droplet at $270$ °C (Anokhina, 2010). The droplet diameter of such a droplet would be $4.6$ mm, the temperature would correspond to $543$ K.

The evaporation time for a $2.7$ mm water droplet is reported to have a local maximum of $60$ s at $330$ °C, i.e. at $603$ K (Manzello & Yang, 2002).

*Leidenfrost's* definition of the effect is the lowest temperature of the hot polished iron surface for a non-adhering of a water droplet resulting in the high mobility of the droplet over the surface (Leidenfrost, 1966). A red glowing spoon heated over coal and passively cooled in air was used. This corresponds to a temperature of $500$ to $800$ K. The same mobility is encountered in (Chatzikyriakou et al., 2011) at approximately $220$ °C, i.e. at $493$ K.

The ability of the vapor to generate a layer that is capable of suspending the droplet could be considered as an alternative criterion for a model. In the approach of *Gottfried*, the Leidenfrost temperature is defined as the lowest temperature with sustainable film boiling. The evaporation time for water droplets of $3.9$ mm size is then near the local maximum, as seen in (Gottfried et al., 1966), approximately $90$ s at $280$ °C, i.e. at $553$ K.

The maximum droplet evaporation time is a macroscopic quantity which corresponds to the Leidenfrost temperature. The measurements cited above were taken at ambient pressure only. In the fifth chapter, reported temperatures for characteristic evaporation times are taken as a reference for temperatures of characteristic residence times in the experiment at ambient pressure setting. The characteristic temperature values in the experiment are marked with phenomenological observations and quantified with residence time measurements by high-speed imaging.

There is evidence that the variation of thermal properties of the fluid and the target materials change the wall temperature at Leidenfrost point, see the chapter on communications in (Temple-Pediani, 1969). Local cooling of the glowing spoon is also observed as a visible dark region at the landing spot of the droplet (Leidenfrost, 1966). This indicates the existence of a short conductive fluid-to-solid contact as induced by the effect of a water hammer (Engel, 1955). In such a scenario, the contact temperature $T_c$ from equation (2.1) for iron with initial temperature of $1073$ K, and water of $293$ K, is $1015$ K, leading to an intensity change in $25\%$ of radiation energy for a black body. Such a intensity change of light could be noticed by observation. On the other hand, as the penetration depth of heat conduction in iron at the time scale of $0.1$ s is $4$ mm, the thickness of the spoon

material may be too small to support $T_c$ under the assumption of semi-infiniteness, and the temperature change could be perceivable without conductive heat transfer taking place.

The Leidenfrost temperature is reported to be sensitive to the surface finish of the target, if polished, particle blasted or rough sanded (Bernardin et al., 1996).

The arithmetic average surface roughness of $0.09$, $0.97$ and $2.96$ $\mu$m, according to the surface preparation mentioned before, is accompanied with surface features of the size of $1$, $5$ and $15$ $\mu$m, respectively, as revealed by scanning electron microscope (SEM) images in (Bernardin et al., 1996). Therefore a vapor layer of magnitude of $1$ $\mu$m will be needed in the experiment of this study for the vapor layer to effectively insulate the fluid from the solid. This can only occur, when the vapor layer is thick enough from being protruded by the vertices on the solid surface and being destabilized. A similar value for the vapor thickness during droplet impact is reported in (Tran et al., 2012).

Within the scope of this investigation, the residence time of the droplet upon the hot target is measured. Thus, the evaporation time minima are quantified and compared with reported values. Phenomenologically, non-wetting behavior of the droplets above certain temperatures at given pressures is observed. The beginning of such a boiling state is corresponding with the local maximum of the evaporation time and is used as the criterion for the Leidenfrost temperature in this study.

## 2.3 Droplet impact

A theory describing droplet impact, as illustrated in figure 2.6, is known (Yarin, 2005; Roisman, 2009; Tran et al., 2013). For the purpose of this study, the expression for the spread diameter of the droplets is utilized.

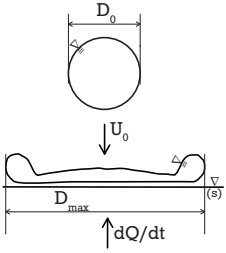


**Figure 2.6.**: Spreading droplet

The impact phenomenon is mainly governed by the initial diameter of the droplet $D_0$, the impact velocity $U_0$, the surface tension $\sigma$, the dynamic viscosity $\mu$, the density $\rho_l$ and the wettability of the solid surface, represented by the equilibrium contact angle $\theta_e$. These parameters can be grouped into the Weber and the Reynolds number given by:

$$We = \frac{\rho_l D_0 U_0^2}{\sigma};\ Re = \frac{\rho_l D_0 U_0}{\mu} \tag{2.6}$$

For a water droplet with the initial size $D_0 = 2.4$ mm and a free fall height of $7.7$ mm with acceleration of $1\ g$, the impact velocity, $We$ and $Re$ are about $0.39$ m/s, $5$ and $950$ respectively. For the typical parameters of the present experiment, the drop does not splash.

Numerous studies have been carried out to examine the maximum spread ratio (Li et al., 2010; Roisman et al., 2002). For a low-viscosity fluid like water the expected maximum spread diameter at room temperature and pressure for the inertial governed spread phase is calculated as (Roisman, 2009, eq. (42))

$$D_{max} = D_0(0.87Re^{1/5} - 0.40Re^{2/5}We^{-1/2}) \tag{2.7}$$

Similar maximum spread ratios are reported for different fluids (Yarin, 2005). This leads to the size estimation for the heated plate and for the optical access windows in designing of the present experiment.

The dynamic pressure on the symmetry axis of droplet impact is created due to the change in the direction of liquid motion. This pressure adds to the chamber pressure, so that the local pressure for the liquid is increased during impact. The dynamic pressure, $p_q$, (Spurk & Aksel, 2007, p. 359) is

$$p_q = \frac{1}{2}\,\rho_l\,U_0^2 \tag{2.8}$$

and with the typical values of the experiment $p_q = 76$ Pa. This pressure is by design relatively small in this experiment, but in a typical spray cooling device with increased impact velocity the dynamic pressure can be significant for technical use.

For the interaction time of the droplet with the hot wall in the rebound regime, the splashing, spreading and receding phases of the droplet impact can be modeled and agree with experimental results. Interaction of water droplets at low Weber number with a hydrophobic wax surface endures from $5$ to $20$ characteristic time scales (Roisman et al., 2002). With the experimental time scale of $6$ ms in the present experiment, the rebound time of the droplet is estimated from $30$ to $120$ ms.

Heat conduction during droplet impact is enhanced due to forced fluid convection in the near-wall boundary layer (Roisman, 2010a):

$$T_c = \frac{\mathfrak{F}(Pr,\Xi,\xi)\;e_t\;T_t + e_l\;T_l}{\mathfrak{F}(Pr,\Xi,\xi)\;e_t + e_l} \tag{2.9}$$

where $\mathfrak{F}(Pr,\Xi,\xi)$ is a function of $Pr$, the material dependent Prandtl number of the droplet, $\Xi$ the scaled position of the phase transition front, and $\xi$ the dimensionless similarity ratio of spreading droplet thickness to the viscous length (Roisman, 2010a, eq. (3.6, 4.13)).

According to this equation, the contact temperature at the impact point is generally closer to the initial temperature of the droplet, the initial temperature of the wall need to be higher for ONB. For the typical parameters of the present experiment in the contact region, $Pr \approx 1.6$ at $p = 0.1$ MPa and $Pr \approx 0.85$ at $p = 2.5$ MPa. $\Xi = 0$ indicates the position in liquid directly at the wall surface. Under the assumption of small viscous length in comparison to the droplet thickness of estimated $0.5$ mm, the similarity ratio $\xi \to \infty$. $\mathfrak{F}(1,0,\infty) \approx 0.63$, cooling is thus enhanced by the fluid flow in the droplet. At saturation temperature the Prandtl number decreases with increasing pressure. Therefore droplet cooling is enhanced further and the spread between the target temperature and the contact temperature increases with increasing pressure.

## 2.4 Characteristic scales

The measurements of figure 2.3 are performed on a macroscopic time scale, with time from $0.1$ to $90$ s. To gain further insight into the process, a visualization with high-speed imaging is used. A water droplet takes from $30$ to $120$ ms to complete the rebound after impact upon a hydrophobic target. The temporal resolution of the imaging with the frame rate of $4000$ frames per second permits the details of the rebound process to be directly observed.

Droplet impact on the wall induces different phenomena, such as hydrodynamic pressure hammer, bubble entrapment of vapor and ambient gases, along with acoustic waves inside and outside the droplet. The potential significance and duration of these effects are discussed below.

The maximal additional local pressure caused by the water hammer effect, $\Delta p$, can be estimated by the equation

$$\Delta p = \Delta u \rho_l a_l \tag{2.10}$$

where $\Delta u$ is the velocity change, $\rho_l$ is the liquid density and $a_l$ is the speed of sound in liquid (Spurk & Aksel, 2007). The estimated result is $\Delta p \approx 0.58$ MPa, however the compressibility of the metal target is neglected. A collision of two elastic infinite bodies leads to a pressure estimate

$$\Delta p = \frac{\Delta u \rho_l a_l}{1 + \frac{\rho_l a_l}{\rho_s a_s}} \tag{2.11}$$

where $\Delta u$ is the velocity change, $\rho_l$, $\rho_s$ are the liquid and solid densities, $a_l$, $a_s$ are the speed of sound in the liquid and the solid, respectively (Haller, 1933). This estimation gives a typical value of $0.53$ MPa for the water hammer pressure in this setup.

The duration of the pressure surge for water hammer is on the scale of acoustic effects and can be expected in the order of $0.1$ $\mu$s, further analysis of the impingement process leads to a local pressure rise time of 40 ns and an adjusted pressure with a factor of $0.9/2$ to account for spherical droplet geometry (Engel, 1955). The details of water hammer effect cannot be resolved with the available temporal resolution.

The $10$ ns time scale is regarded as the minimal physically justified time scale for the fluid-wall interaction. With a frame rate of $4000$ frames per second, our present high-speed imaging equipment is expected to be able to capture particularly the translations of the fluid-vapour interface of the droplets, which are slower by some orders of magnitude than the acoustic effects.

For the upper length one can refer to the maximal droplet spread diameter during droplet impact shown in equation (2.7), which is approximately $5$ mm. The size of the target plate is chosen to be $25\ \mathrm{mm} \times 25\ \mathrm{mm}$. The dimensions of the plate allow to observe multiple rebounds of the droplets at high temperatures and reduce the alignment effort.

For the lower length scale there are small secondary droplets, which are produced by vigorous boiling, and simultaneously the dynamic vapor film thickness, which is smaller than $10$ $\mu$m (Biance et al., 2011), as compared to several $100$ $\mu$m at stationary conditions (Quéré, 2013).

Therefore, the lower spatial limit of the measurements can be arbitrary small and is governed by the available measurement technology.

As gas and vapor densities during droplet impact are orders of magnitude smaller than the densities of the fluid and solid, the entrapped gases are considered pressed into the cavities and nucleation sites of the target surface, which are available due to surface roughness.

The influence of gravity on a spherical droplet is proportional to its volume, the influence of surface tension is proportional to its surface. Of the two influences surface tension becomes dominant, if the droplet diameter is smaller than a critical length. This length is the capillary length $L_{cap}$

$$L_{cap} = \sqrt{\frac{\sigma}{\rho_l\ g}} \approx 2.5\ \mathrm{mm} \tag{2.12}$$

assuming $\rho_l \gg \rho_v$.

Gravity can be neglected, if the droplet radius is smaller than $L_{cap}$ (Quéré, 2013). The length scales for the radius of the water droplet in the experiment, along the characteristic size of lamellas, bubbles and rims is five times lower than the capillary length. Furthermore, the direction of the gravity vector does not play a major role during droplet impact and droplet deformation.

## 2.5 Expected influence of elevated pressure

The main influence of ambient pressure on the heat transfer in a boiling system is considered to be the shift in saturation temperature of the vapor, as predicted by the *Clausius-Clapeyron* equation, see also (Habchi, 2010). For n-heptane and other fuel components, more information is available (Temple-Pediani, 1969), here also a decrease in the maximum droplet lifetime, near the Leidenfrost temperature, is reported with increasing pressure. Furthermore, an increase of the minimum droplet lifetime near DNB with increasing pressure is shown (Temple-Pediani, 1969, detail of fig. 2).

The disappearance of the Leidenfrost effect is also recorded in hydrocarbon fluids at pressures above the critical pressure in (Temple-Pediani, 1969), as there is no phase boundary. The persistent transition to non-wetting is expected in the current experiment, as the critical pressure of water $p_{crit} = 22.064$ MPa at $T_{crit} = 647.096$ K (Baehr & Stephan, 2006b) is well above the pressure in the current study.

Changes in ambient pressure also lead to slightly different material properties of the liquid phase (IAPWS, 2007; VDI, 2010). In this experiment, vapor density increases linearly with pressure and changes by a factor of $\approx 25$. This has an impact on the inertia forces and the heat transfer in the vapor. Therefore, in the theoretical section, all quantities are regarded depending on local temperature and pressure (Kretzschmar et al., 2013), except otherwise noted.

The main distinction of the present setup to other published experiments is the variation of the different values of the boiling, nucleation and Leidenfrost temperatures by changing only the pressure in the experimental chamber. Although the pressure effect on fuel hydrocarbons was investigated in (Temple-Pediani, 1969), this was never investigated for water.

The reported temperature values for the Leidenfrost effect are taken at ambient pressure. The influence of pressure is not considered in known reports on Leidenfrost effect (Baumeister & Simon, 1973), or is included implicitly by saturation temperature, critical temperature, spinodal line or vapor density. If any non-modelled physical process or a non-fitted experimental parameter plays a major role in the transition to nucleate boiling, deviations of theoretical predictions from experimental results are expected with increasing chamber pressure. Hence the experiments performed here provide novel data for hypothesis testing.

## 2.6 Aim of the study

The ambient pressure has a significant influence on the evaporation rate of an impinging droplet because it changes the saturation vapor temperature of the fluid and the density of generated vapor. Therefore, it affects many aspects of boiling like boiling temperature, Leidenfrost temperature, thickness of the vapor layer in stationary levitation, along with the dynamics of the impact, heat transfer rates and parameters of the secondary spray. This study investigates the transition to the de-wetting state at different chamber pressures.

The goal of this study is to conduct experimental work and to investigate the implications of elevated pressure on the boiling phenomenon of an impacting water droplet.

Fluid spray cooling involves many scientific fields such as fluid atomization, droplet generation, interaction of droplets in flight, impingement phenomena, evaporation and boiling, along with splashing and secondary droplet generation. Previous studies have revealed complex interaction of droplets forming pools and films upon impact (Roisman et al., 2007), which masks the possibility to look inside the boiling process. A detailed study of all the effects simultaneously would extend beyond the scope of the present research project. The idea of this study is to concentrate on the evaporation phenomenon, accessing single droplet impact.

Thus, the purpose of this work is to consider an abridged case of spray cooling and of the introduction of water in a combustion chamber: A single, nearly spherical droplet of water falls a short distance in air at the pressure from $0.1$ to $2.5$ MPa and impinges onto a flat metal target, which is heated to induce boiling.

This study focuses on the influence of pressure as this influence is not covered by any studies to date.

The long-term aim of the research is to develop comprehensive models of drop impact with phase change under extreme, i.e. non-equilibrium, conditions.

# 3 Experimental setup

The experimental setup comprises the pressure chamber, as shown in figure 3.1, the droplet generation section, the heated target, an optical shadowgraph system and the data acquisition system.

**Figure 3.1.:** Pressure chamber on the support structure

The key components of the experiment, as shown in the figure 3.2, are assembled inside the pressure chamber. A piezoelectric pump and a blunt hydrophobic needle are used as a droplet generation device. This droplet generation principle was chosen after in-depth research, as it proved to be convenient to integrate into the pressure chamber. Droplet detachment is induced by pumping under gravitational forces. Measurement and optical systems are synchronized to the detachment of the droplet with a reflective light barrier. The trigger signal is initiated through an FPGA (field programmable gate array) based measurement system, which incorporates a 100 ms PID temperature controller and data monitoring functions. An Ultramic600 heater from Watlow with an integrated type K thermocouple is placed

under the aluminum (AL99.5-alloy) target plate, whose thickness is $3$ mm. The target surface is polished with corundum abrasive paper with a decrease in the grit size from P100 to P360, alongside corundum polishing paste to provide a mirror-like appearance. While polishing, in the middle of the target plate the abrasive paper was pressed with approximately $1$ N additional force to induce a depression of $\approx 0.1$ mm. The curvature is to stabilize the rebound of the droplets enabling the possibility to capture multiple rebounds at high temperatures.

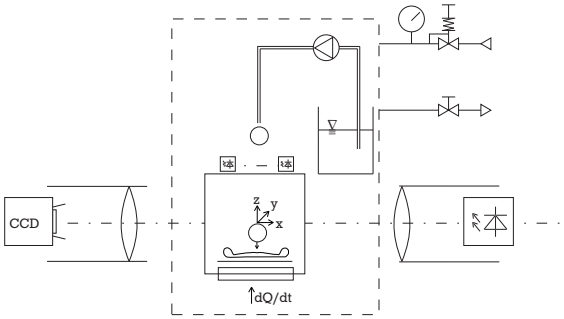


**Figure 3.2.:** Schematic diagram of the setup

Pressure is recorded on a pressure chamber port, relative to the ambient pressure of the laboratory, which is obtained from a nearby weather station. The absolute uncertainty in pressure is $60$ hPa ($0.06$ bar). The pressure of the liquid in the droplet is slightly higher than the pressure at the chamber port in accordance to equation (2.2), due to surface tension and in accordance to equation (2.8). These pressure differences are approximately $1.2$ hPa and $76$ Pa, respectively, their effect is accounted in the pressure measurement uncertainty.

A high-speed shadowgraph optic system is implemented, with stratified low coherence blue LED illumination. The pulse duration is $300$ ns, synchronized with the high-speed camera at $4000$ frames/s. The focal length of the camera lens is $300$ mm. The pixel size at the object plane is $43.4 \pm 0.2$ $\mu$m according to calibration pictures.

The contact temperature is accessed indirectly. Equation (2.1) is solved for the target temperature. In that way, the contact temperature is recalculated into the corresponding temperature of the target plate, which can be set prior to the particular impact.

The temperature sensor is placed in the heater, the target plate is adhering to it with a liquid metal thermal conductor. The distance between the sensor and the

wall surface is approximately $d_t = 4$ mm, so there is a question, if the assumption of small temperature differences inside the heater package is valid.

For estimation of the temperature gradients before the droplet impact, the one-dimensional stationary heat conduction inside the heated heater package is considered (Baehr & Stephan, 2006b, eq. (1.8))

$$\dot{Q} = \frac{\kappa_t A_t}{d_t}(T_{sensor} - T_t) \tag{3.1}$$

where $\dot{Q}$, $\kappa_t$, $A_t$, $d_t$ and $T_{sensor}$ are the heating power, the thermal conductivity of the target package, the area of the heated target package, the sensor-to-surface distance and temperature at the sensor, respectively.

The temperature difference $(T_{sensor} - T_t)$ represents the systematically underrated temperature error because of $d_t > 0$. The lowest thermal conductivity of the materials in the heater package is that of aluminium nitride in the heater, so $\kappa_t = 70$ W/(m K) is assumed. The surface area of the heater package is calculated from the dimensions of $25.4 \times 25.4 \times 10$ mm. The typical maximal heating power in stationary temperature control at $p = 2.4$ MPa and $T_t = 733$ K setting is 5 % of full power, i. e. $\dot{Q} = 48$ W. With rearranged equation (3.1) the sensor temperature offset

$$(T_{sensor} - T_t) = \frac{\dot{Q}\, d_t}{\kappa_t\, A_t} \tag{3.2}$$

has a maximal value of $(T_{sensor} - T_t) = 1.2$ K. In the following calculations $T_{sensor} = T_t$ is assumed.

Calculation of the residence time is conducted through the counting of the frames from the first to the last frame showing no gap between the droplet and the target wall. The maximum measured time is limited to 2 s by the available memory and the resolution is limited to $0.25$ ms by the frame rate.

In the Leidenfrost state, the vapor layer thickness during impact is smaller than in the stationary case (Kunkelmann, 2010) and is smaller than the optical pixel size at the object plane. But the inertia of the droplet causes it to rebound from the wall, when wetting and surface attraction between the droplet and the wall are weak, within $40$ ms in a typical droplet impact with similar $We$ number (Roisman et al., 2002). The optical resolution permits the detection of a gap wider than $87$ $\mu$m. The travel time of the droplet at $v_0$ for this distance is $0.22$ ms. The measurement of the residence time effectively includes this amount of time on impact and a similar amount of time on the departure of the droplet from the wall.

Characterization of the secondary droplets from high-speed records is conducted by a newly developed image processing method. Starting from the raw image, the

first image in the record containing the empty scenery just before arrival of a new droplet is subtracted. To homogenize the illumination, the difference image is filtered spatially. For each filtered image the droplets are recognized with a threshold function, based on the irradiance function of a semi-infinite screen. Finally, statistics concerning the size of the detected droplets are compiled according to the area equivalent diameter of the droplets.

## 3.1 High pressure chamber

In the pressure chamber, an experimental insert, specific to the experiment is designed and implemented. This insert carries the heater assembly, the thermal sensors, the droplet generator and the ventilation of the optical windows.

The relevant pressure range for the experiment is derived from the typical conditions of a combustion chamber. This is required in the scenario of injection of water or a water-fuel suspension into the combustion chamber. The evaporation of typical fuel components is accessed in (Temple-Pediani, 1969), but this data is not suitable for water, as its material properties cannot be extrapolated from hydrocarbons.

Depending on the design of an engine, different mixture conditions are possible at fuel injection. Pressure of $0.7$ MPa is stated in (Habchi, 2010), $1.2$ MPa is reported in (Stanglmaier et al., 2002), $2$ MPa is reported for a turbo-charged diesel engine prior ignition in (Mollenhauer & Tschöke, 2010) and $2.4$ MPa is shown in the combustion chamber of an aircraft turbine engine in (Royce, 1996). Therefore, the pressures chosen for the experiment range from $0.1$ MPa to $2.5$ MPa, corresponding to reduced pressure range from $0.0045$ to $0.11$ of water.

## 3.2 Droplet generation

In the process of conception of the experiment several droplet generation techniques were tested and implemented. This chapter shows the results of the tests and the reasons which led to the construction of the particular droplet generator in this setup. This information is provided to help the following experimental studies in the choice of a suitable droplet generation technique.

Different principles of droplet-on-demand (DOD) generation have been reviewed, including bubble-jet, piezoelectric, acoustic, pneumatic, aerodynamic, microfluidic and needle dripping principles (Ashgriz, 2011, pp. 581 ff.).

In the bubble-jet device, a heater in a capillary receives an electrical impulse, heating a portion of the fluid in the pipe. The fluid evaporates and the vapor bubble pushes a portion of the fluid out of the capillary, generating a small jet, which in flight constitutes of a group of droplets. In time the heat from the impulse diffuses out of the vapor, it condenses causing the bubbles to collapse. During the collapse of the bubble, capillary forces drag the replenishment load of fluid in a typical device. Bubble-jet droplet generators are in wide use in commercial printers of Hewlett-Packard and Canon. Such a printhead was considered as a droplet generator for the experiment and tested.

For printing, solvent-dye mixtures with manufacturer-proprietary recipes are used. Flushing the dye and refilling of a cartridge with water, although it is feasible and tedious, doesn't ensure that the generated droplets are free of impurities of the dye or printhead's materials. The dye solutions seem to have corrosion inhibitors. The performance of a refilled printer cartridge deteriorates on daily basis after refilling, the printhead heater has a tendency to corrode.

The printhead was operated successfully with impulse voltages up to $24$ V. The duration and the energy of the electrical impulse is important to correlate with the volume of the evaporated fluid in the capillary. After the bubble is formed, it insulates the heater from the rest of the cartridge, entrapping the excessive heating energy within the heater. Due to the heat load, one extended impulse can impair the corresponding channel of the printhead. The temperature of the generated droplets is influenced by the heating, thus making it necessary to use a sensor to monitor the temperature of the incoming droplets between the nozzle and the print head heater. It's assumed, that the Leidenfrost effect and dry-out takes place repeatedly inside the bubble-jet droplet generator prior to any experiment. The typical impulse duration is $10$ $\mu$s. Variation of the droplet size is possible with different pulse energies in the working range of the print head. The droplet size is coupled with the droplet velocity. Satellite droplet formation occurs at high pulse energy. The typical droplet size ranges from $10$ to $100$ $\mu$m for dye droplets.

Further variation of droplet size could be possible with reconstruction of the print head. A custom construction of a bubble-jet DOD device would require a construction of a small heater with lithographic technology.

Due to the uncertainty in the details of the influence of the heater on the fluid and the disadvantages in usability of the bubble-jet print heat, when used with clean water, this type of DOD device was not considered for the present experiment.

In piezoelectric devices, a pulsation in fluid pressure is induced by a piezoelectric active membrane, by a translational stack or by a contracting pipe. The displaced volume of the fluid forms a jet out of the nozzle, which by surface tension forms droplets in flight. Commercial print heads of Epson use this working principle. A custom constructed droplet generator was considered for the experiment and tested (Li, 2013).

If the fluid is actively driven through the piezoelectric head by the means of a pump or external pressure, a continuous jet is formed by the nozzle. This jet can be modulated by a small-amplitude signal to produce droplet chains with a narrow size distribution, (Brenn et al., 1996). Depending on the pumping rate, the device can be used as DOD generator, droplet chain or water jet generator.

For alteration of droplet size, the orifice in the front part of the device is exchanged. The orifices are available from scientific suppliers in the form of metal optical pinholes, but can also be laser-drilled.

Acoustic droplet generators resemble the working principle of the piezoelectric generator. The pressure variation is made by a concentrated sound impulse. The aforementioned realization of a piezoelectric DOD generator is more compact and flexible, than a loudspeaker-based design.

In pneumatic droplet generators the pressure impulse is generated by a short-time opening of a pressurized gas supply valve of a tuned Helmholtz-type cavity. Realization of a pneumatic DOD generator is cumbersome inside the pressure chamber, as the gas supply needs to be maintained at constant pressure difference to ensure stable operation.

Aerodynamic droplet generation is achieved by pumping a small droplet at the end of a capillary and detaching it by a coaxial air pulse. For the first step a medic dosage pump is typically used. The air flow pulse needs to be strong enough to trigger detachment, but also small enough not to disintegrate the droplet during acceleration. For this working principle, the air supply is sensitive for pressure differences, imposing difficulties, when pressure in the chamber is varied.

A microfluidic droplet generator uses coaxial capillary flows for non-miscible fluids. To generate a droplet on the tip, the first fluid is pumped into a capillary. A coaxial flow of the second fluid detaches and further transports the droplet. This working principle produces controlled emulsions and can be set up to generate droplets with shells (Seo et al., 2007), but for the reason of high difference in the

density of water and air it is not suitable for generating droplets flying in a directed manner.

As variation of droplet sizes and velocities adds dimensions to the study, and an investigation on these variations is published (Bernardin et al., 1997), this study concentrates on the pressure variations, keeping the droplet parameters constant.

Needle dripping operating principle requires the least adaption to setup inside the high pressure chamber. It is robust to the changes in surrounding pressure. Contamination and additional heating of the liquid are not taking place. Therefore, this type of DOD generation is chosen in the present experiment. The piezoelectric dosage pump is actuated electrically from outside. A blunt medical needle with outer diameter of $0.4$ mm, which has a hydrophobic tip coating, is used as a droplet generation device. Detachment of individual droplets is triggered by gravitational forces.

## 3.3 Synchronization

The measurement and optical systems are synchronized with the detachment of the droplet by the use of a reflective light barrier of the type VTR17D1H from Vactec. The output from the light barrier is fed into the FPGA as an analogue channel. The threshold comparison initiates a TTL (transistor-transistor logic) $5$ V compatible output, which triggers the start of the high-speed recording at the high speed camera. The cameras software allows for setting a delay for triggering, so a delay of $47$ ms was used to account for the flight time of the droplet outside the field of view. The high-speed camera has a TTL output which indicates camera exposure time. This signal is fed to the stroboscope unit to trigger the illumination. For each frame, this signal goes to a positive state at the beginning of camera detector matrix exposure. With a delay of less than $15$ ns the stroboscope starts to illuminate the scene. The duration of effective exposure is set by the stroboscope settings, i.e. by the duration of illumination, the shutter duration setting of the high-speed camera is higher. At the typical frame rate of $4000$ frames per second, the camera is no longer influenced by day light. The actual duration of the illumination can be checked by a fast photodiode connected to an oscilloscope. A green indicator LED (light emitting diode) serves this purpose. An oscilloscope of the type Tektronix TDS2004C was used to check the timings of the trigger signals.

## 3.4 Measurement and protocol system

The measurement systems incorporate a $100$ ms PID temperature controller and mean value calculation for the monitored temperatures on the FPGA level; hence the data monitoring functions on the micro-controller level receive less noise. This is important for the temperature sensor channels dealing with low-level voltages. The sample rate is reduced from $20$ kHz to $20$ Hz.

Pressure was recorded relative to the ambient pressure of the laboratory by the WIKA A-10 sensor type 12719316, s/n 11039MRA. This sensor has a manufacturer calibrated accuracy of $0.14$ % of the $4$ MPa range, yielding an uncertainty of $56$ hPa. The ambient pressure is measured by a nearby weather station and varied during the experiments within an interval of $2$ hPa. Together with the overpressure of $1.2$ hPa induced by surface tension of the droplet, the absolute uncertainty in pressure is estimated to be $60$ hPa ($0.06$ bar).

The humidity of the air inside the pressure chamber is measured by a dew point sensor. The air in the chamber is mixed by the air curtain on the optical windows and by the structure cooling fan of the heater assembly, so a homogeneous humidity is assumed inside the chamber. The dew point of the pressurized air in the chamber is $-47$ °C. The dew point is relatively low, as the air is dried at the pressure supply station of the laboratory.

For low-delay, closed-loop control of the heater, the temperature needs to be sensed at a rate above 10 Hz. That excludes many available measurement modules, therefore a custom temperature sensing is implemented. This also allows for a flexible programming of the PID control loop, which was extended with safety functions like disengage at broken sensor or manual disable.

The structure of the experiment in the chamber is continuously cooled by a radiator with a fan to ensure stability even during a major overheating of the heater package in case of malfunction in the heater control.

Temperature measurements use type K, i.e. NiCr-Ni thermocouples. One thermocouple is integrated into the heater, a second thermocouple was used to monitor the water temperature in the droplet generator. Thermocouples generate a voltage according to the temperature difference between the measured point and the reference cold junction. As the cold junction is not at the reference temperature of $0$ °C, thermal voltage of type K wires at the cold junction temperature is subtracted from the signal to implement cold junction compensation.

The temperature difference is then calculated by a polynomial function with known Seebeck coefficients. The temperature of the cold junction is monitored by a resistance thermometer of type Pt-1000 from Heraeus, the terminal block is shielded by aluminium sheets and copper tape from temperature gradients. The re-

sistance is measured through a voltage drop difference in comparison to a known 1 k$\Omega$ type coal resistor. The coal resistor value is derived from a comparison to a precision resistive coil. The resistances at the reference temperature $R_0$, shown in table 3.1, are measured in an ice bath. For the resistive values polynomial temperature dependencies (DIN, 2009), are used to account for shifts between room temperature and reference temperature. . The estimated uncertainty in the temperature measurements is $\pm 0.5$ K. For convenience, the temperatures are presented in degrees Celsius and for calculations are expressed in Kelvin, with $0\ ^\circ\text{C} = 273.15$ K.

| Part | $R_0$ in $\Omega$ | Model | Remarks |
|---|---|---|---|
| Ref | $350 \pm 0.086$ | Burster 1142S | $\pm 0.02$ %, $<$ $\pm 2$ ppm/K, manufacturer calibrated at 23 °C |
| Pt 1 | $1000 \pm 2$ | Heraeus 32209220 | $\pm 0.12$ % class, monitoring cold junction |
| C | $978 \pm 2$ | Conrad 418706 | $\pm 5$ % class, reference in the experiment, has a negative linearity coefficient |
| Pt 4 | $1004 \pm 2$ | Heraeus M422 | was destroyed by a heater short circuit |
| Pt 15 | $1004 \pm 2$ | Heraeus M422 | monitoring chamber temperature |

**Table 3.1.:** Calibrated $R_0$ values for temperature calculations

## 3.5 Heated target design

The measurements are taken on a grid of different pressures and temperature values. With the pressures in the range of $0.1$ to $2.5$ MPa, temperature values under investigation are above the saturation temperature of evaporation of the fluid. According to reported values, the transition is expected to cover a region up to $300$ °C ($573$ K) at ambient pressure. With elevated pressure, the saturation temperature rises by $100$ K, so the maximum temperature of the experiment design is $400$ °C ($673$ K).

The heater is integrated into the optical system as an enabler for aligning the target plate to the projection axis and to the gravity vector, horizontally. Therefore, the aluminium base plate of $1$ inch cage cube from Thorlabs is drilled and threaded accordingly. The top of the cage cube is drilled to provide clear passage for the droplet generator and, in case of top view recordings, for the objective.

Upon the base plate, a stack of materials is placed as follows: PTFE insulation layer of $3$ mm as main insulation, a porous glass ceramic layer of 1 mm for thermal insulation above $533$ K ($260$ °C), the heater type Ultramic600 CER-1-01-00002 from Watlow consisting of sintered aluminium nitride, a layer of heat conductive material and a $3$ mm thick Al99.5-metal target plate.

The heater has an integrated type K thermocouple inside, which is used for heater control. The maximal sensor temperature offset due to the distance from the sensor to the surface is $1.2$ K according to equation (3.2) and is not considered in further calculations.

The top surface of the target is polished with corundum abrasive paper with grit sizes P100, P250, P360 and with corundum polishing paste from Nigrin to a mirror-like appearance (Buchmüller et al., 2012).

Below the base plate a cooling fan and a compact radiator are mounted, to avoid the optical structure from heating up in case of overheating of the heater. This fan also stirs the air and homogenizes the humidity and temperature of the air in the chamber. During specified operation no temperature difference between the base plate and the radiator was noticed, indicating low heat losses on the bottom side of the heater.

## 3.6 Heater control loop

The heater has a power rating of $967$ W with a $240$ V AC supply, corresponding to a potential heat flux of $1.5$ MW/m$^2$ on the aluminium surface. In the heating up of the experiment this allows the heater assembly to reach heating rates of $50$ K/s at full throttle.

This high power rating is convenient to achieve DNB in water at high temperatures and high pressures in spite of possible heat losses. On the other hand, this also means that an automatic closed loop control is needed to maintain the required temperature setting.

Considering the maximal heating rate above, if a temperature precision of $0.1$ K is aimed for, and the power of the heater can be controlled over $50$ steps, from zero to full throttle, the update time of the control loop needs to be roughly less than $T_s = 0.1$ s. This estimation is derived from the understanding that the smallest heating power or the smallest heating time increase leads to an increment of experimental temperature.

The heating power diffuses from the heater filaments to the wall surface. In this process a step-sized increment is reduced to the value of $1$ % of the initial value (Baehr & Stephan, 2006a) at the diffusion length $x_{100}$

$$x_{100} = 0.733\Lambda = 0.733 \times 2\sqrt{\pi\ \alpha\ t_0} \tag{3.3}$$

where $\Lambda$ is the thermal penetration depth, $\alpha$ is the thermal diffusivity, and $t_0$ is the length of the period.

In the current heater assembly, $x_{100}$ has a value of 4.4 mm. This implies, that fluctuations produced by the changes in the digital heater control steps are evened out by the heat diffusion and do not reach the upper heater surface. Thus, the temperature stability in the experiment is enhanced by the heat diffusion through the heating plate.

The modulation of the heater power is implemented as a fast on-off control using the pulse width modulation (PWM) technique. The PWM settings are chosen to the period of $100$ ms divided into $100$ steps, diluting the fluctuations of the modulation by thermal diffusion.

The controlled heater output ratio of full output $P_{PID}$ is calculated as a portion of full power, according to the difference of the target plate temperature to the requested set-point temperature $\Delta T_{PID}(t) = T_{set} - T_t(t)$

$$P_{PID}(t) = K_c \left[ \Delta T_{PID}(t) + \frac{1}{T_i} \int_0^t \Delta T_{PID}(\tau) d\tau + T_d \frac{d}{dt} \Delta T_{PID}(t) \right] \tag{3.4}$$

where $K_c$ is the controller gain, $T_i$ is integral time in minutes and $T_d$ is the derivative time in minutes (National Instruments, 2008, p. 2-1).

The values of $K_c$, $T_i$ and $T_d$ are the parameters of the PID controller. Their empirical setting is well known (Ziegler & Nichols, 1942, 1993). Nowadays, one of the most adaptable methods of the setting calculation is called the "reaction

curve" (Bennett et al., 2007) method: the control loop is opened, a step function is applied at the power input and the system reaction is recorded. Such an approach is very simple, but operation on the open loop is unsafe (Litz, 2013, chapter 2.6.4). Variations of this method are known to allow parameter identification in closed loops.

The PID values are calculated with the formula of *Chien, Hrones* and *Reswick* for optimized setpoint response without overshoot (Litz, 2013, p. 158). This formula show better robustness in comparison to the other established formula (Ho et al., 1995). The wide successful use of the formula in the industry comes from the relatively simple identification of the process model of a first-order system with time lag and the fact that many real world systems have one dominating responsive effect. In this particular setup, the tuned values of the PID parameters are:

$$K_c = 1.6 \text{ 1/K}, T_i = 8.2 \text{ s}, T_d = 1.5 \text{ s} \tag{3.5}$$

The response time constant is measured by the time to reach $63.2$ % of the final response value, accounting for an exponential saturation. The slope-of-the-tangent method is also a well-known method to measure the time constant, but it is not considered here due to its sensitivity to noise.

During the experiment, microscopically small electric discharges through the insulation occur, when water enters the pores of the ceramic. This does not cause damage, as the currents are small and the water dries up quickly, but during the discharges the voltage sensing of the thermocouple sensors is overdriven. These measurements are represented by the LabVIEW logic as "saturated value" and automatically discarded in the processing of mean values.

## 3.7 Optical setup

The measurement of the diameter and velocity of a fluid droplet in flight prior to the impact can be achieved only by non-invasive methods, in order to keep the shape of the droplet undisturbed. Electromagnetic waves are sufficiently fast and can be focused to allow observation of effects from outside of the pressure chamber through windows. This reduces the effort of the setup, as the most complex sensors, i.e. the high speed optics, are not installed inside the chamber. Using visible light promise the most adequate results in respect to the wavelength, because of the involved length scales. Infrared radiation and longer wavelengths provides too little spatial resolution for the optical setup to register secondary droplets and boiling bubbles. Ultraviolet illumination would ionize some of the fluid molecules and hence alternate the chemistry of the wetting process.

The interaction of light and matter is complex. Especially in the field of light scattered by small transparent particles, there is ongoing research on the various optical measurement methods, from shadowgraph to time-of-flight-methods (Tropea, 2011; Linne, 2013). Nevertheless, every optical solution involves compromises and limitations. Preliminary considerations and tests were performed to ensure a functional setup, including the tests of the components' performance.

The scattering of visible light by a droplet is a complex phenomenon in itself, and is approximated here by the wave nature of light according to the *Huygens-Fresnel* principle. Even with the illumination approximated a planar monochromatic coherent incident wave, the light scattered by a transparent water sphere of $100\ \mu$m diameter is divided into various parts, i.e. being absorbed, reflected, refracted or even guided along the droplet's surface, as shown in figure 3.3 (Laven, 2004).

Substantial knowledge on droplet interaction with light is available. An established solution for the so-called far-field light distribution in this case was first presented by *G. Mie* in a treatment of colloidal gold particles (Mie, 1908). Solutions on more general approximations are published, for example for cylindrical particles (Debye, 1908). The computations for the series of scattering coefficients were improved by rearranging the algorithm (Wiscombe, 1980). Complex particles were considered in calculations of the snow albedo in satellite imaging (Warren & Wiscombe, 1980). Scattering libraries use the implementation in the Fortran programming language (Bohren & Huffman, 1983), which serves as a common denominator in code comparisons. For application of laser illumination, Gaussian-shaped light sources are modelled (Lock, 1995). Interpretation of surface wave coefficients for spheres leads to a comprehensive theory of backscattered light in glories (Laven, 2005). Furthermore, approaches to model ellipsoids have emerged with specialised algorithms (Gouesbet & Gréhan, 2011) and models of light scat-

tering of multiple agglomerated spheres are shown (Mackowski & Mishchenko, 2011). For dense sprays, spatial modulated illumination is proposed to reduce multi-scattered light (Berrocal et al., 2009). Therefore, in many cases, a particular scene of objects can be simulated to predict light scattering based on the theory.

For the choice of the scattering angle and the light source in the present setup, the simulation of light scattering from a spherical water droplet in figure 3.3 is consulted. The angular plot shows the relative intensity of scattered light in dependence from the scattering angle for perpendicular and parallel polarization. This diagram is simulated by a tool from (Laven, 2003).

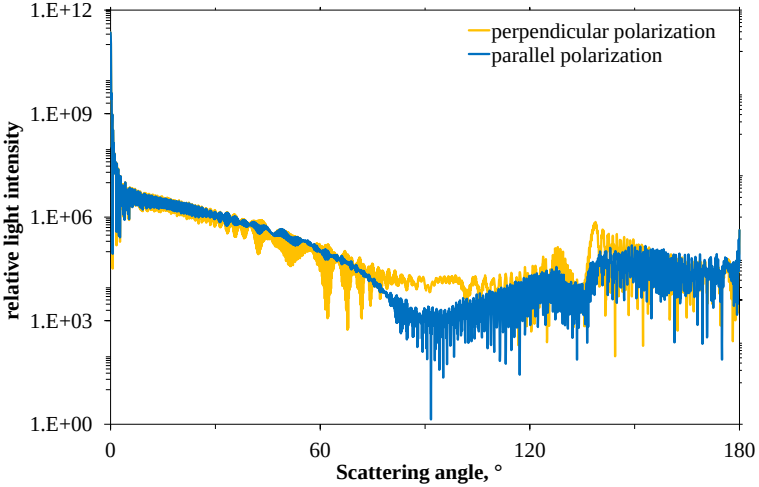


**Figure 3.3.:** Mie intensity calculation of 650 nm monochromatic light, scattered by a spherical $100\ \mu$m water droplet

The maximum scattered light intensity in figure 3.3 is located at a zero degree scattering angle, i.e. in forward-scattering. Here the intensity is several orders of magnitude higher, than with other arrangements. Therefore, this scattering angle is chosen for the present optical setup.

Other scattering angles are used by optical measurement techniques which provide information on droplet size distributions, like the phase Doppler technique, or analysis of cumulative fringe patterns from a laser beam. Although these

techniques provide high accuracy for measurement of particle sizes of secondary droplets, application to single droplet impact is not feasible. The phase doppler technique collects data from a single measurement volume, which has to be traversed through the field of view. During the scanning, the experimental parameters need to be held constant in a stationary spray process. As single droplet impact is instationary, the impact would have to be repeated for every measurement volume, while scanning the field of view.

For investigation of small droplets a high magnification is needed. On the other hand, the field of view should include the entire target area. In combination with the required object distance of $0.45$ m, a focal length of 100 mm is required for the lens. The value for the magnification is $0.29\times$. The aperture of the receiving optics is in the usual range, the focal ratio of the current setup is approximately $f/4$. As will be subsequently presented, the scene is illuminated by stratified light with low incident angle, illuminating only a part of the receiving aperture, increasing the f-number further.

The generated secondary particles are distributed around the impact axis. The measurement of the secondary droplets need either to estimate the out-of-focus particles of the three-dimensional pattern, or to use an increased depth of field by reducing the effective aperture. The latter approach is used in the present setup. With the receiver aperture as explained above and the diffuse light illumination, the depth of field is $1.9\ mm$. Details of the calculations are provided in the subsection below.

As the process of droplet impact is on a microsecond time scale, the available illumination intensity during exposure is an important issue. Although the light quantity is usually considered in the way "the more intensity the better", in the field of high-speed imaging the use of a continuous light source imposes other constraints. Continuous lighting imposes an additional heat load on both the investigated object and the optical system. The heat load is in the order of several hundred watts, even though, for the values of 1000 fps and $1\ \mu s$ exposure, the receiver shutter is open only $10^{-3}$ part of the time. In addition to energy inefficiency, such a heat load would affect temperature measurements by adding uncontrolled temperature gradients in the experiment, or even evaporate significant amounts of test fluid before droplet detachment.

Decreased aperture and bandwidth of the illumination influence the appearance of the edges of the droplet in the imaging, as individual diffraction patterns can be observed. Scattering of plane waves can be simulated (Laven, 2004), or inversely, droplet size can be deducted from scattering patterns (Graßmann & Peters, 2004). When droplets are approximated as round nontransparent disks, with diffraction calculation is simplified to the *Cornu*-spiral model, interference patterns can be evaluated without using holographic inversion. For droplets with diameter $> 10\ \lambda$,

the wavelength of the light source, the edges of the droplets produce independent fringes. So for droplets with size above $10\ \mu$m the fringes can be modelled by light interference on the edge of a semi-infinite screen (Hecht, 2002), as shown on figure 3.4. The edge position can be evaluated from both sides of the droplet in order to calculate the diameter or form parameters, like sphericity.

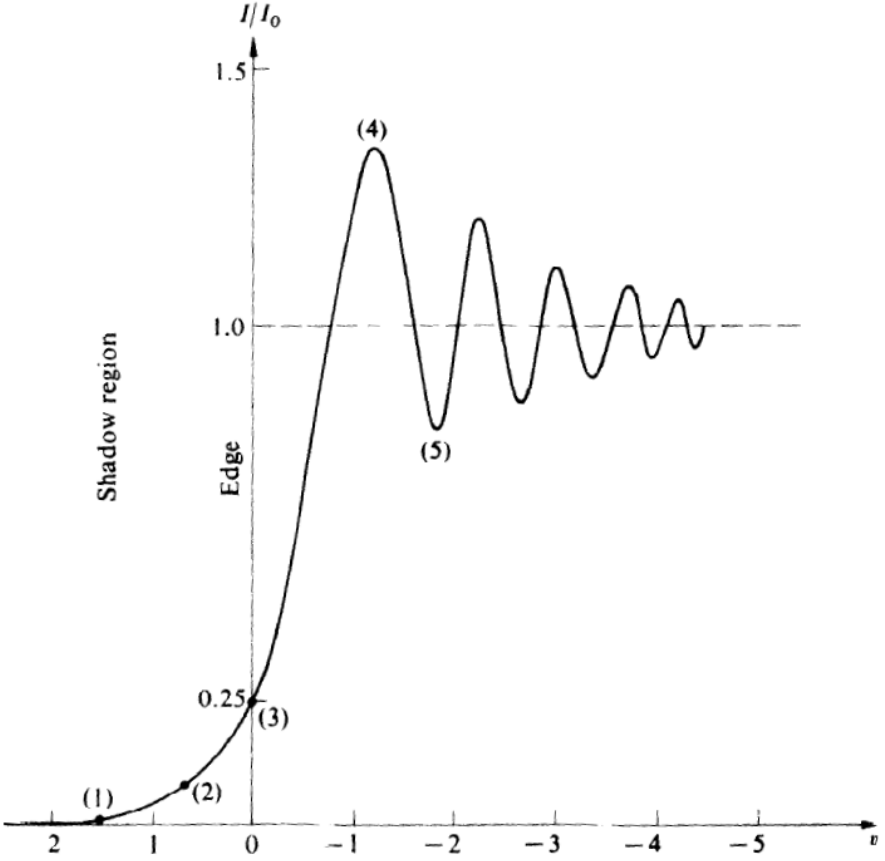


**Figure 3.4.:** Light intensity on the semi-infinite screen (Hecht, 2002)

By using a $445$ nm laser diode stroboscope with an expanded laser beam as illumination, it is possible to reduce the aperture of the illumination and obtain the coherence length at a typical value of $1$ mm, so that such interference fringes oc-

cur and are directly observable, figure 3.5(b). In the figure, a droplet impact with secondary droplet generation at $p = 0.1$ MPa and $T_t = 423$ K $= 150$ °C can be observed.

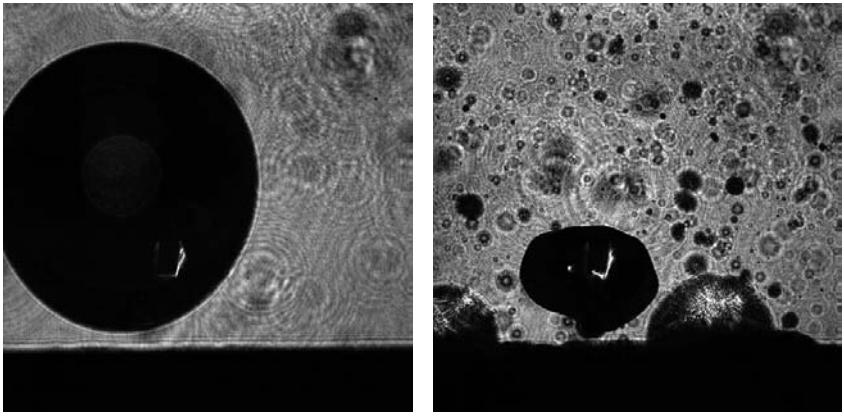

(a) Incoming droplet (b) Secondary droplets

**Figure 3.5.:** Visualization of droplet impact with laser illumination

Multiple fringe patterns, corresponding to both the primary and the secondary droplets, overlap in the field of view. Overlapping images impose a limit to the particle density for the fringe imaging technique, such limitations are discussed in a recent review (Linne, 2013, fig. 41). The interference patterns contain information about the size, shape, position and the refractive index of the particles, albeit machine-based extraction of fringes and size recognition needs to inverse the scattering calculations, which is a rather complicated task.

However, one can exploit the model for the semi-infinite screen for a simplified imaging setting. The interference pattern in figure 3.4 scales with the wavelength of the source. If one would use a light source with two or more emission lines, the oscillating interference pattern, marked by (4) and (5) on the right side of the plot, for the added wavelength would successively alleviate the peaks and throughs for the prior ones. Notably, the relative intensity value of $0.25$, corresponding to an amplitude attenuation of $0.5$, is located at the edge position even in the multi-wave case, as marked by (3) in figure 3.4. Thus, edge detection can be done by an intensity threshold function. A local threshold function (Schindelin et al., 2012), set at the graylevel of $25\%$ is used in the present setup for edge detection. This

approach has physical reasoning in the droplet imaging context, in comparison to various existing algorithms (Sezgin & Sankur, 2004), or the approach of the steepest gradient (Castanet et al., 2013).

The illumination with an LED used in the experiment has a coherence length of $4.6\ \mu$m. This value is derived from the measured spectral bandwidth of the LED of approximately $20$ nm. Thus, no interference patterns are observed in the images. The blue light ($\lambda = 460 \pm 20$ nm) also induces low chromatic abberation, even if uncorrected aspheric singlets are used.

The stroboscope circuit is synchronized with the camera at a frame rate of $4000$ 1/s. The pulse length of $300$ ns is used to ensure sufficient light on the detector. The pulse voltage on the LED is nominally higher, by a factor of $\approx 10$, than the typical maximal voltage for CW-operation permitted by the manufacturer, but it is accepted by the LED due to the low duty cycle of approximately $1/830$ and the parasitic capacitance and inductance of the LED. The voltage of the pulse driver is set to the beginning of saturation of the light intensity. The intensity is observed in the histogram of grey values, as received by the high-speed camera.

The focal length of the camera lens, see figure 3.6, is $300$ mm, realized by two planar-convex lenses with an interim focus. The realized aperture is lower and the depth of field is higher, than set by the lens aperture, as the illumination is done via stratified light: the angle of divergence is $\approx 3.4°$, the square emitting area of the LED with the side length of $1.5$ mm is projected by a f=25.4 mm lens. The illuminated lens diameter at the receiving side is $14.7$ mm at the working distance of $250$ mm, thus the focal ratio is reduced to approximately $f/7$. Depth of field at this f-number is $2.6$ mm, equation (3.6). The pixel center distance on the sensor is $10 \pm 0.01\ \mu m$, and at the object plane $43.4 \pm 0.2\ \mu m$ according to calibration pictures. Details on the image scaling and calibration are provided in the section 3.7.2.

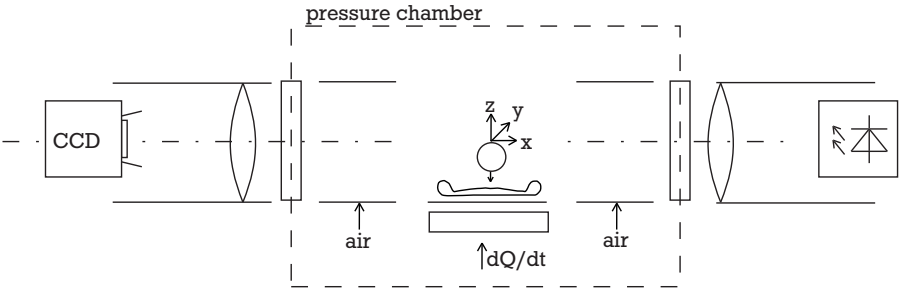


**Figure 3.6.:** Sketch of the optical setup.

The secondary droplets and condensate wet the optical windows of the pressure chamber. Air curtains, installed on the inner side of the windows, prevent this. The air curtains are tubes in the optic path, which have an air connector added radially. The dry air from the supply escapes from the open ends of the tubes. The air provides a counterflow for the secondary droplets, which are coming from inside, effectively disabling them from reaching the windows. On the outer side of the tubes, the air current provides ventilation of the optical surfaces keeping them clear from eventual condensation.

### 3.7.1 Depth of field

Depth of field in the setup is determined by the focal depth of the imaging $\delta z$ (Adrian, 1991) and (Tropea et al., 2007, eq. (5.244))

$$\delta z = 4(1 + 1/M_{opt})^2 \; f\#^2 \; \lambda \tag{3.6}$$

where $M_{opt} = 0.23$ is the magnification according to pixel calibration and $f\# = 7$ the focal ratio. For the presented setup the depth of field is $2.6$ mm. The value of the depth of field is chosen ten times higher than in the examples from (Adrian, 1991) to be able to detect particles outside of the focal plane.

For convenience, a calculation tool (Xcitex, 2001) was used to determine the depth of field, the motion blur and lens parameters in the experiment preparation The exposure time is set by the illumination, the motion blur is 0.01 pixels and is neglected.

### 3.7.2 Spatial calibration

For scaling of the images, a test target is recorded at the beginning of the measurement run. This is done with the fully adjusted settings of focus, aperture and positions of all optical components. In this setup a new M6 threaded rod is used as a calibration target, as the standard pitch of the M6 thread is $1$ mm. Since the rod is in mass production in a continuous process, the geometry of the thread is considered invariant. The screw pitch is validated with a caliper measurement. Along a distance of $50$ mm no deviation is measurable with the accuracy of $0.1$ mm, this corresponds to a thread pitch value of $1 \pm 0.002$ mm. The image of the rod is shown in figure 3.7(a), the red line marks the path, along which the profile measurement is taken. Figure 3.7(b) shows the line profile of the corresponding grey values. The distance between the crossings of the gray value $100$ line is $138$ pixel, or $138.3$ pixel using linear sub-pixel interpolation, for a real-world distance of $6$ mm. Thus, the real-world pixel size at the object plane is $43.4 \pm 0.2$ $\mu$m.

For calibration of the scale, the diameter of the rod is used. The base value of the diameter is measured with a caliper, the nominal size of $6$ mm is confirmed to be $5.98 \pm 0.02$ mm. For the optical measurement, the image is prepared to facilitate the postprocessing. The rod image is rotated, with bilinear approximation, such that the diameter direction coincides with the horizontal axis. Scaling is preserved during the rotation. The image is cropped to the middle section of the rod and processed as described in section 6.1 with the same settings, like the droplets.

The horizontal size of the recognized boundary is taken as the optically measured diameter of the thread. The size of $5.96$ mm is $0.7\%$ lower than the nominal value. Therefore, the spatial accuracy of the optical measurements is estimated to $\pm 40 \mu$m.

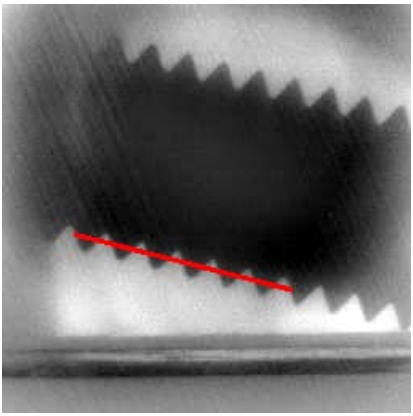

(a) Pitch measurement

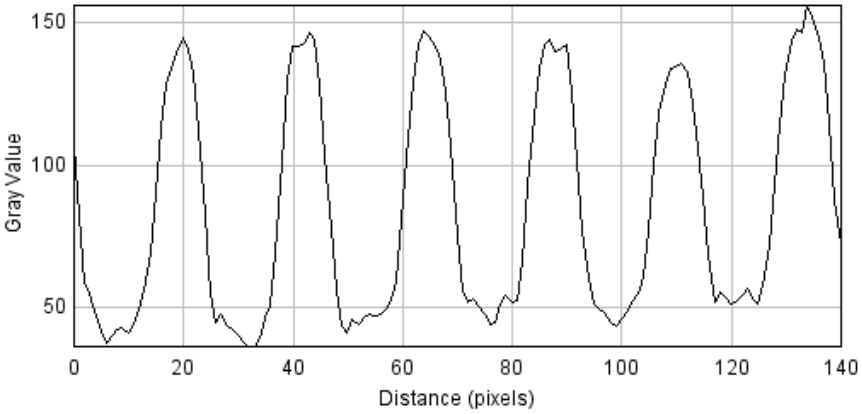


(b) Line profile

**Figure 3.7.:** Pixel size measurement

# 4 Boiling states

In this chapter the results of the boiling experiments are presented. First, the phenomena are observed qualitatively. Typical pressure and temperature points are chosen from the high-speed recording. Key images illustrate the particular behavior, frames in-between the shown images are omitted due to space constraints.

The map of the conducted measurements shows an overview of the data points and the corresponding outcomes, along with first theoretical findings on ONB and nucleation. The observed boiling states are classified phenomenologically. The map of measurements is shown also with reduced parameters, providing new insight into the structure of DNB and the Leidenfrost effect.

## 4.1 Classification of boiling states

The measurement points of this investigation are categorized phenomenologically into different outcome scenarios, as illustrated in the following figures. The scenarios differentiated are wetting $sA$, wetted boiling $sB$, transition boiling $sC$ and rebound $sD$.

The wetting state, shown in figure 4.1, is encountered at low temperature settings, starting with ambient temperature. The droplet touches and wets the surface. There is no nucleate boiling in the droplet observed and the evaporation time is longer, than the maximum recording time.

The wetted boiling state, shown in figure 4.2, is a state where nucleate boiling is seen with bubble development. Here the droplet acts as a small and shallow boiling pool. Boiling is clearly observed with vapor bubbles penetrating through the droplet. When the bubbles collapse, secondary droplets are formed.

In the transition boiling state, shown in figure 4.3, the droplet wets the surface at impact, including the inertial droplet spread phase and the first contraction phase of the impact. At least one detachment of the fluid from the target plate is detected during the recording time. With increased temperatures, the droplet is levitated over the surface, but touches the target surface at some moments with liquid parts. Therefore, only a part of the surface is dried out.

In the rebound state, shown in figure 4.4, droplets detach from the surface in the contraction phase of the impact. The droplets rebound without apparent sticking to the target surface, there is no prolonged contact between liquid and solid. The

rebound is an indicator of completed transition to the Leidenfrost state, a further increase of temperature up to $1400$ K does not change the outcome of the impact.

The pixel size in figures 4.1, 4.3 and 4.4 is $34.7 \pm 0.2$ $\mu$m because of increased magnification of the optics.

The lifetime of a droplet is an indirect indicator of the evaporation rate. At temperatures below the vapor saturation temperature the droplet evaporates progressively faster with rising temperature, the droplet lifetime falls from hours into the range of 10 s in wetting state $sA$. The evaporation can be detected by the fumes of recondensed vapor around the droplet and by the change of refractive index of air around the droplet, which produces Schlieren around the droplet in the figures. Evaporation starts with a short delay, due to the contact temperature effect.

When the temperature rises above nucleation superheat, bubbles appear and the lifetime is as short as $1$ $s$. A minimum lifetime is expected in the nucleate boiling state, this is also because satellite droplets break apart and reduce the mass of the droplet, as shown in figures 4.11, 3.5(b), 6.2(c) and 4.2(d). At the upper end of the boiling state the lifetime rises again, despite the rising temperature, because the bubbles merge together and produce the insulating cushion. The droplet is partially suspended by the vapor bubbles, as shown in figure 4.2(d) and figure 4.2(e).

There is a gradual change to the transition state, as the droplet is suspended more rapidly by the higher amount of vapor, and levitates for longer time fractions, before returning to the target by gravity for the second time. The transition state is distinguished from the previous state by the detection of full detachment of the droplet during the recording time. This "dancing" of the droplet is seen in figures 4.3(e) and 4.3(f), for example. Generated vapor flows to the sides of the droplet, as it is directed by the flow in the droplet-wall gap.

The change to a smooth non-wetting rebound takes place at the border between $sC$ and $sD$. The generation of vapor at the lower part of the droplet changes the mode to a much faster cut-off of the droplet and the target, there are no bubbles or ligaments of the droplet touching the target surface seen in the recordings above $\approx$ $470$ K at ambient pressure. The explosive character of the vapor generation introduces horizontal oscillations in the droplet, which sometimes suffice to break off satellite droplets larger than $10\%$ of the primary droplet. Multiple secondary droplets, with size of the order of magnitude of the smallest detectable size, are generated. The secondary droplets escape with velocities of the order of magnitude of $10$ m/s in the direction ranging from horizontal to less than $30^\circ$ inclination. This velocity is more than one order of magnitude faster than for satellite droplets generated by collapsing lamellas. With rising temperature, the amplitude of the vibration of the primary droplet and the amount of detected secondary droplets is decreased. Then, a rebound of the droplet from the surface without apparent wetting is observed.

In the boiling state $sD$, a maximum droplet lifetime is observed typically (Baumeister & Simon, 1973; Biance et al., 2003). With the vapor layer stabilized, heat conduction through the contact areas is quite low, the lifetime can be as high as 120 s. As radiative and convective heat transport increase with temperature, there is a continuous fall of droplet lifetime with rising temperature. For the residence time, an asymptotic value for the non-wetting rebound is expected.

### 4.1.1 $sA$: wetting state

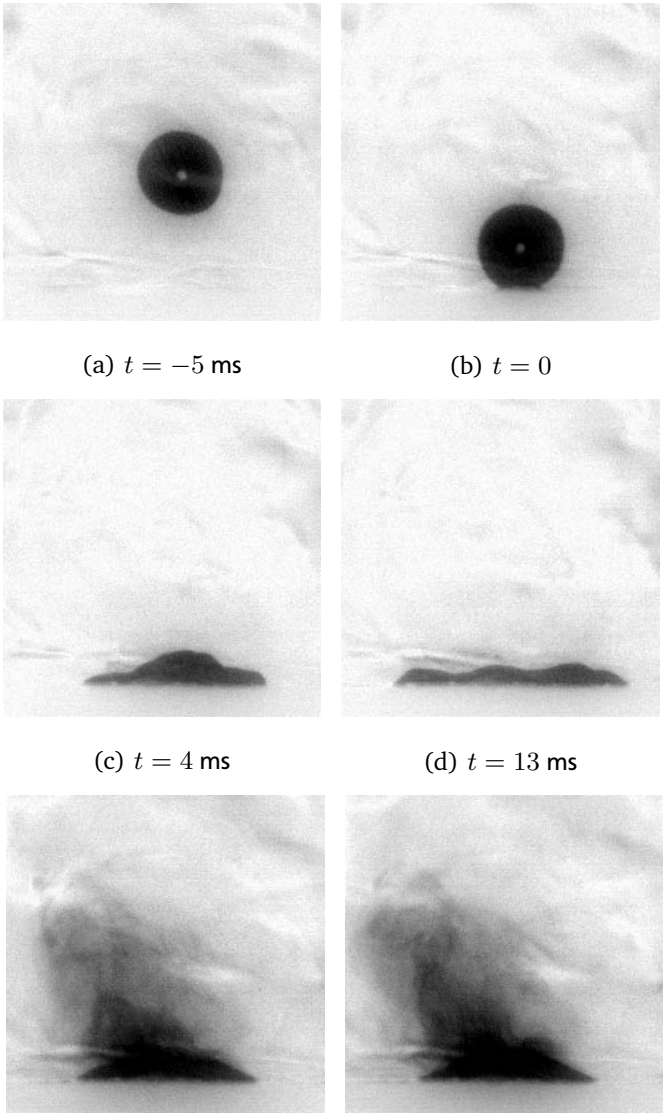

(a) $t = -5$ ms (b) $t = 0$

(c) $t = 4$ ms (d) $t = 13$ ms

(e) $t = 86.5$ ms (f) $t = 98$ ms

**Figure 4.1.:** Wetting state $sA$ at $T_t = 473$ K and $p = 1.7$ MPa

### 4.1.2 $sB$: wetted boiling state

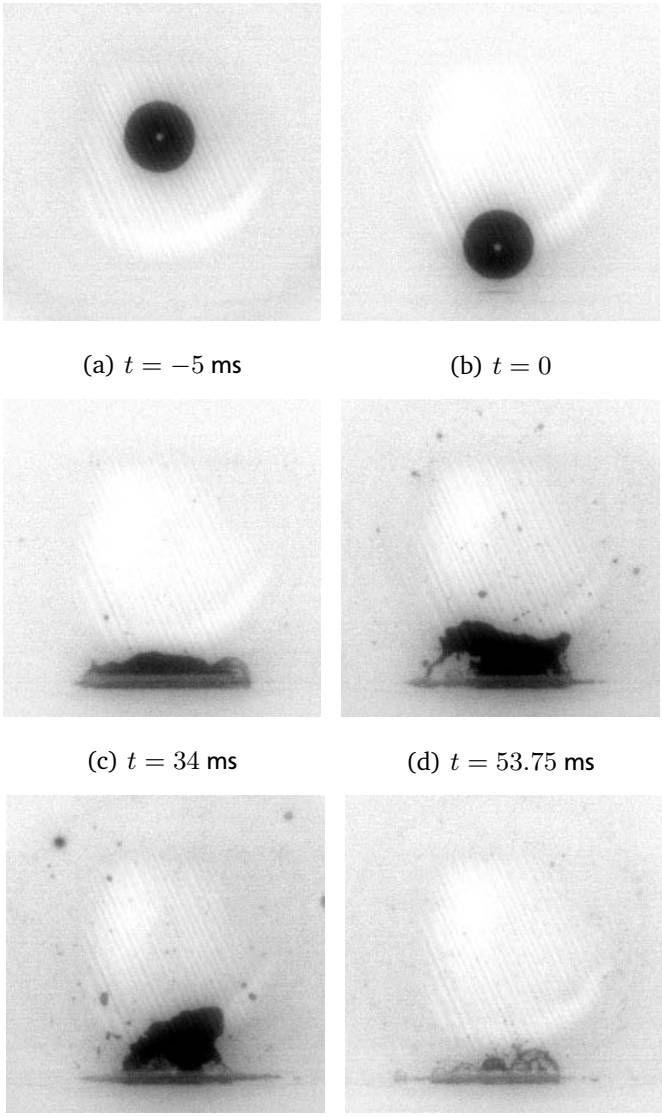

(a) $t = -5$ ms (b) $t = 0$

(c) $t = 34$ ms (d) $t = 53.75$ ms

(e) $t = 96$ ms (f) $t = 214$ ms

**Figure 4.2.:** Wetted boiling state $sB$ at $T_t = 413$ K and $p = 0.1$ MPa

### 4.1.3 $sC$: transition boiling state

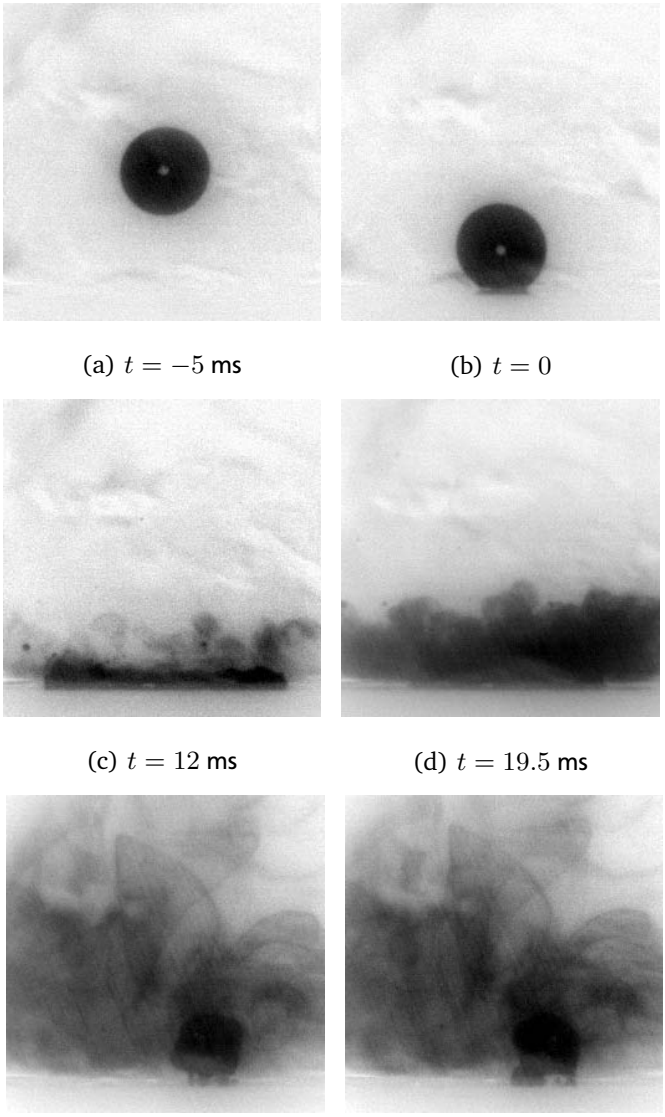

(a) $t = -5$ ms (b) $t = 0$

(c) $t = 12$ ms (d) $t = 19.5$ ms

(e) $t = 59.5$ ms (f) $t = 62.5$ ms

**Figure 4.3.:** Transition boiling state $sC$ at $T_t = 543$ K and $p = 0.9$ MPa

### 4.1.4 $sD$: rebound state

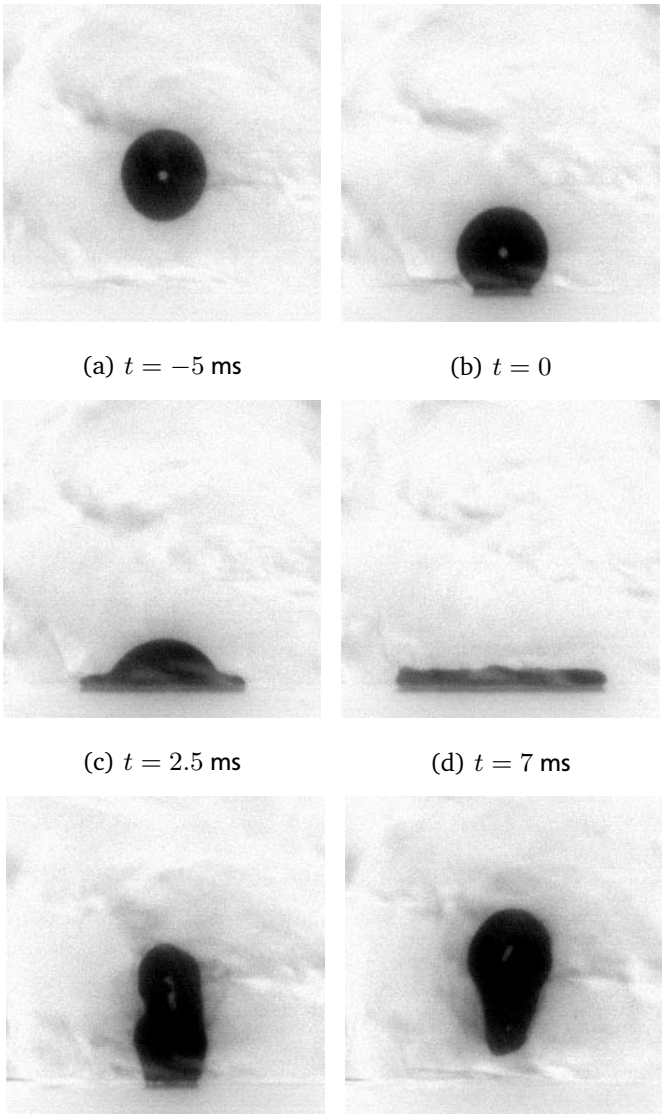

(a) $t = -5$ ms (b) $t = 0$

(c) $t = 2.5$ ms (d) $t = 7$ ms

(e) $t = 26$ ms (f) $t = 37.5$ ms

**Figure 4.4.:** Rebound state $sD$ at $T_t = 623$ K and $p = 0.9$ MPa

### 4.1.5 Map of the boiling states

A pressure-temperature map of the boiling phenomena is shown in figure 4.5. The measurements are taken on a fixed grid of different pressures and temperatures. The temperature settings of the grid are refined near the borders of the boiling regimes to improve the accuracy of the transition detection. Temperature values of interest are above the saturation temperature of evaporation of the fluid, which is marked by $T_{sat}$ in figure 4.5. The four boiling states are depicted in figures 4.5, 4.7 and 4.13 with corresponding symbols.

The phenomenological change from nucleate boiling state $sB$ to transition boiling state $sC$ at ambient pressure and wall temperature of $427 \pm 1.5$ K corresponds with the reported experimental value of $426$ K for an aluminium target in (Baumeister & Simon, 1973). The lines in figure 4.5 show the saturated vapor temperature

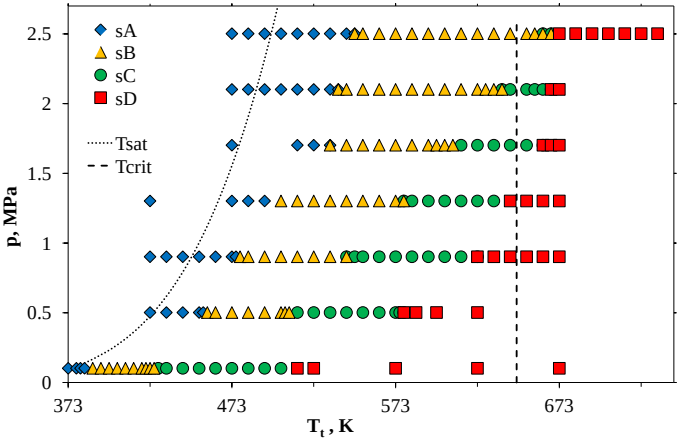


**Figure 4.5.:** Map of boiling states. Saturation line $T_{sat}$ and critical temperature of the fluid $T_{crit}$ are shown for orientation, without equation (2.1). Boiling states: wetting - $sA$, wetted boiling - $sB$ transition boiling - $sC$, rebound - $sD$.

$T_{sat}$ from the tabulated values in (Baehr & Kabelac, 2005) and the critical temperature of water $T_{crit}$ for orientation.

Increasing droplet impingement velocity and increasing droplet size generally increase the characteristic boiling temperature, as known from (Bernardin et al., 1997), therefore this study concentrates on the effects of increasing chamber pressure.

### 4.1.6 Single parameter influence of pressure

According to the saturation line, an increase in temperature is generally expected for all state borders with increasing chamber pressure. This shift is observed for temperatures of the onset of nucleate boiling, the departure from nucleate boiling and the onset of the rebound regime, respectively.

Gas density is nearly proportional to chamber pressure. Gas density is also dependent on the local temperature. Temperature fluctuations are not visible at ambient pressure, but increasing *Schlieren* distortions of the background illumination are seen with increasing pressure. The visibility of temperature fluctuations is increased with increasing pressure, as expected.

Pressure dependence of liquid viscosity and liquid surface tension is negligible (Bett & Capi, 1965; Horne & Johnson, 1966), this is observed qualitatively by the apparently constant frequency of vibrations of the primary droplet after impact.

The following results consider the dependence of the phenomena on both the pressure and the temperature, dividing the experimental field in four boiling states.

## 4.2 Transitions between boiling states

The phenomenological changes in boiling states implicate validity borders for models and engineering correlations. As in the example of the heat transfer rate in the boiling curve, and lifetime of the droplet, the phenomenological borders also correlate with characteristic points. Thus, the borderlines between the boiling states are of particular interest for application purposes.

Three borders for transitions between the boiling states are discussed further, as shown in figure 4.6. The borders correspond to the onset of boiling in the droplet, $sA \vee sB$, the onset of partial droplet levitation, $sB \vee sC$, and the droplet rebound, $sC \vee sD$, respectively.

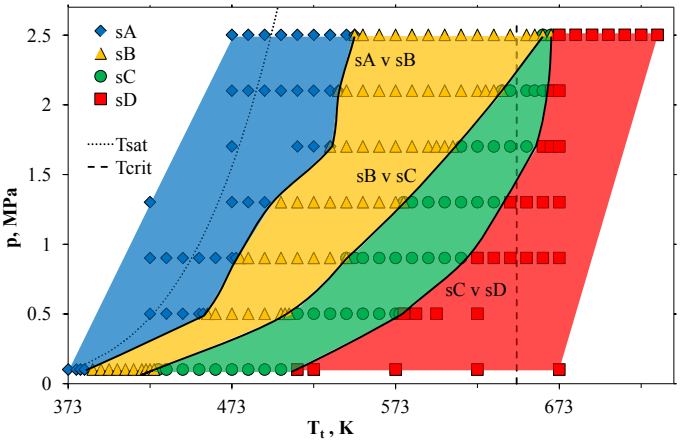


**Figure 4.6.:** Transitions between boiling states. Saturation line $T_{sat}$ and critical temperature of the fluid $T_{crit}$ are shown for orientation, without equation (2.1). Boiling states: wetting - $sA$, wetted boiling - $sB$ transition boiling - $sC$, rebound - $sD$. Transitions: onset of boiling in the droplet - $sA \vee sB$, onset of partial droplet levitation - $sB \vee sC$, onset of droplet rebound - $sC \vee sD$

The saturation line for bulk liquid, $T_{sat}$, predicts smaller temperatures for the border of the wetting state $sA$ and wetted boiling state $sB$ than observed in the experiment. Thus, models introducing boiling with nucleation are introduced further and shown in figure 4.7. These models incorporate also the contact temperature equation (2.1).

### 4.2.1 Border of the wetting state $sA$ and wetted boiling state $sB$

The saturation line for bulk liquid, $T_{sat}$, deviates from the observed shifts in temperature with increasing pressure of the $sA$ and $sB$ state border. Phenomenologically, state $sB$ is nucleate boiling. Therefore, $hS$, the saturation hypothesis with transient heat conduction from equation (2.1), and $hN$, the boiling model with heterogeneous nucleation from chapter 2.2.1 and transient heat conduction from equation (2.1), are considered further. The approach is to find the factor which changes with pressure, which is yet to account for an extension of theory.

#### 4.2.1.1 Heterogeneous nucleation for contact area

Hsu's criterion underestimates the overheat temperature. Hence, an extension to account for the limited contact area of the droplet is proposed below. A single droplet in wetting state is in contact with the wall only at some area $A_{drop}$, depending on the droplet spread diameter $D_{max}$

$$A_{drop} = \frac{\pi D_{max}^2}{4} \tag{4.1}$$

It is assumed that one active nucleate site per droplet contact area is sufficient to initiate the process of nucleate boiling, leading to a required number of active nucleation sites:

$$N_s = 1/A_{drop} = \frac{4}{\pi D_{max}^2} \tag{4.2}$$

This criterion is a low boundary for onset of nucleate boiling, inside the nucleate boiling state $sB$ multiple nucleation sites be active and the nucleation sites are distributed stochastically on the surface.

For the number of active nucleation sites $N_s$ per square meter in bulk water upon a polished aluminium plate (contact angle $\theta_e = 30°$) exist empirical correlations in (Basu et al., 2002), in SI units:

$$N_s = 3400[1 - cos(\theta_e)]\Delta T_B^{2.0} \quad \Delta T_B < 15 \text{ K} \tag{4.3}$$

$$N_s = 0.34[1 - cos(\theta_e)]\Delta T_B^{5.3} \quad \Delta T_B \geq 15 \text{ K} \tag{4.4}$$

The nucleation overheat temperature $\Delta T_B$ can be calculated from the number of active nucleation sites and the target temperature $T_t^\star$ for ONB in the droplet can be expressed with equations (2.1) and (4.3) as

$$hN \Rightarrow T_t^\star = (T_{sat} + \Delta T_B)(1 + \frac{e_l}{e_t}) - T_l \frac{e_l}{e_t} \tag{4.5}$$

For water at $p = 1.7$ MPa, $T_{sat} = 477.47$ K $= 204.32$ °C, for a droplet with the observed $D_{max}$ of 6.9 mm, $A_{drop} = 3.7 \times 10^{-5}$ m$^2$, $N_s = 2.6 \times 10^4$ 1/m$^2$ and the nucleation overheat temperature $\Delta T_B = 7.66$ K. With the initial droplet temperature $T_l$ of 293 K and the known material properties $T_t^\star$ is calculated to $500$ K $= 226.85$ °C. This temperature should mark the lower limit for the state of nucleate boiling while the droplet wets the surface. Plot of $T_t^\star$ in the $p, T$ regime map shows the predictions of this heterogeneous nucleation hypothesis, $hN$, and allows for comparison with the observed ONB in discussion of the results.

#### 4.2.1.2 Heterogeneous nucleation with fluid motion

During droplet impact, fluid motion inside the droplet enhances the heat transfer by adding convection. Equation (2.9) from (Roisman, 2010a) accounts for this increase by a correction based on a dimensionless fluid flow solution.

With increasing pressure, the temperature region of boiling is increased first due to the increasing saturation temperature of the fluid. As the fluid stays liquid in these conditions, the viscosity decreases, allowing increased flow velocities, by $40\%$ increased heat transfer and, as a result, decreased liquid-metal contact temperature according to equation (2.9).

Thus, with consideration of fluid flow, temperature of metal target for onset of boiling is increasing progressively with increasing pressure, and marked as flow hypothesis $hF$

$$hF \Rightarrow T_t^\star = (T_{sat} + \Delta T_B)(1 + \frac{e_l}{\mathfrak{F}(Pr, 0, \infty)\, e_t}) - T_l \frac{e_l}{\mathfrak{F}(Pr, 0, \infty)\, e_t} \tag{4.6}$$

with the Prandtl number $Pr$ decreasing from $1.6$ to $0.8$ at increasing pressures of the experiment.

The decrease of the Prandtl number at saturation temperature with increasing pressure is caused by the reduction of liquid viscosity with increasing temperature. Elevated pressure allows the fluid to stay in the liquid phase at higher temperatures, as compared to ambient pressure conditions.

For the calculation of contact temperature using equation (2.9), the thermal conductive properties are considered. Thermal resistance of the surface of aluminium specimens is dependent on the surface finish and the thickness of the oxide layer (Peterson & Fletcher, 1990). Thermal conductance of metal surfaces is also dependent on the materials in contact and the type of contact (Wolff & Schneider, 1998). In the present case, the preparation of the metal plate includes polishing with corundum paper and corundum paste. After the polishing the surface is exposed to air. Both processes induce an aluminium oxide passive coating of the metal and aluminium oxide inclusions on the surface. The composition of the solid layer adjacent to the surface of the target plate is a mixture between the aluminium and aluminium oxide parts. The detailed composition on the molecular scale could not be determined. Therefore, the thermal effusivity of the metal surface is assumed to be the mean effusivity of bulk aluminium metal $e = 25$ kW s$^{0.5}$/(K m$^2$) and crystalline aluminium oxide $e = 3.8$ kW s$^{0.5}$/(K m$^2$) with a value of $e_t = 14.4$ kW s$^{0.5}$/(K m$^2$).

The contact between the water and the metal plate is assumed as full wetted contact on the droplet area, with the occupied area of entrapped air and vapor in the nucleation sites being negligibly small.

The effect of the consideration of fluid motion and the conductive properties on the predicted target temperature for initiation of boiling in the droplet varies with the chamber pressure due to the change in liquid material properties. The temperature difference to the nucleation theory of bulk liquid, $hN$, predicted by fluid flow consideration alone and by the combination of fluid flow with the conductive properties at pressure $p = 0.1$ MPa is 3 K and $9.5$ K, respectively. At $p = 2.5$ MPa these effects contribute $8.3$ K and $24.3$ K, respectively. The effects interact and amplify the shift in the target temperature prediction. If surface conductivity effect would be applied to the $hN$ model alone, the temperature shifts at the pressures above would be lower, $4.3$ K and $9.9$ K, respectively.

The predictions of the models are shown in the next chapter for a comparison with experimental results on the first state transition.

#### 4.2.1.3 Comparison with experimental results

The saturation temperature at the liquid-solid contact area, the nucleation boiling line for the droplet spread diameter of $6.9$ mm and the nucleation boiling line considering fluid flow inside droplet are shown in figure 4.7 for evaluation. The values for saturation temperature are obtained from the tabulated values (Baehr & Kabelac, 2005), using the contact temperature equation (2.1). The nucleation line

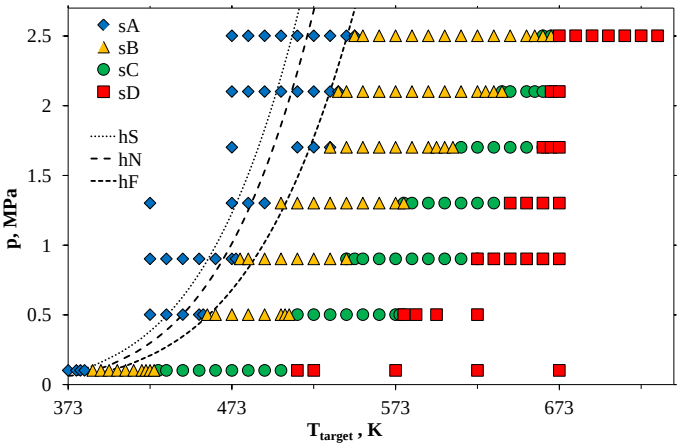


**Figure 4.7.:** Evaluation of various models on initiation of nucleate boiling: $hS$ - saturation temperature of water at the liquid-solid contact from equation (2.1), $hN$ - heterogeneous nucleation at contact area from equation (4.5), $hF$ - heterogeneous nucleation at contact area with convection inside the droplet from equation (4.6). Boiling states: wetting - $sA$, wetted boiling - $sB$ transition boiling - $sC$, rebound - $sD$

with superheat for onset of nucleate boiling at the droplet spread area, $hN$, is near the border of the wetting state $sA$ and wetted boiling state $sB$ at ambient pressure. However, this theory shows increasing differences at elevated pressure.

Taking into account the fluid flow inside the droplet and the thermal conductivity of the surface, $hF$ makes a difference in $T_t$ of $9.5$ K at ambient pressure, and $24.3$ K

at $p = 2.5$ MPa. The agreement between the prediction and the experiment is rather good.

Therefore the conclusion is, that boiling theory with nucleation sites for bulk liquids, projected to droplet areas, with consideration of fluid flow, describes the border of the nucleate boiling state at elevated pressure in the experiment.

### 4.2.2 Border of the wetted boiling state $sB$ and transition boiling state $sC$

#### 4.2.2.1 Previous models

Previous studies considering the possible factors for the transition from wetted boiling to levitated droplets are reviewed in (Bernardin & Mudawar, 1999). A cavity activation and bubble growth model of the Leidenfrost point and the Leidenfrost point model for impinging droplets and sprays from (Bernardin & Mudawar, 2002, 2004) were developed upon the analysis of experiments and lead to the predicted Leidenfrost temperature in K, depending on the droplet impact velocity $U_0$

$$hB \Rightarrow T_c = 273.15 + 162.0 + 24.3\, U_0^{0.64} \tag{4.7}$$

For the present experiment, equation (4.7) predicts $T_c = 448$ K. The prediction is invariant to pressure, thus the temperature for the $sB \vee sC$ transition would remain unchanged with elevated pressure.

As the temperature for the $sB \vee sC$ transition at ambient pressure corresponds to the reported experiment in (Baumeister & Simon, 1973), there is a question how this theory performs at elevated pressure. The correlation

$$hM \Rightarrow T_c = \frac{27}{32}\, T_{crit}\, [1 - exp(-0.52 \frac{(\rho_s/A)^{4/9}}{\sigma^{1/3}})] \tag{4.8}$$

where $A = 13$ is the atomic number of heater metal (Baumeister & Simon, 1973, eq. (34)), has pressure and temperature dependency in the surface tension term. This correlation for the Leidenfrost temperature is defined at standard pressure. For the scope of this study, the presence of pressure dependent parameters allows an extrapolated pressure-dependent prediction, which is called here the Baumeister hypothesis $hM$.

Fundamental physical properties of the fluid are captured by the saturation line model $hS$, the homogeneous nucleation model, i.e. the spinodal line $hH$ and the critical temperature of the fluid $hC$. For these models the contact temperature equation (2.1) is applied to recalculate for the initial target wall temperature.

The previous models predict temperatures for the departure from nucleate boiling state $sB$ to transition boiling state $sC$ that deviate from the experimental results with increasing pressure. This is not a surprise for the correlation $hB$, as it has no pressure dependency. Also the predictions $hM$, $hS$, $hH$ and $hC$ are obviously not following the trend of the experimental boundary. This calls for extended models and alternative approaches, such as the pressure dependent bubble coagulation model and the evaporative interface model.

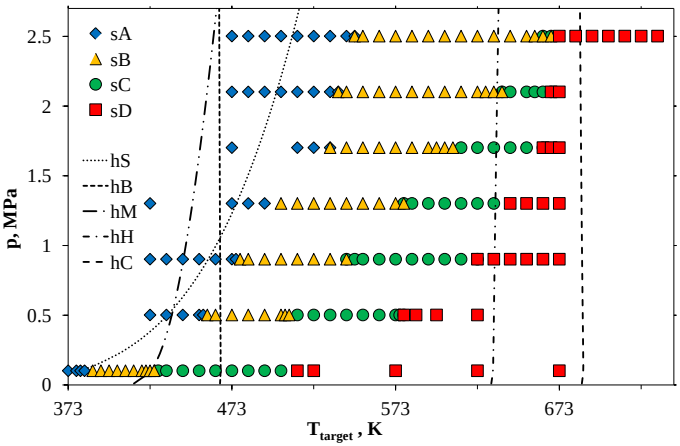


**Figure 4.8.:** Evaluation of existing models on the onset of droplet levitation: $hS$ - saturation temperature at the liquid-solid contact from equation (2.1), $hB$ - Leidenfrost point model for impinging droplets and sprays (Bernardin & Mudawar, 2004), $hM$ - Leidenfrost temperature correlation (Baumeister & Simon, 1973) extrapolated using pressure dependent parameters, $hH$ - spinodal line for homogeneous nucleation (Lienhard & Karimi, 1981) with equation (2.1), $hC$ - critical temperature of the fluid with equation (2.1). Boiling states: wetting - $sA$, wetted boiling - $sB$ transition boiling - $sC$, rebound - $sD$

#### 4.2.2.2 Heterogeneous nucleation for spots

In the transition state, droplets partially floating on the vapor layer and periodically touching the surface by oscillating parts of the droplet are observed. Here the modeling attempt by reducing the contact area is discussed briefly, as this shows the general need to introduce fluid flow phenomena in the theory.

The model $hN$ includes the consideration of limited contact area of the droplet and the corresponding effect on nucleation site density. This model is extended as a hypothesis for the transition boiling state and the phenomenon of temporally

levitated droplets which touch the metal surface periodically with protrusions being in contact only on the area of small spots.

In the case of droplet protrusions touching the heater, the area of contact is a dynamic value and can be quite small. Based on observations we assume a contact spot with an area of $A = 100\ \mu\text{m} \times 100\ \mu\text{m} = 0.01\ \text{mm}^2$. The corresponding density of the active sites would be $N_s = 10^8\ \text{sites/m}^2$ according to equation (4.1). Such a high site density is expected at high wall superheats. However only few experiments with site density over $2.3 \times 10^6\ \text{sites/m}^2$ and superheat greater than 26 K for nucleate boiling of water are found in the literature (Basu et al., 2002). Using equation (4.4) a superheat of 40.89 K is estimated for $N_s = 10^8\ \text{sites/m}^2$ at the border between the nucleate boiling state $sB$ and the transition boiling state $sC$.

This model predicts a superheat temperature, where nucleate boiling would be triggered in the spots of the droplet protrusions, effectively restricting any liquid-solid contact. This model is appealing because it introduces no additional physics and relies only on the reduction of the contact area. The following comparison with experimental results shows deviations.

The transition boiling state $sC$ at $p = 0.1$ MPa extends up to $T_t = 433$ K, i. e. at $T_c = 424$ K. The superheat according to equation (4.3) of $45.9$ K corresponds to spot areas of $A = 5.4 \cdot 10^{-3}\ \text{mm}^2 = 5400\ \mu\text{m}^2$. This is a relatively small area when compared to observed thickness of the droplet "feet" in transition boiling state. At elevated pressure of $p = 1.7$ MPa the transition regime reaches $T_t = 623$ K, thus $T_c = 602$ K. The superheat shifts to 125 K with corresponding spot areas of $A = 2.7 \cdot 10^{-5}\ \text{mm}^2 = 27\ \mu\text{m}^2$, which are definitely smaller, than the observed protrusions. There is no explanation for the difference in the superheats at different pressures.Thus, additional reasoning for the difference in superheats at the different pressures is needed.

Therefore, a better understanding of pressure effects and fluid dynamics of the oscillating fluid interface in the transition state and subsequently, of the levitated droplet in the rebound state is required to explain the trends.

#### 4.2.2.3 Bubble coagulation and foam cushion

The bubble coagulation model is presented here as it shows an approach of an increasing temperature after onset of nucleate boiling and incorporates state-of-the-art boiling concepts. The model has the potential to follow the increase in temperature for the initiation of transition boiling $sC$ by the change in fluid properties. The decrease of surface tension with increasing saturated boiling pressure, decreasing latent heat of evaporation and the increase of vapor density are the ma-

jor changes in water properties encountered, which affect bubble growth ratio and mass evaporation rate.

At temperatures above ONB the water droplet still wets the surface, but the liquid is displaced dynamically by the growing vapor bubbles. The occupation of the contact area by the bubbles leads to a decrease of the contact area between liquid phase and the target. Moreover, parts of liquid can be trapped between three growing bubbles and be lifted above the heater, as marked by the dashed area in figure 4.9, and in that way evade participating in the heat transfer.

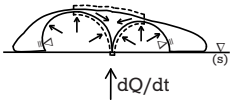


**Figure 4.9.:** Vapor bubbles entrap liquid

The working hypothesis here is that the lifting by bubbles can be modelled with a statistical approach.

#### 4.2.2.3.1 Percolation threshold

Bubble origin, bubble growth initiation and the fluid mixing in the liquid phase are processes which are non-deterministic on the length scale of a bubble. Coagulation of an ensemble of bubbles involves bubble interaction and is therefore regarded as being inappropriate for direct modeling or stochastic treatment. Percolation theory deals with macroscopic effects of stochastic processes.

The droplet forms a small pool on the wetted area $A_{drop}$ from equation (4.1). Coagulated clusters of vapor bubbles form as soon the conditions for a two-dimensional percolation of round disks, of radius $r$, over the target plane in the system, with characteristic size of the droplet area $A_{drop}$, are met.

The cumulative ratio of droplet area occupied by the bubbles, the occupation ratio $\gamma$ is

$$\gamma = \frac{\sum_{i=1}^{N_{bubbles}} A_i}{A_{drop}} \tag{4.9}$$

The critical value of $\gamma$ is compared with the critical total area for disks $\eta_c = \pi r^2 N/L^2$, where $N$ is the number of objects and $L$ is the system size in (Mertens & Moore, 2012). By assuming constant spatial distribution of active nucleate sites and sufficient overheat to activate multiple sites, $\gamma = \eta_c$. The bubbles can coagulate in the process and the disks overlap, therefore the cumulative occupied area is

generally higher than the projected area of obstruction and the occupation ratio can be higher than one.

The effect of equation (4.9) is illustrated in figure 4.10. Bubbles coagulate to clusters at an occupation ratio of $1.1$ and above. The numerically determined percolation threshold is $\gamma_c = 1.12808737 \pm 6 \times 10^{-8}$ (Mertens & Moore, 2012).

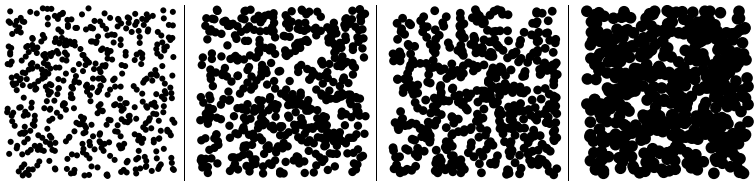

**Figure 4.10.:** Visualization of percolation with $\gamma = \{0.5, 1.0, 1.1, 2.0\}$

#### 4.2.2.3.2 Bubble growth

To quantify the effect of coagulated bubbles, $\gamma$ is expressed in experimental quantities according to the theory on the boiling of fluids under free convection.

The droplet contact area is taken from the droplet spread diameter in equation (4.1). The number of bubbles is assumed to be equal to the number of active nucleation sites from equation (4.3).

For the cumulative area of the bubbles, one has to consider the temporal growth rate of the bubbles, where bubble radius is proportional to square root of time (Kutateladze, 1979, eq. (45)). Thus, the area of each bubble is growing linearly with time. The mean bubble area is $1/2$ of the maximal bubble area which is given by the maximal bubble diameter, the bubble departure diameter $D_b$. For the calculation of the bubble departure diameter exist empirical correlations, like

$$D_b = 0.851\ \theta_0 \sqrt{\frac{2\,\sigma}{g\,(\rho_l - \rho_v)}} \tag{4.10}$$

where $\theta_0$ is the contact angle of vapor bubbles in radians, $\theta_0 = 0.7$ in the present case (Baehr & Stephan, 2006a, eq (4.85)). This correlation is based on the force balance of surface tension and gravity and has the pressure dependent parameters surface tension and gas density. On the other hand, shear flow during droplet impact and flow inside the departing droplet would disturb the force balance. As is shown in the chapter before, the influence of liquid viscosity is significant for initiation of boiling at elevated chamber pressure, thus a more general model is used below.

As bubble formation involves instationary flows of liquid and gas phase, buoyancy effect, surface tension and evaporation, "there is no generalized correlation for the bubble departure diameter" (Dhir et al., 2007, p. 609), but several specific correlations are discussed in the cited report.

The empirical correlation in (Kutateladze, 1979) combines these effects by non-dimensional numbers and retains validity at elevated pressures. We use this theory for further calculation of the bubble departure diameter:

$$D_b = \delta_* \, 0.25 \, \sqrt{1 + 10^5 \, K_{**}} \tag{4.11}$$

with the similarity criterion $K_{**}$

$$K_{**} = (\frac{Ja}{Pr})^2 \frac{1}{Ar_*} \tag{4.12}$$

and the Archimedes number $Ar_*$

$$Ar_* = \frac{g \, \delta_*^3}{\nu^2}(1 - \frac{\rho_v}{\rho_l}) \tag{4.13}$$

and the Prandtl number $Pr = c \, \mu/\kappa$, the Jakob number $Ja = \frac{\rho_l}{\rho_v} \frac{c_{p,l}(T_{sat} - T_c)}{h_{ev}}$ and the capillary length $\delta_* = \sqrt{\frac{\sigma}{g \, (\rho_l - \rho_v)}}$ (Kutateladze, 1979, eq. (54)).

The bubble diameter at departure is correlated by *Cole and Rohsenow* in (Dhir et al., 2007, eq. (6)) for water boiling at variable pressures below standard pressure which leads to the assumption that this correlation might fit also at elevated pressure:

$$D_b = 1.5 \times 10^{-4} \sqrt{\frac{\sigma}{g \, (\rho_l - \rho_v)}} \, Ja^{*5/4} \quad Ja^* = \frac{\rho_l}{\rho_v} \frac{c_{p,l} T_{sat}}{h_{ev}} \tag{4.14}$$

The typical observed bubble size is $1$ mm at $0.1$ MPa in figure 4.2(f) and $0.3$ mm at $0.9$ MPa in figure 4.3(c), giving estimates of the bubble departure diameter of $2$ mm and $0.6$ mm, respectively. While the prediction from equation (4.11) is in an other order of magnitude ($4.8$ m, $0.6$ m) and the prediction from equation (4.10) seems not to follow the trend at $0.9$ MPa ($2$ mm, $1.7$ mm), the prediction from equation (4.14) ($2.3$ mm, $0.2$ mm) seems to scale appropriately an is taken for further $D_b$ calculations.

The bubble departure diameter and the number of nucleation sites are the main factors for the percolation hypothesis. The dependence of $N_s$ and $D_b$ on pressure determines the outcome prediction. $D_b$ is modeled with empirical pressure dependence in material properties, like vapor density $\rho_v$, while pressure dependence of $N_s$ is connected to the saturated vapor pressure.

#### 4.2.2.3.3 Percolation condition

With increasing temperature, the occupied area fraction $\gamma$ increases because of the increase in the number of active nucleation sites and the increase in the area occupied by the particular bubbles. As soon as $\gamma$ reaches $\gamma_c$, continuous channels of vapor form between the droplet and the heated wall, obstructing the liquid flow from reaching the wall surface

$$hP \Rightarrow \gamma = \frac{N_s \; D_b}{2 \; A_{drop}} \leq \gamma_c \tag{4.15}$$

This is seen as the first kind of crisis and an insulating layer expected with increasing temperature, which should form a kind of *foam cushion*.

The corresponding contact temperature is calculated from this set of equations for different pressure values and plotted in the discussion of the experimental results as the percolation hypothesis, $hP$, in figure 4.12.

This mechanism is also proposed as an explanation of the shoulder in droplet residence time in the present experiment. The growing bubbles insulate the liquid from the wall and obstruct the flow of liquid to the wall. Eventually, as the bubble membranes disintegrate, a clear passage of gas is seen underneath the droplet. Hence, the residence time in the transition regime corresponds to the characteristic bubble growth time. The classic macroscopic measurement of droplet evaporation time, or, as otherwise called, droplet lifetime, would not detect such a lifted state directly, but via an inflection point in the lifetime. Soon after the collapse of the bubble membranes, vapor can escape from the base of the droplet, allowing it to land again on the target. The subsequent takeoff and landing of the droplet have a typical frequency of 0.1 kHz and are typically not detected macroscopically, so cumulative evaporation time is reported in (Gottfried et al., 1966; Biance et al., 2003; Anokhina, 2010).

Vibrations, as shown in figure 4.11 for a droplet at $p = 0.9$ MPa and $T_t = 563$ K, which are observed in the experiments, also lead to contact of the droplet to the heated surface with duration of some milliseconds.

As this dynamic behaviour of the droplets involve complex motion of the fluids, modeling of this regime is impractical. The residence time of the droplet upon the heated target surface is recorded to provide a quantification of the phenomenon and to facilitate further model validations.

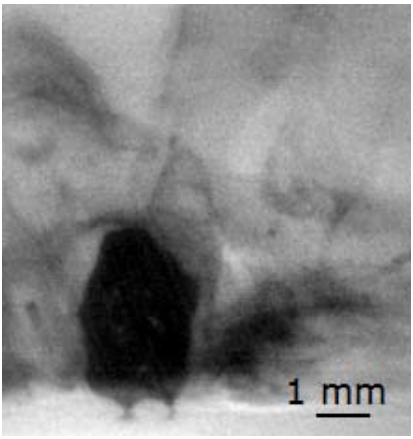


**Figure 4.11.:** Dancing droplet

#### 4.2.2.4 Stability of the evaporation interface

At small superheats, typical for nucleate boiling regime, evaporation is triggered by some nucleus and a bubble starts to grow as discussed (Scriven, 1959; Kutateladze, 1979). With increased superheat, a faster evaporation front can occur at the moving interface itself (Aktershev & Ovchinnikov, 2008, see Fig. 1), which can move on faster through the superheated fluid part, than the nucleated bubble.

The flow crisis of the first order in bulk liquids is analogous to the obstruction of flow by bubbles (Mayinger, 1984). The second crisis, i.e. some kind of DNB should be observable. The concept of evaporation fronts is also discussed for DNB in bulk liquid boiling setups (Stutz & Simões-Moreira, 2013).

This second order transition of the boiling system can be considered as a reactive interface flow. In a chemical reaction, like a premixed flame, energy is stored in the molecular structure of the fuel and the oxidizer. Analogously, energy is stored in the molecular attraction forces of the overheated liquid. A heat release reaction is triggered on the interface and expanding gaseous vapor is leaving the interface. As suggested by *F. E. Marble*, the Landau-interface instability (Landau, 1944; Landau & Lifshitz, 1987) could be relevant for the critical overheat and a new flow pattern (Shepherd & Sturtevant, 1982). In a classical treatment of a combustion setup, the fluid, typically a gas, expands after a chemical reaction in a plane and slightly perturbed flame front region with negligible thickness. Fluid

flow on evaporation of superheated liquid were analysed analogous to the reaction front also in (Prosperetti & Plesset, 1984; Higuera, 1987; Shusser & Weihs, 2001).

The reported instability conditions are

$$
\begin{aligned}
& j^4 \geq 4\ \sigma\ g\ \rho_l\ \rho_v^2\ , \\
& j \geq \sqrt{\tfrac{2\ \rho_l\ \rho_v}{3}}\ \sqrt[4]{\tfrac{\sigma\ g}{\rho_l}}\ ,\ j^4 \geq (4/9)\ \sigma\ g\ \rho_l\ \rho_v^2 \\
& j^4 \geq max(k_r\ ,\ \sigma\ g\ \rho_l\ \rho_v^2)
\end{aligned}
\tag{4.16}
$$

where $j$ is the mass flux through the liquid-vapor interface and $k_r$ is a criterion on radial instability (Landau & Lifshitz, 1987), (Prosperetti & Plesset, 1984, eq. (70)) and (Higuera, 1987, eq. (18)).

Typically the analysis of such a stability problem at an approximative step neglects the influence of the surface tension, as it is nonexistent in gases and its effect in water is minimal on the length scale above centimeters. However, in the experiment of this study, $D_0 < L_{cap}$. The bottom layer of a droplet in the transition to the Leidenfrost regime, which is superheated, has a thickness below $0.5$ mm, which further reduces the influence of gravity relative to surface tension. The results of the studies cited above cannot be taken directly, as the terms involving $g$ collapse, when one tries to neglect gravity, with the horizontal or upside-down direction of the interface movement.

The analysis of the interface stability problem starts with the characteristic equation for disturbance growth (Landau & Lifshitz, 1987). Details on the calculations are provided in form of an algebra system script (Wolfram Research, 2010) in chapter F.3. Reducing the characteristic equation to the criterion, where the real part of the alternating term of the solution for the growth rate becomes positive, leads to the instability condition

$$
j \geq \sqrt{\frac{\rho_l\ \rho_v\ (k^2\ \sigma + g\ (\rho_l - \rho_v))\ (\rho_l + \rho_v)}{k(\rho_l^2 + \rho_l\ \rho_v - \rho_v^2)}}
\tag{4.17}
$$

where $k$ is the wave number (Landau & Lifshitz, 1987). This instability condition includes the dependence on gravity and surface tension.

Evaporative mass flux $j$ needs to be connected to some kind of reaction model, so the instability condition can be expressed in material properties. The evaporation rate depends on density difference between superheated and saturated vapor (Prosperetti & Plesset, 1984, eq. (12)) by the Hertz-Knudsen equation

$$j = \sqrt{\frac{R\,T_c}{2\pi\,M}}(\rho_{v,sat,T_c} - \rho_v) \tag{4.18}$$

where $R$ is the universal gas constant, $M$ is the molar weight of water, $\rho_{v,sat,T_c}$ is the equilibrium saturated vapor density at contact temperature and $\rho_v$ is the saturated vapor density at the experiment pressure.

Therefore, equation (4.17) is solved for $T_c$:

$$T_c \geq \frac{2M\pi\rho_l\rho_v(\rho_l + \rho_v)(g(\rho_l - \rho_v) + k^2\sigma)}{kR(\rho_l^2 + \rho_l\rho_v - \rho_v^2)(\rho_v - \rho_{v,sat,T_c})^2} \tag{4.19}$$

The wave number $k$ in equation (4.17) identifies characteristic perturbation size range for a given set of parameters. $k$ is the spatial period of a sine-type perturbation. Growing perturbations are assumed to compete for energy stored in the steadily superheated fluid, so the first instability occurs for $k$ with the lowest onset temperature.

The minimum temperature in respect to $k$ for equation (4.19) is calculated by the Fermat's theorem, see also input number 22 in chapter F.3, testing for the first and the second derivatives. Thus, $k_0$ for the onset of instability is

$$k_0 = \sqrt{\frac{g\,\rho_l - g\,\rho_v}{\sigma}} \tag{4.20}$$

Temperature from equations (4.19) and (4.20) is tested in the discussion of the experimental results. The corresponding temperature and pressure values for this condition are plotted as the line for the Landau instability hypothesis, $hL$, in figure 4.12.

$$hL \Rightarrow T_{c,0} = \frac{4M\pi\rho_l\rho_v(\rho_l + \rho_v)\sqrt{g(\rho_l - \rho_v)}\sigma^{3/2}}{R(\rho_l^2 + \rho_l\rho_v - \rho_v^2)(\rho_v - \rho_{v,sat,T_c})^2} \tag{4.21}$$

A range of instable perturbations is predicted for $T_c > T_{c,0}$ due to the structure of equation (4.19) of kind $T_c \geq A\,(B + k^2)/k$.

The characteristic length, $2\pi/k_0$, is the spatial period of the first disturbance. In difference to bulk liquid boiling setups, in our experiment exists an upper geometrical limit for the range of realizable values of this length, the initial droplet size $D_0 = 2.4$ mm and the size of the spread droplet $D_{max}$. For pressure from $0.1$ to

2.5 MPa the values of $2\pi/k_0$ decrease from 1.8 mm to 1.1 mm. Thus, geometrical limitation of the droplet is irrelevant for this hypothesis.

The concept of evaporation of superheated water can be also seen from the thermal point of view. Just after the first contact of the droplet with the wall, on the time scale of nanoseconds, the lower part of the water is superheated according to the temperature profile in figure 2.1. Superheated water on the bottom side of the droplet stores latent energy. The expansion of the fluid and the evaporation front are driven here by the release of the stored latent heat, analogous to a chemical potential. The energy potential of such a thermal hydraulic explosion of superheated water is in order of magnitude of 300 kJ/kg (Lienhard et al., 1986, fig. 19). This specific energy is approximately 8 % of the chemical energy released by detonating trinitrotoluene (TNT). The destabilizing effect of such an energy release can lead to DNB.

With sufficient superheat, evaporation of even a small layer of liquid could generate sufficient vapor volume and impulse to detach the droplet from the target. The velocity of the evaporation of this layer is expected to rise with increasing temperature until it is faster than the imaging detection. The released energy per superheated layer is expected to decrease with increasing temperature, as the build-up of the superheated volume is diffusion-driven and thus slower than the triggered bubble with evaporation. This can result in a macroscopically smooth rebound at high temperatures.

#### 4.2.2.5 Comparison of new models with experimental results

For comparison, the theoretical predictions for the $sB \vee sC$ transition are overlaid on the state map. The reduced pressure and the reduced contact temperature, $T_r = T_c/T_{crit}$, are used as scaling parameters, figure 4.12.

Surface tension of a fluid diminishes at its critical temperature. Therefore, the Landau instability line, $hL$, does not cross the critical temperature, this theory depends on the stabilizing effect of surface tension.

The $hP$-line according to equation (4.15) for the percolation theory is inside the transition regime. The $hP$-line is drawn for $p_r \leq 0.081$ as in this pressure range the numerical calculation converged. The overheat temperature is higher than 15 K and equation (4.4) was chosen for $N_s$ calculations. The percolation model follows the trend of the transition boiling initiation, albeit with some constant amount of reduced temperature deviation.

The nucleation site density, which is an external model for both the nucleation with limited contact area and the percolation approaches, may be reviewed before closing discussion on these hypotheses. Other reason for temperature differences could be the convective heat transfer due to flow inside the spreading droplet,

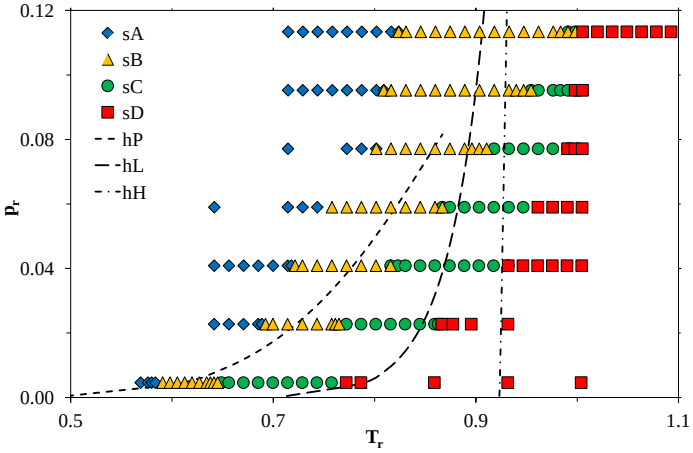


**Figure 4.12.:** Evaluation of new models on the onset of droplet levitation on the border between wetted boiling and transition boiling: $hP$ - Percolation condition from equation (4.15), $hL$ - Landau instability model from equation (4.21), $hH$ - spinodal line for homogeneous nucleation (Lienhard & Karimi, 1981) with equation (2.1), for orientation. Boiling states: wetting - $sA$, wetted boiling - $sB$, transition boiling - $sC$, rebound - $sD$. Map of boiling states scaled to reduced temperature and reduced pressure

as approached by equation (2.9). The size of the vapor bubbles for the percolation approach may be less, than assumed, because the spread droplet is shallower than the bubble departure size. The bubbles may disintegrate before departure, at smaller sizes than in the bulk liquid. This can effectively lower the occupied area ratio and rise the threshold temperature for percolation. Bubbles coagulate prior to departure at high temperature, but in a droplet with limited diameter the vapor can escape to the sides. This would decrease the lifting effect and leat to higher temperatures for the transition boiling state. These ideas could be followed by a future project.

The $hL$-line, depicting the onset of the Landau instability in equation (4.19), is inside the transition state, but not at the border to the rebound regime. The

Landau instability may be responsible for some of the changes inside the transition regime, but the predictions are sensitive on the assumption of the wave number $k$. Calculation converges in an interval from $1$ to $4000$, our assumption of the lowest-temperature-growing instability mode may be inferior to some more sophisticate model. In this form, the $hL$ approach deviates from the experimental results.

The models $hP$, $hL$ and also the homogeneous nucleation model $hH$ deviate from the experimental $sB \vee sC$ transition for departure from nucleate boiling. Therefore, a top-bottom approach is used further, the regression on the experimental results.

### 4.2.2.6 Experimental linear regression of reduced superheat

According to the corresponding states principle, the thermodynamic properties of many chemically different fluids can be calculated (VDI, 2010, p. 122).

In figure 4.13 the pressure and the contact temperature are scaled to the reduced pressure, $p_r = p/p_{crit}$, and to the reduced superheat above saturation temperature, $\underline{T} = (T_c - T_{sat})/T_{crit}$. The lines for vapor saturation $hS$ and the critical temperature of the fluid $hC$ are shown in figure 4.13 for orientation.

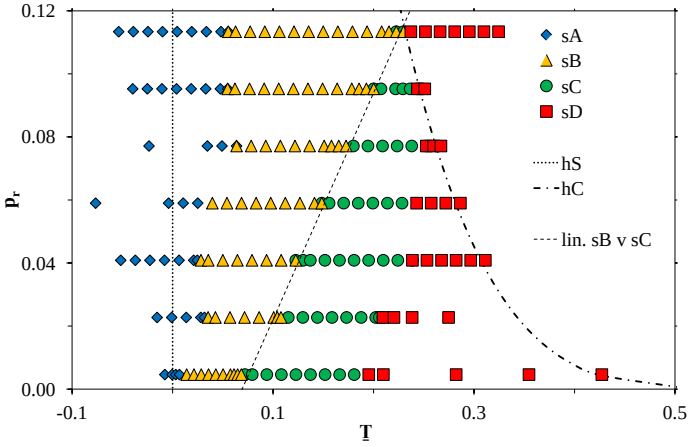


**Figure 4.13.:** Linear regression on the onset of droplet levitation: $hS$ - saturation temperature at the liquid-solid contact from equation (2.1), $hC$ - critical temperature of the fluid with equation (2.1), lin. $sB \vee sC$ - linear regression from equation (4.22). Boiling states: wetting - $sA$, wetted boiling - $sB$ transition boiling - $sC$, rebound - $sD$. Map of boiling states scaled to reduced superheat and reduced pressure

The idea behind this scaling is the *van der Waals*' interaction between fluid molecules, which is seen macroscopically as surface tension on the liquid-gas interface. With increasing temperature, the the dynamic energy of the molecules increases according to the kinetic approach, eventually overcoming molecular attraction. Thus for any fluid there exists a critical temperature $T_{crit}$, above which

the liquid-gas interface vanishes, at any pressure. The critical pressure $p_{crit}$ corresponds to $T_{crit}$ in the liquid-vapor critical point of the fluid.

Superheat is also a prominent parameter in phase transition theory and particularly in boiling theory. The heat energy stored in the fluid prior to phase transition is proportional to superheat, i.e. to the temperature difference between the equilibrium temperature and the local fluid temperature.

In this set of parameters, a linear regression on the position of a given regime border identifies the character of the effects as strongly connected the thermal properties of the fluid. Particularly, the linear regression

$$p_r = 0.7182\,\underline{T} - 0.0497 \tag{4.22}$$

on the border points between $sB$ and $sC$ scores a coefficient of determination of $R^2 = 0.988$. This suggests that the physics of the DNB process involves a linear relation according equation (4.22) of reduced pressure with the reduced superheat for the transition between nucleate boiling state $sB$ and transition boiling state $sC$. Similar ONB and inflection point linearities to the pressure are also reported qualitatively by *Satcunanathan* in the chapter on communications in (Temple-Pediani, 1969) for hydrocarbons.

To explore the underlying physics, we assume an infinitesimally small part of liquid in the contact region. The contact temperature is above saturation temperature, thus the liquid is superheated. The superheat is proportional by $c$ to the heat energy stored in the liquid, on top of latent heat of evaporation. This energy is released on evaporation, producing work on the generated vapor volume and the liquid-vapor interface. As proposal for future research, the solution of a model to account for energy transfer during evaporation could provide better understanding in light of the reduced superheat linearity equation (4.22).

### 4.2.3 Border of the transition state $sC$ and rebound state $sD$

For the change from transition boiling state to the rebound state on the $sC \vee sD$ border, referenced to as the fully developed film boiling, the approach of self-supporting vapor layer is proposed in (Gottfried et al., 1966) and by other studies. The underside of the impinging droplet has a complex, non-planar and non-spherical, shape as is modeled in (Roisman, 2010b) and experimentally shown in (Marengo et al., 2011; Tran et al., 2012). Generally, the generated vapor volume has to be equal to the vapor outflow on the near-wall rim of the rebounding droplet.

As the theory for the instationary flows and evaporation of the droplet is yet to be closed, this approach is a possibility for future research.

For comparison, the theoretical predictions for the $sC \vee sD$ border are overlaid with the state map. The reduced pressure and the reduced contact temperature, $T_r = T_c/T_{crit}$, are used as scaling parameters, figure 4.14.

Correlation coefficients of linear regressions of the borders of the boiling states are below $0.9$. This suggests a higher-order relation of $p_r$ with $T_r$ in a possible theoretical approach.

The spinodal line $hH$ in figure 4.14 marks the predicted homogeneous nucleation temperature of the contact region. Opposite to the suppose in (Bernardin & Mudawar, 1999), made at ambient pressure, also a linear relation of $p_r$ and homogeneous nucleation temperature of the contact region diverges from any of perceived state borders in the experiment.

The transition to the rebound state is completed always below the critical temperature in the contact area, according to equation (2.1), of the fluid. Above critical temperature water doesn't have an interface between liquid and vapor at any time scale. The contact region heats up and vaporizes instantaneously, actually there is no interface to measure the vaporization rates and times above critical temperature in the contact area. The nucleate boiling state $sB$ extends up to the critical temperature of $647$ K at the pressure of $2.5$ MPa, the transition boiling state $sC$ is then concentrated to this point.

Critical temperature of the fluid in the contact region, $hC$-line, is an upper bound to the boiling transition states at all pressures in the experiment. Even at elevated pressure, all droplets rebounded at temperatures $T_r \geq 1$.

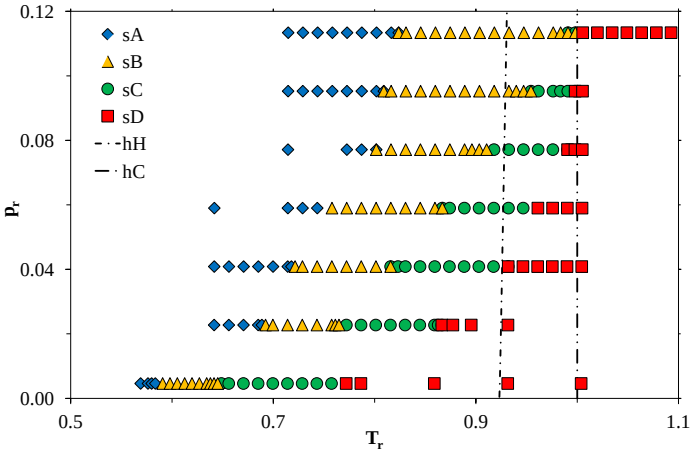


**Figure 4.14.:** Evaluation of models on the onset of droplet rebound: $hH$ - spinodal line for homogeneous nucleation (Lienhard & Karimi, 1981) with equation (2.1), $hC$ - critical temperature of the fluid with equation (2.1). Boiling states: wetting - $sA$, wetted boiling - $sB$ transition boiling - $sC$, rebound - $sD$. Map of boiling states scaled to reduced temperature and reduced pressure

# 5 Residence time

The residence time of the droplets upon the heated target surface, as defined in chapter one, is discussed in this chapter. The time for the wetting states correlates with the reported values at ambient pressure. Characteristic time thresholds correlate with the residence time with the impact outcomes. Thus, a quantification measure for the classification of the states is formulated.

## 5.1 Experimental results on residence time

Residence time $t_{inc}$ of the droplets was measured by counting the frames on the high-speed video.

For comparison, figure 5.1 depicts the lifetime data for water droplets (Anokhina, 2010) and the residence times of water droplets, with smaller initial size (Park et al., 2012), both at ambient pressure. Results here are consistent with the reported values. The changes in the slope of reducing residence times correspond to the changes in the slope of rising evaporation times in (Anokhina, 2010) at $425$ K ($152$ °C) and $473$ K ($200$ °C) at ambient pressure. The positive shift of the temperature with pressure is consistent with data on other fluids (Temple-Pediani, 1969).

The insulating effect of the vapor on the levitated droplet in boiling state $sC$ should cause the lifetime of the droplet to rise less than without such an effect with rising temperature, this effect is also seen macroscopically by the changed slope of the rising lifetime of a droplet at temperatures from $\approx$ $410$ K to $\approx$ $470$ K in (Anokhina, 2010).

At pressures above $1.3$ MPa, the dense air is refracting the light. Also, the water vapor is condensing in the vicinity of the droplet. This leads to a deteriorated image quality in the images, as the shape of the droplet and the existence of the gap are less certain for time measurements. Therefore, the residence time of the droplets and the diameter of the secondary droplets are measured, wherever possible.

In difference to the lifetime of the droplet, the residence time is decreasing with increasing temperature. The decrease down to relatively small time values on the time scale of $0.5$ ms is observed, which is also the temporal resolution limit of the recordings. While the droplet impacts the surface, even before capillary surface waves reach the top side of the droplet, one or more expansions of the vapor above

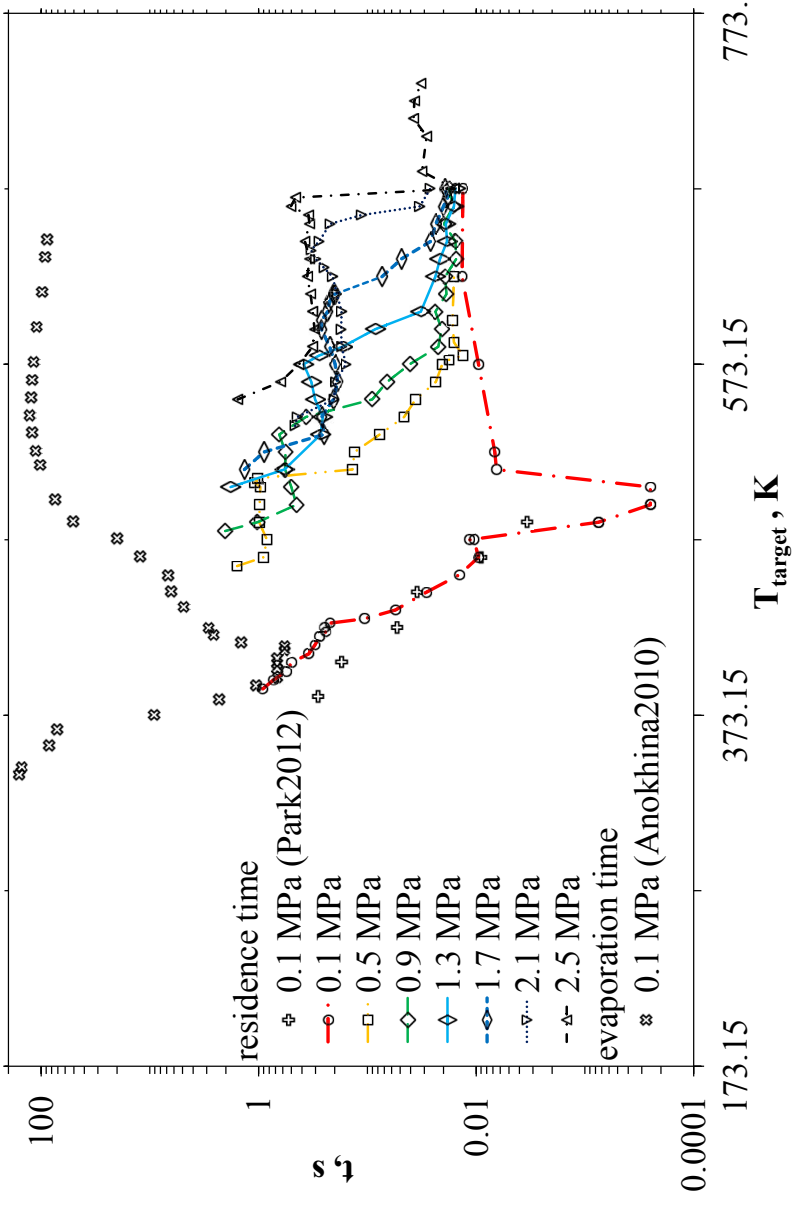


**Figure 5.1.:** Residence time for water droplets at different surrounding pressures as a function of target temperature. Results from (Park et al., 2012) and the evaporation time from (Anokhina, 2010) are added for reference

the surface cut off the contact between the droplet ant the heated surface, generating secondary droplets on the smallest detectable size order of magnitude, figure 5.2.

When the droplet is in the rebound state, the vapor generation is considered to be faster than the temporal resolution of the imaging. The residence time measured in the rebound state is then only a measure of an upper time bound of how long the droplet was nearer to the wall than the imaging spatial resolution of $43$ $\mu$m , the actual contact time of the target plate and the water might be smaller.

At temperatures for fully developed rebound state, the residence time approximates the value of $30\pm10$ ms. The characteristic time scale for droplet impact in the present setup is $t = D_0/U_0 = 4.8$ ms. Thus the endures $6.25$ time scales upon the target. This equals the estimated typical rebound time of a droplet on hydrophobic surface. Furthermore, this corresponds to the typical time for rebounding droplets on a hydrophobic surface in (Roisman et al., 2002, experiment 1,6,8), at ambient pressure. Residence time for all pressures approaches $30 \pm 10$ ms with increasing temperature, figure 5.1.

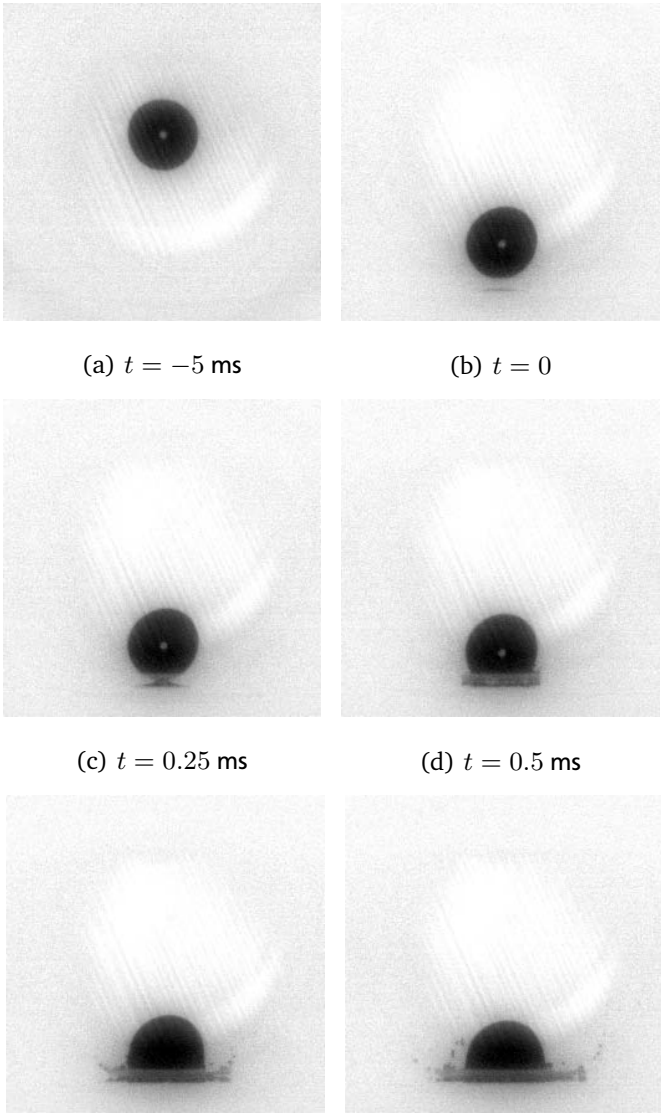

(a) $t = -5$ ms (b) $t = 0$

(c) $t = 0.25$ ms (d) $t = 0.5$ ms

(e) $t = 0.75$ ms (f) $t = 1$ ms

**Figure 5.2.:** Low residence time at $T_t = 493$ K and $p = 0.1$ MPa

## 5.2 Residence time and boiling states

In the transition state, the residence time experiences at least two pressure dependant decreases. Therefore, time thresholds can be used to distinguish the boiling states. Residence time dropping below $1.6 \pm 0.6$ s, corresponds to onset of boiling in the droplet, $sB$, figure 5.3. Residence time falling below $0.22 \pm 0.02$ s corresponds to the initiation of the observed transition $sC$ and is connected to the observation of the droplet levitated by vapour after initial wetting of the surface.

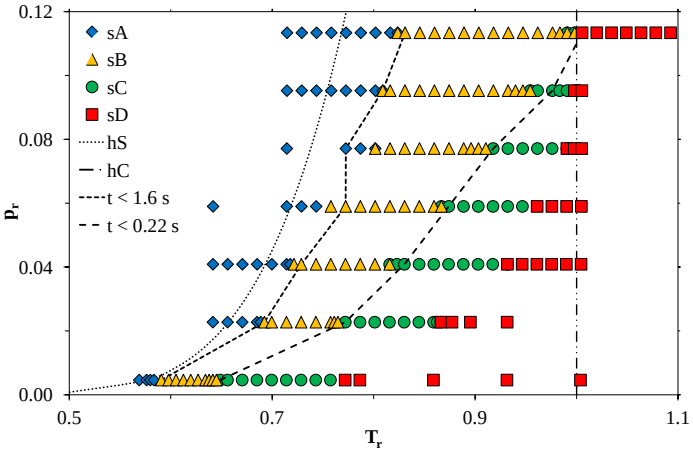


**Figure 5.3.:** Residence time thresholds of boiling states: $t < 1.6$ s - residence time threshold for onset of boiling, $t < 0.22$ s - residence time threshold for initiation of droplet levitation, $hS$ - saturation temperature at the liquid-solid contact, $hC$ - critical temperature of the fluid at the liquid-solid contact. Boiling states: wetting - $sA$, wetted boiling - $sB$ transition boiling - $sC$, rebound - $sD$. Map of boiling states scaled to reduced superheat and reduced pressure

Thus, measurement of the residence time provides a quantitative information for identification of the boiling state borders which is adequate to the phenomenological observation of the effect.

# 6 Secondary droplets

The impingement of a droplet is a discontinuous process. Out of particle sizing techniques suitable for instationary processes, imaging measurement technique is used for measurement of secondary droplets.

In this chapter, statistics on the secondary droplets are shown. The novel image processing algorithm used for this purpose is introduced, along with intermediate results. Bubble departure diameter correlates with the diameter of secondary droplets in the nucleate boiling state.

## 6.1 Image processing

For the characterisation of secondary droplets the images from the high-speed recordings are evaluated. Every high-speed recording is saved with the first image depicting the scenery just before the droplet becomes visible, see figure 6.1(a), as it moves into the field of view. The first frame of a recording is taken as a background reference, it is subtracted from the consecutive frames, so only differences, which are taking place during the recording become visible. Thus, the drift of illumination intensity due to aging of the LED, and dark regions of the image, which contain no detectable information, are eliminated.

The difference-image contains inhomogeneities of illumination due to optical abberations in the collimator, due to the non-uniform irradiance pattern of the LED and due to refraction of illumination by the heated air. To reduce the inhomogeneities, spatial filtering is performed. High spatial frequencies correspond to the particular edges of the droplets, while abberations have a low spatial frequency. Filtering is made therefore by a spatial FFT (fast Fourier transform) high-pass filter. The edge frequency of the filter is set by a factor of 1.5 lower, than the maximal expected droplet size of secondary droplets. In that way, the edges of the droplets are not diluted by the filtering step and the gray levels at the edge can be used for edge calculation without further corrections.

As the Fourier transformation is faster on square images and the central part of the image is containing the droplet images, the image is cropped to a square before filtering. Figure 6.2 shows the cropped image, the filtered image and, as a reference, the identified droplets projected as overlay upon the scene. According to the model shown in figure 3.4, local auto-threshold function (Schindelin et al., 2012) is used for edge detection. A table of all identified particles is collected which

(a) background image

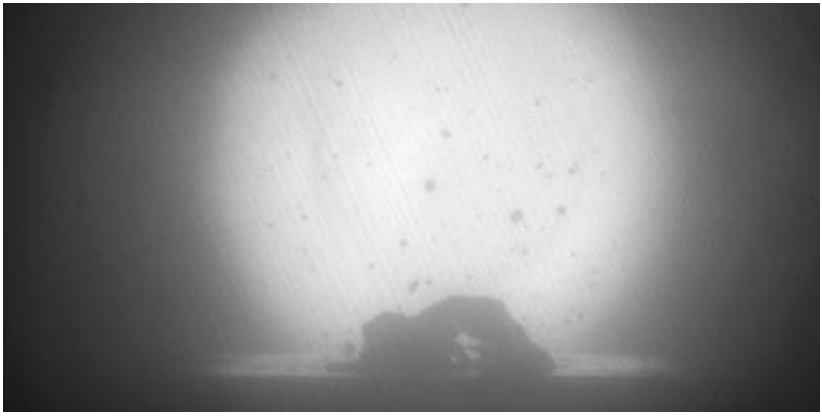

(b) analysed image

**Figure 6.1.:** Pre-processing of images

contains for each particle: the serial number of the particle in the image, the file path to the analysed image, the particle area in pixels and the interpolated centroid coordinates of the particle in horizontal and vertical direction. The table is stored in a comma separated format in a file for statistical analysis.

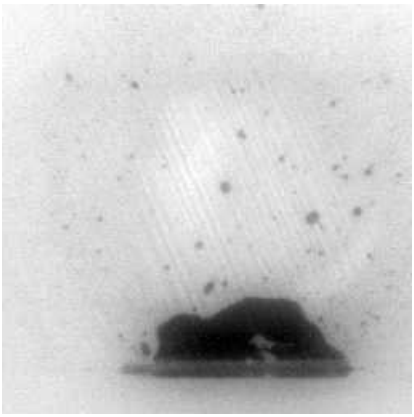

(a) cropped image

(b) filtered image

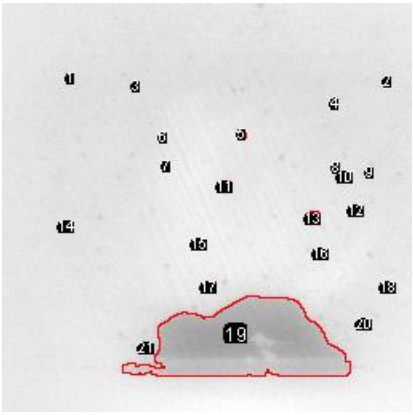


(c) particles overlayed

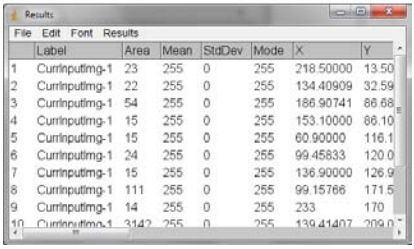


| | Label | Area | Mean | StdDev | Mode | X | Y |
|---|---|---|---|---|---|---|---|
| 1 | CurrInputImg-1 | 23 | 255 | 0 | 255 | 218.50000 | 13.50 |
| 2 | CurrInputImg-1 | 22 | 255 | 0 | 255 | 134.40909 | 32.59 |
| 3 | CurrInputImg-1 | 54 | 255 | 0 | 255 | 186.90741 | 86.68 |
| 4 | CurrInputImg-1 | 15 | 255 | 0 | 255 | 153.10000 | 86.10 |
| 5 | CurrInputImg-1 | 15 | 255 | 0 | 255 | 60.90000 | 116.1 |
| 6 | CurrInputImg-1 | 24 | 255 | 0 | 255 | 99.45833 | 120.0 |
| 7 | CurrInputImg-1 | 15 | 255 | 0 | 255 | 136.90000 | 126.9 |
| 8 | CurrInputImg-1 | 111 | 255 | 0 | 255 | 99.15766 | 171.5 |
| 9 | CurrInputImg-1 | 14 | 255 | 0 | 255 | 233 | 170 |
| 10 | CurrInputImg-1 | 3142 | 255 | 0 | 255 | 139.41407 | 209.0 |

(d) table of results

**Figure 6.2.:** Spatial filtering and particle recognition

## 6.2 Statistical analysis and data processing

During the measurement campaign, each of the recordings for every measured pressure-temperature combination is saved in a directory with the pressure and temperature setting saved inside the file name string. As the temperature stabilised quartz oscillator time base of the high-speed camera has an estimated accuracy

figure below $10^{-6}$, the timing of the images can be calculated by dividing of the image number by the frame rate of the recording, without further calibration. The readings of the chamber pressure, the target temperature and the time are read out of the file path string and converted to SI units. The contact temperature is recalculated from the target temperature by the use of the rearranged equation (2.1) and the thermal properties of the target alloy (Tappen, 2007).

The particles are quantified in the image processing step by the projected area in the object plane. This quantity is called $A$ (DIN, 2012). As preferred quantification parameter for particles, the area equivalent diameter $x_A$ is calculated for each particle as

$$x_A = \sqrt{\frac{4\ A}{\pi}} \tag{6.1}$$

The primary droplet is typically the largest particle in the field of view. To count only the secondary droplets, the measures of the largest particle in each image are discarded. Images, which contain no detected particles, or only one particle, i.e. the primary droplet, are therefore considered empty and not used further. The number of recognized secondary particles in a recording with manually observed secondary droplets is above $200$, corresponding to more than $0.3$ secondary particles per image. Recordings containing more than $200$ secondary particles are processed to calculate aggregate statistical values, like the Sauter mean diameter.

The aggregate measures of a particle distribution $q_r(x)$ connect the microscopic size values of the particles to the macroscopic measures of the ensemble, like the specific area or specific volume. These statistical figures correspond the physical properties of the particle ensembles, like solubility or stiffness. Such an aggregate descriptor is defined as the mean particle size $\overline{x}_{k,r}$ with the use of the moments of the particle distribution $M_{k,r}$ according to

$$\overline{x}_{k,r} = \sqrt[k]{M_{k,r}} = \sqrt[k]{\frac{M_{k+r,0}}{M_{r,0}}} \tag{6.2}$$

$$M_{k,r} = \int_{x_{min}}^{x_{max}} x_A^k\ q_r(x)\ \mathrm{d}x \tag{6.3}$$

where $k$ is the order of the moment and $r$ is the kind of the quantity, i.e. the dimensionality of the measure, like count, length, area or volume (DIN, 2006).

For chemical reactions, like combustion, and for evaporative processes, the mean volume-specific area $S_V$ of the particle ensemble is important for estimation of the reaction time, as mixing and reaction velocities are typically proportionally to the area of the particles, and the mass of the reagents is typically proportionally to the volume of the particles.

The mean volume-specific area can be calculated (DIN, 2006, eq. (35)) from the Sauter mean diameter (SMD) , which is $\overline{x}_{1,2}$ in equation (6.2)

$$S_V = \frac{6}{\overline{x}_{1,2}} = \frac{6}{M_{1,2}} = \frac{6\, M_{2,0}}{M_{3,0}} \tag{6.4}$$

Integration is made over the range of sizes from $x_{min}$ to $x_{max}$ according to all recognized particles. As the imaging technique does not detect very small particles, with $x_{min}$ typically equal $100\ \mu$m, their information is not contained in the statistical quantities. The particle count of the undetected particles might be quite large, but for the calculation of the volume-specific area the influence of those particles is small. The influence of small particles is leveraged by the exponential function in the moment calculation in equation (6.3), so the influence of undetected small particles on the statistical result is negligible.

## 6.3 Characteristics of secondary droplets

With the image processing method the secondary droplets during the impact are measured. A typical droplet volume distribution of secondary droplets during one droplet impact in the boiling region, at $p = 0.1$ MPa, $T_t = 425$ K, is shown in figure 6.3. The Sauter mean diameter of observed droplets is $0.4$ mm here.

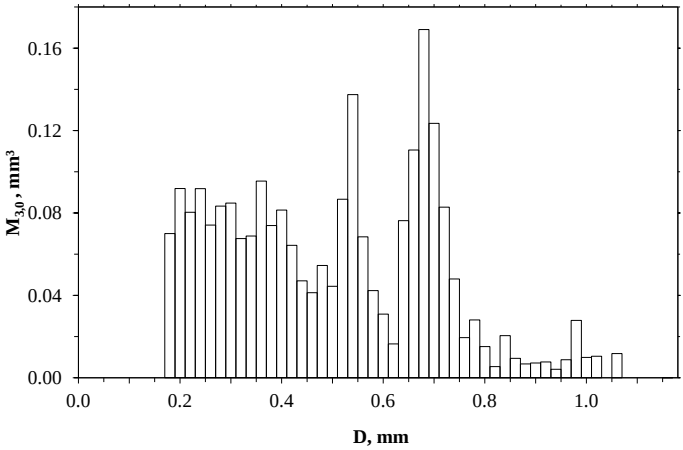


**Figure 6.3.:** Secondary droplet volume distribution

The volume distribution of either a complex or stochastic atomization process appears continuous, as there would be no characteristic droplet size prevailing. In the distribution above, the continuous part is seen at $M_{3,0} \leq 0.09$ mm$^3$, it goes down from a broad peak at droplet sizes of $0.3 \pm 0.1$ mm, up to $1.1$ mm. The distribution is truncated on the side of small particle sizes due to limitations of the measurement technique used.

As the shadowgraph is an imaging measurement technique, droplets smaller than one half of the spatial resolution, i. e. below $\approx 100$ $\mu$m, are not detected. As the mass contribution of the particles scales with the cube of the diameter size and the mean volume specific area of the small particles is higher than for the median-sized particles, the influence from undetected particles on the duration of evaporation is considered indecisive. Due to limited contrast of the recordings, the algorithm left particles below $0.16$ mm undetected, the spatial filtering by the optical lens and

the digital processing attenuated the image out of favor of the smallest detectable particles.

A notable feature in the volume distribution are the peaks of droplet volumes at the droplet size of $0.54$ mm and $0.68$ mm. These droplet sizes are higher represented in the recording, indicating, that these sizes are characteristic sizes for the breakup process, which generates the droplets. Thus, this supposes, that some part of the secondary droplet generation in boiling droplets is deterministic.

The spatial characteristic breakup-lengths correlate to temporal characteristics of droplet breakup, when one event leads to creation of multiple secondary droplets of similar size. Temporal evolution of the count of detected droplets per frame $N_d$ at $p = 0.1$ MPa, $T_t = 425$ K is shown in figure 6.4 .

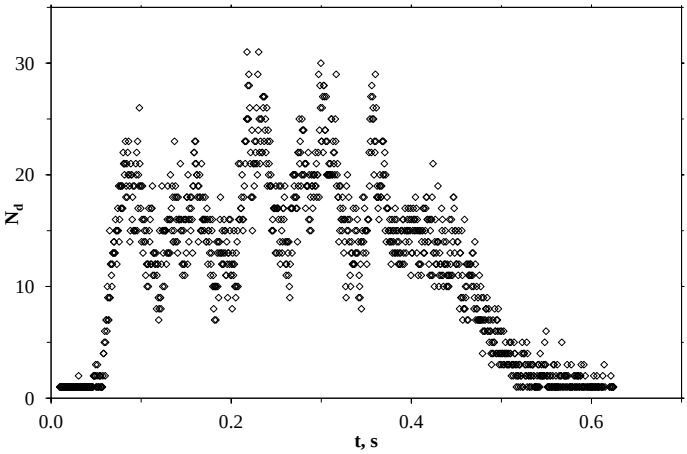


**Figure 6.4.:** Secondary droplet count during boiling

At $t < 0.05$ s the primary droplet impinges the target, spreads on the target and the liquid becomes overheated, boiling does not occur. At $t = 0.06$ s first secondary droplets are detected, they are visually confirmed to be parts from bubble lamella. Boiling proceeds to $t = 0.62$ s until the droplet is evaporated completely, up to $30$ particles are detected simultaneously in the field of view.

Secondary droplet generations proceeds in bursts, when major bubble disintegrations and simultaneous bubble collapses produce up to $15$ secondary droplets at

once, as can be seen at $t = 0.22$ s. The droplets liquid oscillates and a characteristic burst frequency of $1/(0.05 \pm 0.01)$ 1/s, as seen in figure 6.4.

For different pressures and temperatures, different mean droplet size values are measured. At high pressures, the detection of the droplets becomes difficult, as the increased density of air, higher amount of vapor dissolved in air and the fog out of condensate vapor induce additional shadows in the image, reducing the available signal-to-noise distance. Mean values are calculated only for measurement points with sufficient amount of the detected droplets.

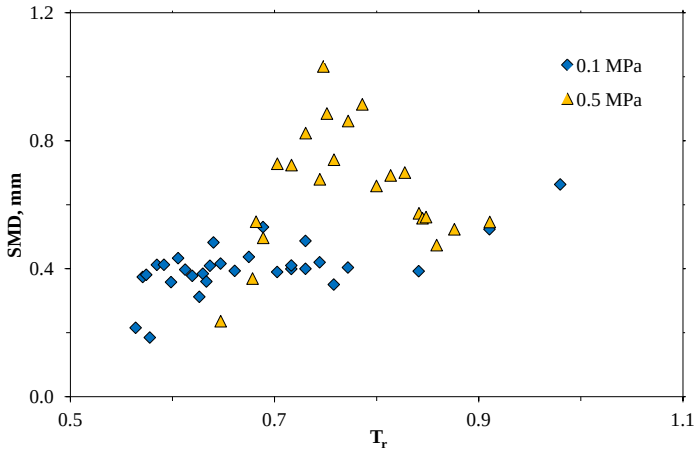


**Figure 6.5.:** SMD of secondary droplets

The Sauter mean diameter of the detected droplets is $0.4 \pm 0.1$ mm for $80\%$ of the measurements at $p = 0.1$ MPa, figure 6.5, while at $p = 0.5$ MPa there is a higher SMD of $0.8 \pm 0.2$ mm registered for $0.70 < T_r < 0.86$, corresponding to nucleate boiling and transition boiling states. This indicates, that the typical size of secondary droplets in boiling states is increasing with pressure.

The fluid flow in the nucleate boiling and transition states is extremely complex and escapes further modeling. Nevertheless, characteristic length scales of the flow are presented by the bubble departure diameter $D_b$ in equation (4.14).

The diameter of the detected secondary droplets in figure 6.3 exhibits characteristic peaks, which are observed to correlate to the temporal evolution of secondary droplets ind the boiling and transition states.

To explore the link between the bubble departure diameter and the secondary droplet diameter, the dependence of the Sauter mean diameter on the bubble departure radius is evaluated in the transition state. There seems to be an experimental correlation between the two values, figure 6.6.

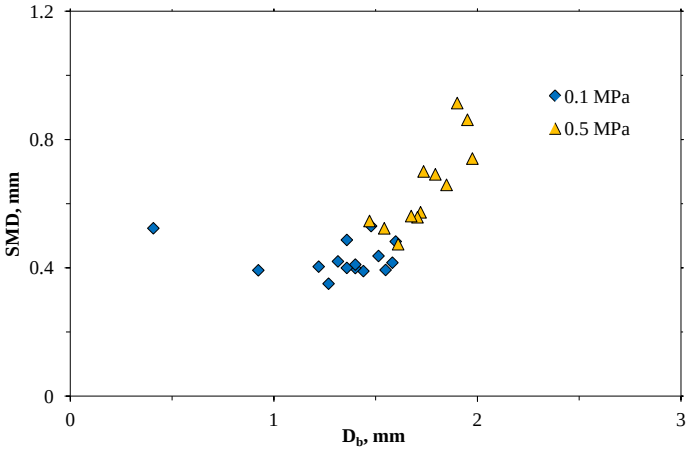


**Figure 6.6.:** SMD of secondary droplets in transition state over bubble diameter

In the transition regime the secondary droplet diameter increases with increasing pressure, also the bubble departure diameter increases with increasing pressure. The trend of the diameter of the secondary droplets may be due to the quantity of liquid in the bubble lamella, which is surrounding the bubble. The bubble lamella is stretched, while the bubble grows, thus an increased bubble diameter means a higher surface tension forces on the surrounding liquid. On bubble burst, more material is ejected in form of the coagulatig secondary droplets.

The model on the relation of the characteristic bubble departure diameter, characteristic lamella thickness and the characteristic diameter of secondary droplets could be an object for future study.

# 7 Conclusions and Outlook

Experimental results of this study include observation of boiling states, which shift in temperature at different levels of pressure: wetting, wetting with boiling, transition and rebound state. Residence times are measured for the different states and allow for quantification of the state transitions.

The four different states of droplet evaporation on a hot plate were observed. The limit criteria of these states were discussed based on published investigations on the Leidenfrost effect and also on theories for boiling and evaporative phase transition.

For the initiation of boiling, the theory based on nucleation site density in bulk liquids and projected at the contact area of the investigated droplet explains the measured superheat for onset of nucleate boiling at ambient pressure, as an extension to the theory of boiling into the setting of single drop impact. Taking into account the dependence of the saturated vapor temperature on the surrounding pressure, this theory follows the trend of the experimental results for onset of nucleate boiling, but shows increasing difference in temperatures with increasing pressure. The onset of boiling takes place above the predictions of the saturation and the nucleation theories, with the former one serving as a conservative lower temperature bound.

A novel nucleation model $hF$, accounting for the fluid flow inside the impacting droplet, agrees well with experimental results for onset of nucleate boiling in the impacting droplet.

For the transition from wetted boiling to levitated droplet state, different approaches were tested. Nucleation with limited contact area does not explain the superheats for the transition and rebound regimes. This could be either due to different nucleation conditions in superheat values of above $50$ K, which were studied neither in droplets nor in bulk liquids up to now, or due to other phenomena like bubble obstruction, evaporation waves and critical temperature of water.

The homogeneous nucleation model deviates from the observations. Theoretical approaches of bubble coagulation and Landau-instability are proposed as possible explanations. The bubble percolation model follows the trend of the experimental results and the Landau instability model is in the range of the observed transition state, but both models are deviating, calling for a review of the assumptions on nucleation site count, bubble interaction and the critical wave number of the instabilities.

The experimentally observed onset of the transition state exhibits a linearity between the reduced pressure value and the reduced contact overheat as shown in equation (4.22).

Together with the upper temperature bound for onset of rebound state, this leads to a vanishing transition state at pressures above $2.5$ MPa. This result has a direct benefit for possible relaxation of design constraints for certain heat exchanger configurations.

For the transition from temporarily levitated droplet to the rebound state, the critical temperature of water serves as an upper bound for transition temperature at all elevated pressures in this study.

The Leidenfrost temperature identified under ambient pressure is equal to the reported value (Baumeister & Simon, 1973).

Residence time in wetted boiling state is also the evaporation time of the droplets. In the transition state the residence time decreases in a similar manner, as the evaporation time increases, as both are connected to the dynamics of boiling. Residence time thresholds of $1.6 \pm 0.6$ s and $0.22 \pm 0.02$ s mark the observed transition state, with onset and departure from nucleate boiling respectively. Residence time approximates the characteristic rebound time of $30 \pm 10$ ms in the rebound state.

The residence time thresholds follow the observed state borders in the pressure-temperature map at all pressure values. Measurement of the residence time therefore provides quantitative information for identification of the boiling state borders, which provides similar results to observation of the impact.

Secondary droplets generated by boiling are detected and characterized. Secondary droplets are detected with the shadowgraph technique. For characterization of the secondary droplets a new image processing algorithm was developed. It is based on the irradiance model of a semi-infinite screen. Sauter mean diameter of the secondary droplets in transition boiling state increases with increasing pressure. An increasing dependence of the Sauter mean diameter of secondary droplets and the bubble departure diameter was observed.

A deeper understanding of departure from nucleate boiling and of the Leidenfrost effect can enable engineers to utilize the evaporative potential for various applications. In (Temple-Pediani, 1969) the Leidenfrost effect is considered to be suppressed for fuels in a typical diesel engine. There is a possibility of reintroducing boiling effects in diesel fuel by the use of binary fuels, i.e. via pre-injection of water or via emulsified fuels.

Inducing micro-explosive evaporation of the water may speed up overall fuel evaporation. Such a mechanism could explain better combustion outcomes with emulsified fuel reported in (Maiboom & Tauzia, 2011).

# 8 Acknowledgements

I wish to express my thanks to Prof. Dr.-Ing. Dr.-Ing. habil. Cameron Tropea and Priv.-Doz. Dr.-Ing. habil. Ilia Roisman for giving me the opportunity to conduct the research at the Institute of Fluid Mechanics and Aerodynamics, Technische Universität Darmstadt. I thank both Prof. Tropea and Dr. Roisman for their advice, guidance and fruitful discussions.

I would also like to thank Prof. Dr.-Ing. Peter Stephan for kindly accepting to be the second referee and for scientific advice.

My thanks go to my grandparents Annette Fischer and Samuel Buchmüller, who taught me persistence by example and always aim high in spite of all hardships.

I owe my gratitude to my brother Robert Buchmüller for the early experiments in rocket science, his present support and comments on the drafts. Very important are my parents Valentina Kartaschowa and Gregor Buchmüller who taught me, among many things, to ask for reasons behind everything, to try to understand, leading me to the field of research. I thank them all for supporting and blessing me in my endeavours and giving me all the opportunities I have.

I am greatly indebted to my grandfather in law, Dr. S. V. Gupta for his expert suggestions, moral support and spending much time in reading the drafts.

I am grateful to my parents in law Dr. Shyam S. Agrawal and Neelam Agrawal for their blessings and their continuous support regarding this work. I would also like to sincerely thank my brother in law Virupaksh Agrawal for his helpful comments on the various drafts and the interesting discussions around the topic.

I wish to express my cordial thanks to my beloved wife Bhumija Agrawal for her support and endless encouragement over the years.

Last but not least, I thank the colleagues from the institute along with the international cooperation partners for their suggestions, and to all my students and helpers in the laboratory for supporting with the load of experimental work.

I gratefully acknowledge financial support from the Deutsche Forschungsgemeinschaft (DFG) in the framework of SFB-TRR 75 "Tropfendynamische Prozesse unter extremen Umgebungsbedingungen", subproject C4.

# Appendix

# A Bibliography


Adrian, R. J. (1991). Particle-imaging techniques for experimental fluid mechanics. *Annual Review of Fluid Mechanics*, *23*(1), 261–304.

Aktershev, S. P., & Ovchinnikov, V. V. (2008). Model of steady motion of the interface in a layer of a strongly superheated liquid. *Journal of Applied Mechanics and Technical Physics*, *49*(2), 194–200.

Anokhina, E. (2010). Investigation of evaporation and boiling of liquids. *Technical Physics*, *55*, 1107–1112.

Ashgriz, N. (Ed.) (2011). *Handbook of Atomization and Sprays: Theory and Applications*. Springer Heidelberg.

Baehr, H. D., & Kabelac, S. (2005). *Thermodynamik: Grundlagen und technische Anwendungen*. Springer Heidelberg, 12th ed.

Baehr, H. D., & Stephan, K. (2006a). *Heat and Mass Transfer*. Springer Heidelberg, 2nd ed.

Baehr, H. D., & Stephan, K. (2006b). *Wärme- und Stoffübertragung*. Springer Heidelberg, 5th ed.

Basu, N., Warrier, G. R., & Dhir, V. K. (2002). Onset of nucleate boiling and active nucleation site density during subcooled flow boiling. *Journal of Heat Transfer*, *124*(4), 717–728.

Baumeister, K. J., & Simon, F. F. (1973). Leidenfrost Temperature - Its Correlation for Liquid Metals, Cryogens, Hydrocarbons, and Water. *Journal of Heat Transfer*, *95*(2), 166 – 173.

Bennett, J., Bhasin, A., Grant, J., & Lim, W. C. (2007). *Chemical Process Dynamics and Controls*. University of Michigan, Ann Arbour. Section: PID tuning via classical methods.

Bernardin, J., & Mudawar, I. (2007). Transition Boiling Heat Transfer of Droplet Streams and Sprays. *ASME Journal of Heat Transfer*, *129*, 1605–1610.

Bernardin, J. D., & Mudawar, I. (1999). The Leidenfrost Point: Experimental Study and Assessment of Existing Models. *ASME Journal of Heat Transfer*, *121*(4), 894–903.

Bernardin, J. D., & Mudawar, I. (2002). A Cavity Activation and Bubble Growth Model of the Leidenfrost Point. *ASME Journal of Heat Transfer*, *124*(5), 864–874.

Bernardin, J. D., & Mudawar, I. (2004). A Leidenfrost Point Model for Impinging Droplets and Sprays. *ASME Journal of Heat Transfer*, *126*, 272–278.

Bernardin, J. D., Stebbins, C. J., & Mudawar, I. (1996). Effects of surface roughness on water droplet impact history and heat transfer regimes. *International Journal of Heat and Mass Transfer*, *40*(1), 73 – 88.

Bernardin, J. D., Stebbins, C. J., & Mudawar, I. (1997). Mapping of impact and heat transfer regimes of water drops impinging on a polished surface. *International Journal of Heat and Mass Transfer*, *40*(2), 247 – 267.

Berrocal, E., Kristensson, E., Sedarsky, D., & Linne, M. (2009). Analysis of the SLIPI technique for multiple scattering suppression in planar imaging of fuel sprays. In *Proceedings of the 11th International Annual Conference on Liquid Atomization and Spray Systems, Vail, CO, USA*. Curran Associates, Red Hook, NY, USA. ISBN 978-16-178265-3-5.

Bett, K. E., & Capi, J. B. (1965). Effect of Pressure on the Viscosity of Water. *Nature*, *207*, 620–621.

Biance, A.-L., Clanet, C., & Quéré, D. (2003). Leidenfrost drops. *Physics of Fluids*, *15*(6), 1632–1637.

Biance, A.-L., Pirat, C., & Ybert, C. (2011). Drop fragmentation due to hole formation during Leidenfrost impact. *Physics of Fluids*, *23*(2), 022104.

Bohren, C., & Huffman, D. (1983). *Absorption and Scattering of Light by Small Particles*, vol. 1. J. Wiley and Sons, New York, Wiley-Interscience.

Brenn, G., Durst, F., & Tropea, C. (1996). Monodisperse sprays for various purposes-their production and characteristics. *Particle and Particle Systems Characterization*, *13*(3), 179–185.

Buchmüller, I., Roisman, I. V., & Tropea, C. (2012). Influence of Elevated Pressure on Impingement of a Droplet Upon a Hot Surface. In *Proceedings of the 12th Triennial International Conference on Liquid Atomization and Spray Systems, Heidelberg, Germany*. ISBN 978-88-903712-1-9.

Castanet, G., Dunand, P., Caballina, O., & Lemoine, F. (2013). High-speed shadow imagery to characterize the size and velocity of the secondary droplets produced by drop impacts onto a heated surface. *Experiments in Fluids*, *54*(3), 1–17.

Chatzikyriakou, D., Walker, S., Hale, C., & Hewitt, G. (2011). The measurement of heat transfer from hot surfaces to non-wetting droplets. *International Journal of Heat and Mass Transfer*, *54*(7-8), 1432–1440.

Debye, P. (1908). Das elektromagnetische Feld um einen Zylinder und die Theorie des Regenbogens. *Phys. Z.*, *9*(22), 775–778.

Dhir, V. K., Abarajith, H. S., & Li, D. (2007). Bubble Dynamics and Heat Transfer during Pool and Flow Boiling. *Heat Transfer Engineering*, *28*(7), 608–624.

DIN (2006). Darstellung der Ergebnisse von Partikelgrößen/-analysen - Teil 2: Berechnung von mittleren Partikelgrößen/-durchmessern und Momenten aus Partikelgrößenverteilungen (ISO 9276-2:2001); Representation of results of particle size analysis - Part 2: Calculation of average particle sizes/diameters and moments from particle size distributions (ISO 9276-2:2001).

DIN (2009). Industrielle Platin-Widerstandsthermometer und Platin-Temperatursensoren (IEC 60751:2008); Deutsche Fassung EN 60751:2008; Industrial platinum resistance thermometers and platinum temperature sensors (IEC 60751:2008); German version EN 60751:2008.

DIN (2012). Darstellung der Ergebnisse von Partikelgrößen/-analysen - Teil 6: Deskriptive und quantitative Darstellung der Form und Morphologie von Partikeln (ISO 9276-6:2008); Representation of results of particle size analysis - Part 6: Descriptive and quantitative representation of particle shape and morphology (ISO 9276-6:2008).

Engel, O. G. (1955). Waterdrop collisions with solid surfaces. *Journal of Research of the National Bureau of Standards*, *54*(5), 281–289.

Fairbairn, S. W. (1851). *Two Lectures: The Construction of Boilers, and on Boiler Explosions, with the means of prevention*. Reid Newsome, Leeds.

Fourier, J. B. J. (1822). *Théorie analytique de la chaleur*. Didot Paris.

Gottfried, B., Lee, C., & Bell, K. (1966). The leidenfrost phenomenon: film boiling of liquid droplets on a flat plate. *International Journal of Heat and Mass Transfer*, *9*(11), 1167–1188.

Gouesbet, G., & Gréhan, G. (2011). *Generalized Lorenz-Mie Theories*. Springer Heidelberg.

Gradeck, M., Seiler, N., Ruyer, P., & Maillet, D. (2013). Heat transfer for leidenfrost drops bouncing onto a hot surface. *Experimental Thermal and Fluid Science*, *47*(0), 14 – 25.

Graßmann, A., & Peters, F. (2004). Size Measurement of Very Small Spherical Particles by Mie Scattering Imaging (MSI). *Particle & Particle Systems Characterization*, *21*(5), 379–389.

Habchi, C. (2010). New Correlations for Leidenfrost and Nukiyama Temperatures with Gas Pressure-Application to Liquid Film Boiling Simulation. In *ILASS - Europe 2010, 23rd Annual Conference on Liquid Atomization and Spray Systems, Brno, Czech Republic*.

Haller, P. d. (1933). Untersuchungen über die durch Kavitation hervorgerufenen Korrosionen. *Schweizerische Bauzeitung*, *101*(21), 243–246.

Hecht, E. (2002). *Optics*. Pearson Education - Addison Wesley, San Francisco., 4th ed.

Hederer, H., Peter, S., & Wenzel, H. (1976). Calculation of thermodynamic properties from a modified Redlich-Kwong equation of state. *The Chemical Engineering Journal*, *11*(3), 183 – 190.

Higuera, F. J. (1987). The hydrodynamic stability of an evaporating liquid. *Physics of Fluids (1958-1988)*, *30*(3), 679–686.

Ho, W. K., Hang, C.-C., & Zhou, J. (1995). Performance and gain and phase margins of well-known PI tuning formulas. *Control Systems Technology, IEEE Transactions on*, *3*(2), 245–248.

Horne, R. A., & Johnson, D. S. (1966). The Viscosity of Water under Pressure. *The Journal of Physical Chemistry*, *70*(7), 2182–2190.

Hsu, Y. Y. (1962). On the Size Range of Active Nucleation Cavities on a Heating Surface. *Journal of Heat Transfer*, *84*(3), 207–213.

IAPWS (2007). *Revised Release on the IAPWS Industrial Formulation 1997 for the Thermodynamic Properties of Water and Steam*. NIST, Boulder, CO, USA.

Kretzschmar, P. H.-J., Stoecker, D. I., Jaehne, I., & Kunick, M. (2013). *Property Library for the Industrial Formulation IAPWS-IF97 for Water and Steam*. Hochschule Zittau/Goerlitz, Zittau, Germany.

Kunkelmann, C. (2010). Status report - project C1. *SFB-TRR 75 status meeting 2010*.

Kutateladze, S. S. (1979). Boiling and bubbling heat transfer under free convection of liquid. *International Journal of Heat and Mass Transfer*, *22*(2), 281–299.

Landau, L. (1944). On the theory of slow combustion. *Acta Physicochim. URSS*, *19*(1), 77–85.

Landau, L. D., & Lifshitz, E. M. (1987). *Course of Theoretical Physics, Fluid Mechanics*, vol. 6. Pergamon Press. See par. 128, problem 2.

Laven, P. (2003). Simulation of Rainbows, Coronas, and Glories by use of Mie Theory. *Appl. Opt.*, *42*(3), 436–444.

Laven, P. (2004). Simulation of rainbows, coronas and glories using Mie theory and the Debye series. *Journal of Quantitative Spectroscopy and Radiative Transfer*, *89*(1-4), 257 – 269.

Laven, P. (2005). How are glories formed? *Appl. Opt.*, *44*(27), 5675–5683.

Leidenfrost, J. G. (1756). *De aquae communis nonnullis qualitatibus tractatus*. [Typis Joan. Sebast. Straube, Acad. typogr.] Impensis Hermanni Ovenni, Univers. bibliopolæ.

Leidenfrost, J. G. (1966). On the fixation of water in diverse fire, de aqua communis nonnullis qualitatibus tractatus, 1756. *International Journal of Heat and Mass Transfer*, *9*(11), 1153–1166.

Li, H. (2013). *Drop Impact on Dry Surfaces With Phase Change*. Ph.D. thesis, TU Darmstadt, Darmstadt, Germany.

Li, R., Ashgriz, N., & Chandra, S. (2010). Maximum Spread of Droplet on Solid Surface: Low Reynolds and Weber Numbers. *Journal of Fluids Engineering*, *132*(6), 061302.

Lienhard, J., & Karimi, A. (1981). Homogeneous Nucleation and the Spinodal Line. *Journal of Heat Transfer*, *103*(1), 61–64.

Lienhard, J. H., Shamsundar, N., & Biney, P. O. (1986). Spinodal lines and equations of state: A review. *Nuclear Engineering and Design*, *95*(0), 297 – 314.

Linne, M. (2013). Imaging in the optically dense regions of a spray: A review of developing techniques. *Progress in Energy and Combustion Science*, *39*(5), 403 – 440.

Litz, L. (2013). *Grundlagen der Automatisierungstechnik. Regelungssysteme - Steuerungssysteme - Hybride Systeme*. Oldenbourg Wissenschaftsverlag Berlin, 2 ed.

Lock, J. A. (1995). Improved Gaussian Beam-Scattering Algorithm. *Applied Optics*, *34*, 559–570.

Mackowski, D., & Mishchenko, M. (2011). A multiple sphere T-matrix Fortran code for use on parallel computer clusters. *Journal of Quantitative Spectroscopy and Radiative Transfer*, *112*(13), 2182 – 2192.

Maiboom, A., & Tauzia, X. (2011). NOx and PM emissions reduction on an automotive HSDI diesel engine with water-in-diesel emulsion and EGR: An experimental study. *Fuel*, *90*(11), 3179 – 3192.

Manzello, S., & Yang, J. (2002). On the collision dynamics of a water droplet containing an additive on a heated solid surface. *Proceedings: Mathematical, Physical and Engineering Sciences*, *458*(2026), 2417–2444.

Marengo, M., Antonini, C., Roisman, I. V., & Tropea, C. (2011). Drop collisions with simple and complex surfaces. *Current Opinion in Colloid and Interface Science*, *16*(4), 292–302.

Mayinger, F. (1984). Sieden - Stabilisator und Störfaktor sicheren Betriebes. *Chemie Ingenieur Technik*, *56*(3), 169–179.

Mertens, S., & Moore, C. (2012). Continuum percolation thresholds in two dimensions. *Phys. Rev. E*, *86*, 061109.

Mie, G. (1908). Beiträge zur Optik trüber Medien, speziell kolloidaler Metallösungen. *Annalen der Physik*, *330*(3), 377–445.

Mollenhauer, K., & Tschöke, H. (Eds.) (2010). *Handbook of Diesel Engines*. Springer Heidelberg.

National Instruments, C. (2008). *LabVIEW™ PID Control Toolkit User Manual*. National Instruments, Corp., Austin, TX, USA.

Nukiyama, S. (1934). The Maximum and Minimum Values of the Heat Q Transmitted From Metal to Boiling Water Under Atmospheric Pressure. *Journal of Japan Society of Mechanical Engineers*, *37*, 367–374. Translated from the Japanese by C. J. Lee in 1966, International Journal of Heat and Mass Transfer, 9, 1419-1433.

Park, J. Y., Min, C.-K., Granick, S., & Cahill, D. G. (2012). Residence Time and Heat Transfer When Water Droplets Hit a Scalding Surface. *Journal of Heat Transfer*, *134*, 101503.

Patience, G. S., Boffito, D. C., & Patience, P. A. (2013). *Writing a Scientific Paper: From Clutter to Clarity*. Elsevier Amsterdam.

Peterson, G. P., & Fletcher, L. S. (1990). Measurement of the thermal contact conductance and thermal conductivity of anodized aluminum coatings. *Journal of Heat Transfer*, *112*(3), 579 – 585.

Prosperetti, A., & Plesset, M. S. (1984). The stability of an evaporating liquid surface. *Physics of Fluids (1958-1988)*, *27*(7), 1590–1602.

Quéré, D. (2013). Leidenfrost dynamics. *Annual Review of Fluid Mechanics*, *45*(1), 197–215.

Roisman, I. V. (2009). Inertia dominated drop collisions. II. An analytical solution of the Navier-Stokes equations for a spreading viscous film. *Physics of Fluids*, *21*(5), 052104.

Roisman, I. V. (2010a). Fast forced liquid film spreading on a substrate: flow, heat transfer and phase transition. *Journal of Fluid Mechanics*, *656*, 189–204.

Roisman, I. V. (2010b). On the instability of a free viscous rim. *Journal of Fluid Mechanics*, *661*, 206–228.

Roisman, I. V., Gambaryan-Roisman, T., Kyriopoulos, O., Stephan, P., & Tropea, C. (2007). Breakup and atomization of a stretching crown. *Physical Review E*, *76*(2), 26302.

Roisman, I. V., Rioboo, R., & Tropea, C. (2002). Normal impact of a liquid drop on a dry surface: model for spreading and receding. *Proceedings of the Royal Society of London. Series A: Mathematical, Physical and Engineering Sciences*, *458*(2022), 1411–1430.

Royce, R. (1996). *The Jet Engine book: The Jet Engine - A complete overview of the modern gas turbine*. Rolls-Royce plc, Derby, England.

Schäfer, T. (2012). *Experimentelle Untersuchung des Leidenfrost-Effektes beim Aufprall von Einzeltropfen auf heisse Oberflächen unter erhöhtem Umgebungsdruck*. Bachelor thesis, Technische Universität Darmstadt.

Schindelin, J., Arganda-Carreras, I., Frise, E., Kaynig, V., Longair, M., Pietzsch, T., Preibisch, S., Rueden, C., Saalfeld, S., Schmid, B., Tinevez, J.-Y., White, D. J., Hartenstein, V., Eliceiri, K., Tomancak, P., & Cardona, A. (2012). Fiji: an open-source platform for biological-image analysis. *Nature Methods*, *9*(7), 676–682. Module: Auto Local Threshold.

Scriven, L. (1959). On the dynamics of phase growth. *Chemical Engineering Science*, *10*(1-2), 1–13.

Seo, M., Paquet, C., Nie, Z., Xu, S., & Kumacheva, E. (2007). Microfluidic consecutive flow-focusing droplet generators. *Soft Matter*, *3*, 986–992.

Sezgin, M., & Sankur, B. (2004). Survey over image thresholding techniques and quantitative performance evaluation. *Journal of Electronic Imaging*, *13*(1), 146–165.

Shamsundar, N., & Lienhard, J. H. (1993). Equations of state and spinodal lines - a review. *Nuclear Engineering and Design*, *141*(1-2), 269–287.

Shepherd, J., & Sturtevant, B. (1982). Rapid evaporation at the superheat limit. *Journal of Fluid Mechanics*, *121*, 379–402.

Shusser, M., & Weihs, D. (2001). Stability of rapidly evaporating droplets and liquid shells. *International Journal of Multiphase Flow*, *27*(2), 299 – 345.

Skripov, V. P., Sinitsyn, E. N., & Pavlov, P. A. (1980). *Thermal and Physical Properties of Liquids in the Metastable State*. Atomizdat, Moscow.

Spurk, J., & Aksel, N. (2007). *Strömungslehre*. Springer Heidelberg, 7 ed.

Stanglmaier, R. H., Roberts, C. E., & Moses, C. A. (2002). Vaporization of Individual Fuel Drops on a Heated Surface: A Study of Fuel-Wall Interactions within Direct-Injected Gasoline (DIG) Engines. Technical paper 2002-01-0838, SAE, Warrendale, PA, USA.

Stutz, B., & Simões-Moreira, J. R. (2013). Onset of boiling and propagating mechanisms in a highly superheated liquid - the role of evaporation waves. *International Journal of Heat and Mass Transfer*, *56*(1-2), 683–693.

Takashima, T., & Iida, Y. (1998). Process of vapor film collapse around hot liquid drops induced by an external pressure wave. *Transactions of the Japan Society of Mechanical Engineers. B*, *64*(623), 2266–2272. As referenced in wikimedia.org file Leidenfrost_temperature_NT.png.

Tappen, A. (2007). *Aluminium-Werkstoff-Datenblatt, EN AW-1050A, EN AW-Al 99.5*. Aluminium-Verlag Düsseldorf.

Temple-Pediani, R. (1969). Fuel drop vaporization under pressure on a hot surface. *Proceedings of the Institution of Mechanical Engineers*, *184*(1), 677–696. London.

Tran, T., Staat, H. J. J., Prosperetti, A., Sun, C., & Lohse, D. (2012). Drop Impact on Superheated Surfaces. *Physical Review Letters*, *108*, 036101.

Tran, T., Staat, H. J. J., Susarrey-Arce, A., Foertsch, T. C., van Houselt, A., Gardeniers, H. J. G. E., Prosperetti, A., Lohse, D., & Sun, C. (2013). Droplet impact on superheated micro-structured surfaces. *Soft Matter*, *9*, 3272–3282.

Tropea, C. (2011). Optical particle characterization in flows. *Annual Review of Fluid Mechanics*, *43*(1), 399–426.

Tropea, C., Yarin, L., & Foss, J. F. (Eds.) (2007). *Springer Handbook of Experimental Fluid Mechanics*. Springer Heidelberg. ISBN: 978-3-540-30299-5.

Vakarelski, I. U., Patankar, N. A., Marston, J. O., Chan, D. Y. C., & Thoroddsen, S. T. (2012). Stabilization of Leidenfrost vapour layer by textured superhydrophobic surfaces. *Nature*, *489*, 274–277.

VDI (2010). *VDI Heat Atlas*. Springer Düsseldorf, 2 ed.

Warren, S. G., & Wiscombe, W. J. (1980). A model for the spectral albedo of snow. II: Snow containing atmospheric aerosols. *Journal of the Atmospheric Sciences*, *37*(12), 2734–2745.

Wiscombe, W. J. (1980). Improved Mie scattering algorithms. *Applied Optics*, *19*(9), 1505–1509.

Wolff, E., & Schneider, D. (1998). Prediction of thermal contact resistance between polished surfaces. *International Journal of Heat and Mass Transfer*, *41*(22), 3469–3482.

Wolfram Research, I. (2010). *Mathematica v. 8.0.0*. Champaign, Illinois: Wolfram Research, Inc., Champaign, IL, USA.

Xcitex (2001). *MiDAS Lens Calculator v. 1.1.0.0*. Xcitex Inc., Cambridge, MA, USA.

Yarin, A. L. (2005). Drop impact dynamics: splashing, spreading, receding, bouncing... *Annual Review of Fluid Mechanics*, *38*(1), 159–192.

Ziegler, J. G., & Nichols, N. B. (1942). Optimum Settings for Automatic Controllers. *Transactions of the American Society of Mechanical Engineers*, *64*, 759–68. ULB Darmstadt signature Zb 508.

Ziegler, J. G., & Nichols, N. B. (1993). Optimum Settings for Automatic Controllers. *Journal of Dynamic Systems Measurement and Control*, *115*(2B), 220–222.

# Nomenclature

## Abbreviations

| | | |
|---|---|---|
| AC | alternating current | 41 |
| BLEVE | Boiling Liquid Expanding Vapor Explosion | 9 |
| DNB | departure from nucleate boiling | 15 |
| DOD | droplet-on-demand | 36 |
| FFT | fast Fourier transform | 92 |
| FPGA | field programmable gate array | 32 |
| LED | light emitting diode | 38 |
| LFP | Leidenfrost point at ambient pressure | 15 |
| ONB | onset of nucleate boiling | 21 |
| PID | proportional, integrative and derivative (closed-loop control) | 32 |
| ppm | parts per million, $10^{-6}$ | 40 |
| PWM | pulse width modulation | 42 |
| SFB-TRR 75 | Sonderforschungsbereich Transregio 75 | 103 |
| SI | The International System of Units | 95 |
| SMD | Sauter mean diameter | 96 |
| TNT | trinitrotoluene | 80 |
| TTL | transistor-transistor logic | 38 |

## Greek characters

## Latin characters

| | | |
|---|---|---|
| $a_s$ | speed of sound in solid in m/s | 28 |
| $A_{drop}$ | droplet contact area with wetted wall in $m^2$ | 65 |
| $Ar_*$ | Archimedes number in (Kutateladze, 1979) | 75 |
| $c$ | specific heat capacity in J/(kg K) | 13 |
| $D_0$ | initial diameter of the droplet in m | 26 |
| $D_b$ | bubble departure diameter in m | 74 |
| $D_{max}$ | droplet spread diameter in m | 65 |
| $e$ | thermal effusivity in (W $s^{0.5}$)/(K $m^2$) | 13 |
| $f\#$ | focal ratio | 51 |
| $g$ | free fall acceleration $g = 9.8081$ m/$s^2$ | 26 |
| $h_{ev}$ | latent heat of evaporation in J/kg | 19 |
| $hC$ | critical temperature of fluid hypothesis | 85 |
| $hF$ | flow hypothesis | 66 |
| $hH$ | homogeneous nucleation hypothesis | 23 |
| $hL$ | Landau instability hypothesis | 79 |
| $hM$ | Baumeister hypothesis | 70 |
| $hN$ | heterogeneous nucleation hypothesis | 66 |
| $hP$ | percolation hypothesis | 76 |
| $hS$ | saturation temperature hypothesis | 17 |
| $j$ | evaporative mass flux in kg/($m^2$ s) | 78 |
| $j_n$ | probability of homogeneous nucleation, $j_n \leq 2 \times 10^{-5}$ | 22 |
| $Ja$ | Jakob number $Ja = \frac{\rho_l}{\rho_v} \frac{c_{p,l}(T_{sat}-T_c)}{h_{ev}}$ | 75 |
| $k$ | Boltzmann constant, $k = 1.38065 \times 10^{-23}$ J/K | 22 |
| $K_c$ | controller gain in 1/K | 42 |

## List of Figures

## List of Equations

## List of Tables

# F Code Listings

## F.1 Image processing

```
//global variable holding waiting time (in millisec) for the wait
segments in the code
//in order to skip waiting just set the value of the variable to 0
var waitTime = 0;
//debugging flag indicator that is used for determination of which
data should
//be shown and/or saved in case the macro is executed for debug
purposes
var debugLevel = 4;
//global variable holding the list of desired file types that can be
processed
var fileTypes = ".tif,.tiff,.jpg,.png,.jpeg,.gif,.bmp";
//global variable indicating whether to use file type filtering
while building
//the list of files to be processed from the input directory
var useFileTypeFiltering = true;
//Variable representing the factor of reduction/scaling of the inner
rectangle containing the image
BlurrBorderReduction = 0.05;
//Gaussian blurring factor
gaussianBlurFactor = 0.025;
//the minimal area size (in pixels) of the particles we want to
include in out analysis,
//for example for particle area size of minimum 100 pixels and
higher set "minParticleSize = 100"
minParticleSize = 10;
macro "Thresholding Analysis"
{
    sourceDirectory = getDirectory("Choose Source Directory ");
    destinationDirectory = "";
    if(sourceDirectory != "")
    {
        destinationDirectory = getDirectory("Choose Destination
        Directory ");
        if(destinationDirectory == "")
        {
            print("Incorrect output directory choice, program
            termination was aborted!\n");
            exit();
        }
    }
    else
    {
        print("Incorrect input directory choice, program termination
        was aborted!\n");
        exit();
    }
```

```
    getDateAndTime(year, month, dayOfWeek, dayOfMonth, hour, minute,
    second, msec);
    outputResultsFileTimeStamp = "" + year + "_"  + (month+1) + "_"+
    dayOfMonth + "_" + hour + "_" + minute + "_" + second;
    outputResultsFileName = "resultsFile_" +
    outputResultsFileTimeStamp + ".csv";
    outputResultsFile = File.open(destinationDirectory +
    outputResultsFileName);
    print("STARTED: Execution Thresholding Analysis. START TIME: " +
    dayOfMonth + "-" + month + "-" + year + " at " + hour + ":" +
    minute + ":" + second);
    totalProcessedCnt = 0;
    totalPointsCnt = 0;
    dirList = getFullDirList(sourceDirectory);
    print(outputResultsFile, "Processed File Name" + ";" + "Area" +
    ";" + "Centroid X" + ";" + "Centroid Y" + ";" +
    "Horizontal-Max-Size");
    for (i=0; i<dirList.length; i++)
    {
        fileList = newArray(1);
        fileList[0] = 0;
        if(useFileTypeFiltering)
        {
            fileList = getFilesOnlyFilteredList(dirList[i], fileTypes
            );
        }
        else
        {
            fileList = getFilesOnlyFullList(dirList[i]);
        }
        call("java.lang.System.gc");
        if(fileList[0] != 0)
        {
            closeAllWindows();
            call("java.lang.System.gc");
            for (j=0; j<fileList.length ; j++)
            {
                currFileName = fileList[j];
                currResults = processImgWithTmplateFile(currFileName,
                fileList[0], destinationDirectory ,
                outputResultsFileTimeStamp);
                if(currResults != "")
                {
                    resultsArray = split(currResults, "$");
                    for(k=0; k < resultsArray.length; k++)
                    {
                        totalPointsCnt = totalPointsCnt + 1;
```

```
                        print(outputResultsFile , currFileName + ";"
                        + resultsArray[k]);
                    }
                }
                totalProcessedCnt++;
                call("java.lang.System.gc");
                call("java.lang.System.gc");
            }
        }
    }
    getDateAndTime(end_year, end_month, end_dayOfWeek, end_dayOfMonth
    , end_hour, end_minute, end_second, end_msec);
    print("FINISHED: Execution Thresholding Analysis. END TIME: " +
    end_dayOfMonth + "-" + (end_month+1) + "-" + end_year + " at " +
    end_hour + ":" + end_minute + ":" + end_second);
    print("TOTAL PROCESSED: " + totalProcessedCnt + " Files.\n
    Results are stored in the results file: " + outputResultsFileName
     + "\n\n");
}
function processImgWithTmplateFile(inputImagePath,
backgroundImagePath, dstDir, outTimeStamp)
{
    backgroundImageName = "backgroundTemplateImage";
    open(inputImagePath);
    fileName = File.getName(inputImagePath);
    setForegroundColor(0, 0, 0);
    wait(waitTime);
    run("Copy");
    wait(waitTime);
    run("Internal Clipboard");
    rename("CurrInputImg");
    run("8-bit");
    if(debugLevel == 5)
    {
            saveAs(".tif", dstDir + outTimeStamp + "_" + fileName +
            "_1_CurrInputImg");
            rename("CurrInputImg");
    }
    dispose(File.getName(inputImagePath));
    open(backgroundImagePath);
    run("Copy");
    run("Internal Clipboard");
    rename(backgroundImageName);
    dispose(File.getName(backgroundImagePath));
    selectWindow("CurrInputImg");
    imageDownSizeSymmetric("CurrInputImg");
    selectWindow(backgroundImageName);
```

```
    imageDownSizeSymmetric(backgroundImageName);
    if(debugLevel == 5)
    {
        selectWindow("CurrInputImg");
        saveAs(".tif", dstDir + outTimeStamp + "_" + fileName +
        "_2_CurrInputImgDownsized");
        rename("CurrInputImg");
    }
    if(debugLevel == 5)
    {
        selectWindow(backgroundImageName);
        saveAs(".tif", destinationDirectory + outputLogFileTimeStamp
        + "_" + File.getName(fileList[0]) + "_0_" +
        backgroundImageName);
        rename(backgroundImageName);
    }
    setPasteMode("Difference");
    selectWindow(backgroundImageName);
    run("Copy");
    selectWindow("CurrInputImg");
    run("Paste");
    run("Invert");
    setPasteMode("Copy");
    if(debugLevel == 5)
    {
            selectWindow("CurrInputImg");
            saveAs(".tif", dstDir + outTimeStamp + "_" + fileName +
            "_3_CurrInputImgMinusBack");
            rename("CurrInputImg");
    }
    selectWindow("CurrInputImg");
    run("Copy");
    run("Internal Clipboard");
    rename("CurrInputImg-1");
    dispose("CurrInputImg");
    selectWindow("CurrInputImg-1");
    run("Bandpass Filter...", "filter_large=51 filter_small=2
    suppress=None tolerance=5 autoscale saturate");
    run("Copy");
    run("Internal Clipboard");
    rename("CurrInputImg");
    selectWindow("CurrInputImg-1");
    setAutoThreshold("Otsu");
    run("Set Measurements...", "centroid area fit mean standard
    modal center bounding feret's stack display redirect=None
    decimal=5");
    run("Analyze Particles...", "size=" + minParticleSize +
```

```
    "-Infinity circularity=0.00-1.00 show=Nothing display exclude
    clear record add in_situ");
    roiManager("Show All with labels");
    selectWindow("CurrInputImg");
    rename("Analysis_Result");
    if(debugLevel >= 4)
    {
        if(nResults > 0)
        {
            selectWindow("Analysis_Result");
            roiManager("Show All with labels");
            run("Flatten");
            dispose("Analysis_Result");
            selectWindow("Analysis_Result-1");
            rename("Analysis_Result");
        }
        selectWindow("Analysis_Result");
        run("Select None");
        saveAs(".jpg", dstDir + outTimeStamp + "_" + fileName +
        "_4_Analysis_Result");
        rename("Analysis_Result");
    }
    analysisResults = "";
    if(nResults > 0)
    {
        headings = split(String.getResultsHeadings);
        for (row=0; row<nResults; row++)
        {
            analysisResults = analysisResults + getResult(headings[1
            ],row) + ";" + getResult(headings[5],row) + ";" +
            getResult(headings[6],row) + ";" + getResult(headings[11
            ],row) + "$";
        }
        analysisResults = replace(analysisResults, "\\.",",");
    }
    dispose(backgroundImageName);
    dispose("CurrInputImg-1");
    dispose("Results");
    dispose("Analysis_Result");
    dispose("ROI Manager");
    return analysisResults;
}
function dispose(title)
{
    if(isOpen(title))
    {
        selectWindow(title);
```

```
        run ("Close");
    }
 }
 function closeAllWindows()
 {
      while (nImages>0)
      {
          selectImage(nImages);
          close();
      }
  }
 function getFullDirList (dir) {
    list = getFileList(dir);
    fullList  = newArray(1);
    fullList[0]  = dir;
    for (i=0; i<list.length; i++)
    {
        tmp = dir + list[i];
        if (File.isDirectory(tmp))
        {
            tmp = replace(tmp, "/","\\");
            new_list  = getFullDirList (tmp);
            fullList  = concatenate_array (fullList, new_list);
        }
    }
    return fullList;
}
 function getFilesOnlyFullList (dir) {
     list = getFileList(dir);
    fullList  = newArray(1);
    for (i=0; i<list.length; i++)
    {
        tmp = dir + list[i];
        if (!File.isDirectory(tmp))
        {
            if (fullList[0] == 0)
            {
                fullList[0] = tmp;
            }
            else
            {
                fullList = append_to_array (tmp, fullList);
            }
        }
    }
    return fullList;
}
```

```
function getFilesOnlyFilteredList (dir, extensions)
{
   list = getFileList(dir);
   filteredList  = newArray(1);
   for (i=0; i<list.length; i++)
   {
       tmp = dir + list[i];
       if (!File.isDirectory(tmp) && isInTypeGroup(list[i],
       extensions))
       {
           if (filteredList[0] == 0)
           {
               filteredList[0] = tmp;
           }
           else
           {
               filteredList = append_to_array (tmp, filteredList);
           }
       }
   }
   return filteredList;
}
function getFullfileListRec (dir) {
  list = getFileList(dir);
  fullList  = newArray(1);
  for (i=0; i<list.length; i++)
  {
    tmp = dir + list[i];
    if (!File.isDirectory(tmp))
    {
      if (fullList[0] == 0)
      {
        fullList[0] = tmp;
      }
      else
      {
        fullList  = append_to_array (tmp, fullList);
      }
    }
    else
    {
      new_list  = getFullfileListRec (tmp);
      if (fullList[0] == 0)
      {
        fullList  = new_list;
      }
      else
```

```
      {
          if (!(new_list.length == 1 && new_list[0] == 0))
          {
            fullList  = concatenate_array (fullList, new_list);
          }
      }
    }
  }
  return fullList;
}
function isInTypeGroup(fileName, extensions)
{
    isInGroup = false;
    extArr = split(extensions,",");
    for(i = 0; i < extArr.length && isInGroup == false; i++)
    {
        isInGroup = endsWith(fileName, extArr[i]);
    }
    return isInGroup;
}
function getFilteredFileListRec(dir, extensions)
{
     list = getFileList(dir);
     filteredList  = newArray(1);
    for (i=0; i<list.length; i++)
    {
        tmp = dir + list[i];
        if (isInTypeGroup(list[i], extensions))
        {
          if (filteredList[0] == 0)
          {
            filteredList[0] = tmp;
          }
          else
          {
            filteredList = append_to_array (tmp, filteredList);
          }
        }
        else if (File.isDirectory(tmp))
        {
          new_list  = getFilteredFileListRec (tmp, extensions);
          if (filteredList[0] == 0)
          {
            filteredList  = new_list;
          } else if (new_list.length == 1 && new_list[0] == 0)
          {
          } else
```

```
          {
            filteredList  = concatenate_array (filteredList, new_list
            );
          }
        } else
        {
          // do nothing, not the right file type
        }
     }
      return filteredList;
}
function imgToNewArray(width, height)
{
    totalSize = width * height;
    pixelArr = newArray(totalSize);
    for(y = 0; y < height; y++)
    {
        for(x = 0; x < width; x++)
        {
            pixelArr[x + y*width] = getPixel(x, y);
        }
    }
    return pixelArr;
}
function copyImgToArray(width, height, dstArr)
{
    if(debugLevel == 6)
    {
        for(y = 0; y < height; y++)
        {
            for(x = 0; x < width; x++)
            {
                dstArr[x + y*width] = getPixel(x, y);
            }
            print("CopyImgToArray:" + dstArr[y*width] + ";" +
            getPixel(0, y) + "\n");
        }
    }
    else
    {
        for(y = 0; y < height; y++)
        {
            for(x = 0; x < width; x++)
            {
                dstArr[x + y*width] = getPixel(x, y);
            }
        }
```

```
    }
    return dstArr;
}
function addImgToArray(width, height, dstArr)
{
    for(y = 0; y < height; y++)
    {
        for(x = 0; x < width; x++)
        {
            dstArr[x + y*width] = dstArr[x + y*width] + getPixel(x, y
            );
        }
    }
    return dstArr;
}
function arrayToImage(width, height, srcArr, dstImgName)
{
    selectWindow(dstImgName);
    for(y = 0; y < height; y++)
    {
        for(x = 0; x < width; x++)
        {
            setPixel(x, y, srcArr[x + y*width]);
        }
    }
}
function calcAvgArray(width, height, dstArr, divFactor)
{
    totalSize = width * height;
    if(divFactor > 1)
    {
        if(debugLevel == 6)
        {
            print("\n");
            for(i = 0; i < totalSize; i++)
            {
                dstArr[i] = dstArr[i] / divFactor;
                if((i % width) == 0)
                {
                    print(dstArr[i] + " ; ");
                }
            }
        }
        else
        {
            for(i = 0; i < totalSize; i++)
            {
```

```
                dstArr[i] = dstArr[i] / divFactor;
            }
        }
    }
    return dstArr;
}
function imageDownSizeSymmetric(imgName)
{
    selectWindow(imgName);
    imgHeight = getHeight();
    imgWidth = getWidth();
    if(imgHeight != imgWidth)
    {
        if(imgHeight > imgWidth)
        {
            run("Canvas Size...", "width=" + imgWidth + " height=" +
            imgWidth + " position=Center zero");
            imgHeight = imgWidth;
        }
        else
        {
            run("Canvas Size...", "width=" + imgHeight + " height=" +
             imgHeight + " position=Center zero");
            imgWidth = imgHeight;
        }
    }
    return imgHeight;
}
function open_ID (filename) {
  open(filename);
  ID = getImageID();
  return ID;
}
function close_by_ID(ID) {
  selectImage(ID);
  close();
}
function get_cleansed_file_list (dir, extension) {
  list      = getFileList(dir);
  cleansed  = newArray(1);
  for (i=0; i<list.length; i++)
  {
    tmp = dir + list[i];
    if (endsWith(list[i], extension))
    {
      if (cleansed[0] == 0)
      {
```

```
        cleansed[0] = tmp;
      }
      else
      {
        cleansed    = append_to_array (tmp, cleansed);
      }
    } else if (File.isDirectory(tmp))
    {
      new_list  = get_cleansed_file_list (tmp, extension);
      if (cleansed[0] == 0)
      {
        cleansed  = new_list;
      } else if (new_list.length == 1 && new_list[0] == 0)
      {
        // do nothing, this directory had no good file and appending
        it will
        // append a zero to the list
      } else
      {
        cleansed  = concatenate_array (cleansed, new_list);
      }
    } else
    {
      // do nothing, not the right file type
    }
  }
  return cleansed;
}
function concatenate_array (array1, array2)
{
  length_1  = lengthOf(array1);
  length_2  = lengthOf(array2);
  new = newArray(length_1 + length_2);
  for (i=0; i<length_1; i++)
  {
    new[i] = array1[i];
  }
  for (i=0; i<length_2; i++)
  {
    new[length_1 + i] = array2[i];
  }
  return new;
}
function remove_from_array (array, index)
{
  length  = lengthOf(array);
  new     = newArray(length - 1);
```

```
  for (i=0; i<index; i++)
  {
    new[i] = array[i];
  }
  for (i=(index+1); i<length; i++)
  {
    new[i] = array[i];
  }
  return new;
}
function add_to_array (value, array, position)
{
  ori_length = lengthOf(array);
  if (position < ori_length)
  {
    array[position] = value;
    return array;
  }
  else
  {
    new = newArray(position + 1);
    for (i=0; i<ori_length; i++)
    {
      new[i] = array[i];
    }
    new[position] = value;
    return new;
  }
}
function append_to_array (value, array)
{
  ori_length  = lengthOf(array);
  new  = newArray(ori_length + 1);
  for (i=0; i<ori_length; i++)
  {
    new[i] = array[i];
  }
  new[ori_length] = value;
  return new;
}
```

## F.2 Optical calculations

Figure F.1 illustrates the optical calculations tool (Xcitex, 2001) used in the experiment setup. The current exposure time in the experiment is set by the illumination. It is ten times lower than on the figure along with the ten times smaller motion blur.

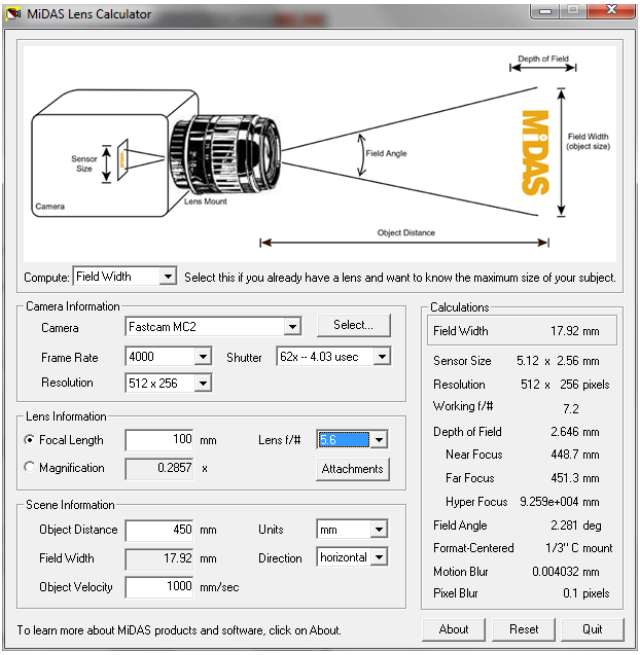


**Figure F.1.:** Lens calculator window

## F.3 Landau instability

Landau1986r calculation. Ilja Buchmüller, January 2014.

In[1]:=
```
eq9c = Ω^2 (v1 + v2) + 2 Ω k v1 v2 + (k^2 (v1 - v2) + (g k (ρ1 - ρ2) + α1 k^3) / j ) v1 v2 == 0
```

Out[1]=
$$v1\ v2\left(k^2\ (v1-v2)+\frac{k^3\,\alpha1+g\,k\,(\rho1-\rho2)}{j}\right)+2\,k\,v1\,v2\,\Omega+(v1+v2)\,\Omega^2==0$$

In[2]:=
```
sol = Solve[eq9c, Ω] // Simplify
```

Out[2]=
$$\left\{\left\{\Omega\to-\frac{j\,k\,v1\,v2+\sqrt{-j\,k\,v1\,v2\,\left(j\,k\,\left(v1^2-v1\,v2-v2^2\right)+(v1+v2)\,\left(k^2\,\alpha1+g\,(\rho1-\rho2)\right)\right)}}{j\,(v1+v2)}\right\},\right.$$
$$\left.\left\{\Omega\to\frac{-j\,k\,v1\,v2+\sqrt{-j\,k\,v1\,v2\,\left(j\,k\,\left(v1^2-v1\,v2-v2^2\right)+(v1+v2)\,\left(k^2\,\alpha1+g\,(\rho1-\rho2)\right)\right)}}{j\,(v1+v2)}\right\}\right\}$$

In[3]:=
```
ev = Evaluate[Ω] /. sol
```

Out[3]=
$$\left\{-\frac{j\,k\,v1\,v2+\sqrt{-j\,k\,v1\,v2\,\left(j\,k\,\left(v1^2-v1\,v2-v2^2\right)+(v1+v2)\,\left(k^2\,\alpha1+g\,(\rho1-\rho2)\right)\right)}}{j\,(v1+v2)},\right.$$
$$\left.\frac{-j\,k\,v1\,v2+\sqrt{-j\,k\,v1\,v2\,\left(j\,k\,\left(v1^2-v1\,v2-v2^2\right)+(v1+v2)\,\left(k^2\,\alpha1+g\,(\rho1-\rho2)\right)\right)}}{j\,(v1+v2)}\right\}$$

In[4]:=
```
(ev[[1]] + ev[[2]]) / 2 // Simplify
```

Out[4]=
$$-\frac{k\,v1\,v2}{v1+v2}$$

In[5]:=
```
alt = (-ev[[1]] + ev[[2]]) / 2 // Simplify
```

Out[5]=
$$\frac{\sqrt{-j\,k\,v1\,v2\,\left(j\,k\,\left(v1^2-v1\,v2-v2^2\right)+(v1+v2)\,\left(k^2\,\alpha1+g\,(\rho1-\rho2)\right)\right)}}{j\,(v1+v2)}$$

In[6]:=
```
root = (alt * (j (v1 + v2)))^2 /. v2 → v1 * ρ1 / ρ2 // Simplify
```

Out[6]=
$$\frac{j\,k\,v1^3\,\rho1\,\left(-\left(k^2\,\alpha1+g\,(\rho1-\rho2)\right)\,\rho2\,(\rho1+\rho2)+j\,k\,v1\,\left(\rho1^2+\rho1\,\rho2-\rho2^2\right)\right)}{\rho2^3}$$

Ilja Buchmüller: root > 0 means the interface gets (bi -) unstable.

In[7]:=
```
sol3 =
 Reduce[{root > 0, ρ1 > ρ2 > 0, v1 > 0,  α1 > 0, k > 0 , j > 0}, j, Reals] // Simplify
```

Out[7]=
$$\left(g>-\frac{k^2\,\alpha1}{\rho1-\rho2}\ ||\ j>0\right)\ \&\&\ \left(g\le-\frac{k^2\,\alpha1}{\rho1-\rho2}\ ||\ j>\frac{\left(k^2\,\alpha1+g\,(\rho1-\rho2)\right)\,\rho2\,(\rho1+\rho2)}{k\,v1\,\left(\rho1^2+\rho1\,\rho2-\rho2^2\right)}\right)\ \&\&$$
$$k>0\ \&\&\ v1>0\ \&\&\ \alpha1>0\ \&\&\ \rho1>\rho2\ \&\&\ \rho2>0$$

In[8]:=
```
sol5 = sol3[[1]][[1]] /. (ρ1 - ρ2) → Δρ
```

Out[8]=
$$g>-\frac{k^2\,\alpha1}{\Delta\rho}$$

Bond number has a height and a sphere radius, here R^2. Vapor density effect is $\Delta\rho$ for Bo.

In[9]:= **Bo == Δρ g R^2 / α1**

Out[9]= $Bo == \frac{g\, R^2\, \Delta\rho}{\alpha 1}$

In[10]:= **eqBo = g -> Bo α1 / (Δρ R^2)**

Out[10]= $g \to \frac{Bo\, \alpha 1}{R^2\, \Delta\rho}$

In[11]:= **Simplify[sol5 /. eqBo, {Δρ > 0, α1 > 0, k > 0, R > 0 }]**

Out[11]= $Bo + k^2\, R^2 > 0$

as $k^2\, R^2 \to 1$ this means $Bo > -1$. Therefore,
if gravity is inversed and is higher than surface tension, the interace produces droplets, a well known result. The evaporation driven instability has the onset criterium

In[12]:= **sol6 = sol3[[2]][[2]]**

Out[12]= $j > \frac{\left(k^2\, \alpha 1 + g\, (\rho 1 - \rho 2)\right)\, \rho 2\, (\rho 1 + \rho 2)}{k\, v1\, \left(\rho 1^2 + \rho 1\, \rho 2 - \rho 2^2\right)}$

(v1 implicite)

In[13]:= **sol6 = sol3[[2]][[2]] /. v1 -> j / ρ1**

Out[13]= $j > \frac{\rho 1\, \left(k^2\, \alpha 1 + g\, (\rho 1 - \rho 2)\right)\, \rho 2\, (\rho 1 + \rho 2)}{j\, k\, \left(\rho 1^2 + \rho 1\, \rho 2 - \rho 2^2\right)}$

In[14]:= **sol7 = Reduce[{sol6, ρ1 > ρ2 > 0, α1 > 0, k > 0 , j > 0}, j, Reals] // Simplify**

Out[14]= $\left(g > -\frac{k^2\, \alpha 1}{\rho 1 - \rho 2} \;||\; j > 0\right) \&\& \left(g \le -\frac{k^2\, \alpha 1}{\rho 1 - \rho 2} \;||\; j > \sqrt{\frac{\rho 1\, \left(k^2\, \alpha 1 + g\, (\rho 1 - \rho 2)\right)\, \rho 2\, (\rho 1 + \rho 2)}{k\, \left(\rho 1^2 + \rho 1\, \rho 2 - \rho 2^2\right)}}\right) \&\&$

$k > 0 \&\& \alpha 1 > 0 \&\& \rho 1 > \rho 2 \&\& \rho 2 > 0$

In[15]:= **sol8 = sol7[[2]][[2]]**

Out[15]= $j > \sqrt{\frac{\rho 1\, \left(k^2\, \alpha 1 + g\, (\rho 1 - \rho 2)\right)\, \rho 2\, (\rho 1 + \rho 2)}{k\, \left(\rho 1^2 + \rho 1\, \rho 2 - \rho 2^2\right)}}$

(sol8b is neclecting gravity, k≥1)

**sol8b = sol7[[2]][[2]] /. g → 0 /. k → 1**

$j > \sqrt{\frac{\alpha 1\, \rho 1\, \rho 2\, (\rho 1 + \rho 2)}{\rho 1^2 + \rho 1\, \rho 2 - \rho 2^2}}$

Prosperetti1984 material equation (Hertz-Knudsen), evaporation factor $\alpha$ taken as 1.

eq12 = j == α $\sqrt{(R\, Ts / (2\, \pi\, M))}$ (ρveTs − ρv)

In[16]:=
```
eq12 = j -> αz √(R Tc / (2 π M)) (ρveTc - ρ2)
```

Out[16]=
$$j \to \frac{\sqrt{\frac{R\,Tc}{M}}\ \alpha z\ (-\rho 2 + \rho veTc)}{\sqrt{2\,\pi}}$$

In[17]:=
```
sol8 /. eq12
```

Out[17]=
$$\frac{\sqrt{\frac{R\,Tc}{M}}\ \alpha z\ (-\rho 2 + \rho veTc)}{\sqrt{2\,\pi}} > \sqrt{\frac{\rho 1\ \left(k^2\,\alpha 1 + g\ (\rho 1 - \rho 2)\right)\ \rho 2\ (\rho 1 + \rho 2)}{k\ \left(\rho 1^2 + \rho 1\,\rho 2 - \rho 2^2\right)}}$$

In[18]:=
```
sol9 = Reduce[{sol8 /. eq12, ρ1 > ρveTc > ρ2 > 0,
    α1 > 0, k > 0 , M > 0, R > 0, Tc > 0, αz > 0}, Tc, Reals] // Simplify
```

Out[18]=
$$\rho 2 > 0\ \&\&\ \rho 1 > \rho 2\ \&\&\ \rho 2 < \rho veTc < \rho 1\ \&\&\ \alpha z > 0\ \&\&\ \alpha 1 > 0\ \&\&$$
$$R > 0\ \&\&\ M > 0\ \&\&\ k > 0\ \&\&\ \left(\left(Tc > 0\ \&\&\ \rho 1 \neq \rho 2\ \&\&\ k^2\,\alpha 1 + g\,\rho 1 == g\,\rho 2\right)\ ||\right.$$
$$\left.\left(g > -\frac{k^2\,\alpha 1}{\rho 1 - \rho 2}\ \&\&\ Tc > \frac{2\,M\,\pi\,\rho 1\ \left(k^2\,\alpha 1 + g\ (\rho 1 - \rho 2)\right)\ \rho 2\ (\rho 1 + \rho 2)}{k\,R\,\alpha z^2\ \left(\rho 1^2 + \rho 1\,\rho 2 - \rho 2^2\right)\ (\rho 2 - \rho veTc)^2}\right)\right)$$

In[19]:=
```
sol10 = sol9[[9]][[2]][[2]]
```

Out[19]=
$$Tc > \frac{2\,M\,\pi\,\rho 1\ \left(k^2\,\alpha 1 + g\ (\rho 1 - \rho 2)\right)\ \rho 2\ (\rho 1 + \rho 2)}{k\,R\,\alpha z^2\ \left(\rho 1^2 + \rho 1\,\rho 2 - \rho 2^2\right)\ (\rho 2 - \rho veTc)^2}$$

In[20]:=
```
sol11 = sol10 /. α1 → σliq /. ρ1 → ρliq /. ρ2 → ρvap /. αz → 1
```

Out[20]=
$$Tc > \frac{2\,M\,\pi\,\rho liq\,\rho vap\ (\rho liq + \rho vap)\ \left(g\ (\rho liq - \rho vap) + k^2\,\sigma liq\right)}{k\,R\ \left(\rho liq^2 + \rho liq\,\rho vap - \rho vap^2\right)\ (\rho vap - \rho veTc)^2}$$

What is the wave number k for minimum Tc?

In[22]:=
```
sol12 =
 Reduce[{D[sol10[[2]], k] == 0, D[sol10[[2]], {k, 2}] > 0, ρ1 > ρveTc > ρ2 > 0, α1 > 0,
     k > 0 , M > 0, R > 0, Tc > 0, αz > 0},
   k, Reals] /. α1 → σliq /. ρ1 → ρliq /. ρ2 → ρvap
```

Out[22]=
$$\rho vap > 0\ \&\&\ \rho liq > \rho vap\ \&\&\ \rho vap < \rho veTc < \rho liq\ \&\&\ \alpha z > 0\ \&\&$$
$$\sigma liq > 0\ \&\&\ Tc > 0\ \&\&\ R > 0\ \&\&\ M > 0\ \&\&\ g > 0\ \&\&\ k == \sqrt{\frac{g\,\rho liq - g\,\rho vap}{\sigma liq}}$$

In[23]:=
```
sol12[[10]]
```

Out[23]=
$$k == \sqrt{\frac{g\,\rho liq - g\,\rho vap}{\sigma liq}}$$

The wave number k for minimum Tc is dependent on g, contraintuitively, but here g is binding the fluid densities measured under earth surface conditions to the inertial forces on the volume. In this way k shows the balance of inertial forces and surface tension.

In[29]:=
```
sol11 /. k → sol12[[10]][[2]] // Simplify
```

Out[29]=
$$Tc > \frac{4\,M\,\pi\,\rho liq\,\rho vap\,(\rho liq+\rho vap)\,\sqrt{\frac{g\,(\rho liq-\rho vap)}{\sigma liq}}\;\sigma liq}{R\left(\rho liq^2+\rho liq\,\rho vap-\rho vap^2\right)(\rho vap-\rho veTc)^2}$$

k for fastest growing :

In[39]:=
```
sol13 = Ω /. sol[[1]]  /. v2 → v1 * ρ1 / ρ2  /. v1 -> j / ρ1 /. eq12 /. αz → 1 // Simplify
```

Out[39]=
$$\left(M\left(k\left(\frac{R\,Tc}{M}\right)^{3/2}(\rho2-\rho veTc)^3-\rho1\,\rho2\,\sqrt{\left(-1\Big/\left(M^3\,\rho1^3\,\rho2^3\right)k\,R^2\,Tc^2\left(2\,k^2\,M\,\pi\,\alpha1\,\rho1\,\rho2\,(\rho1+\rho2)+2\,g\,M\,\pi\,\rho1\,\rho2\left(\rho1^2-\rho2^2\right)-k\,R\,Tc\left(\rho1^2+\rho1\,\rho2-\rho2^2\right)(\rho2-\rho veTc)^2\right)\right.}\left.(\rho2-\rho veTc)^4\right)\right)\Big/\left(\sqrt{2\,\pi}\;R\,Tc\,(\rho1+\rho2)\,(\rho2-\rho veTc)^2\right)$$

In[40]:=
```
D[sol13, k] // Simplify
```

Out[40]=
$$\frac{1}{\sqrt{2\,\pi}\;R\,Tc\,(\rho1+\rho2)}$$
$$M\left(\left(\frac{R\,Tc}{M}\right)^{3/2}+\left(R^2\,Tc^2\left(3\,k^2\,M\,\pi\,\alpha1\,\rho1\,\rho2\,(\rho1+\rho2)+g\,M\,\pi\,\rho1\,\rho2\left(\rho1^2-\rho2^2\right)-k\,R\,Tc\left(\rho1^2+\rho1\,\rho2-\rho2^2\right)(\rho2-\rho veTc)^2\right)\Big/\left(M^3\,\rho1^2\,\rho2^2\right.\right.\right.$$
$$\left.\left.\left.\sqrt{\left(-1\Big/\left(M^3\,\rho1^3\,\rho2^3\right)k\,R^2\,Tc^2\left(2\,k^2\,M\,\pi\,\alpha1\,\rho1\,\rho2\,(\rho1+\rho2)+2\,g\,M\,\pi\,\rho1\,\rho2\left(\rho1^2-\rho2^2\right)-k\,R\,Tc\left(\rho1^2+\rho1\,\rho2-\rho2^2\right)(\rho2-\rho veTc)^2\right)(\rho2-\rho veTc)^4\right)}\right)\right)(\rho2-\rho veTc)$$

In[41]:=
```
D[sol13, {k, 2}] // Simplify
```

Out[41]=
$$-\left(\sqrt{\frac{\pi}{2}}\;R^3\,Tc^3\left(3\,k^4\,M\,\pi\,\alpha1^2\,\rho1\,\rho2\,(\rho1+\rho2)-g^2\,M\,\pi\,\rho1\,(\rho1-\rho2)^2\,\rho2\,(\rho1+\rho2)+6\,g\,k^2\,M\,\pi\,\alpha1\,\rho1\,\rho2\left(\rho1^2-\rho2^2\right)-2\,k^3\,R\,Tc\,\alpha1\left(\rho1^2+\rho1\,\rho2-\rho2^2\right)(\rho2-\rho veTc)^2\right)(\rho2-\rho veTc)^6\right)\Big/$$
$$\left(M^4\,\rho1^4\,\rho2^4\left(-1\Big/\left(M^3\,\rho1^3\,\rho2^3\right)k\,R^2\,Tc^2\left(2\,k^2\,M\,\pi\,\alpha1\,\rho1\,\rho2\,(\rho1+\rho2)+2\,g\,M\,\pi\,\rho1\,\rho2\left(\rho1^2-\rho2^2\right)-k\,R\,Tc\left(\rho1^2+\rho1\,\rho2-\rho2^2\right)(\rho2-\rho veTc)^2\right)(\rho2-\rho veTc)^4\right)^{3/2}\right)$$

In[43]:=
```
sol14 =
 Reduce[{D[sol13, k] == 0, D[sol13, {k, 2}] > 0, ρ1 > ρveTc > ρ2 > 0,  α1 > 0, k > 0 ,
       M > 0,  R > 0,  Tc > 0, αz > 0}, k,  Reals] /. α1 → σliq /. ρ1 → ρliq /. ρ2 → ρvap
```

Out[43]=
```
$Aborted
```

**Ilja Buchmüller**
Diplom Wirtschaftsingenieur
(Maschinenbau) / M. Sc.
e-mail: ilja.buchmueller@gmail.com

## Work Experience

*02.2010 - 12.2013* *Institute for Fluid Mechanics and Aerodynamics, TU Darmstadt*
Researched the influence of pressure on water droplets impinging on a heated wall as part of the SFB-TRR 75. Taught practical applications of Measurement Techniques to undergraduate students

*04.2009 - 02.2010* *Vogel Druck & Medienservice GmbH, Höchberg*
Designed innovative automated robotic unit for handling printed media

*11.2008 - 04.2009* *Institute for Fluid Mechanics and Aerodynamics, TU Darmstadt*
Responsible for pre-processing and pre-analysis of experimental results

*03.2006 - 01.2007* *BoschRexroth AG, Lohr am Main*
Completed internship, followed by part time employment

*12.2003 - 03.2008* *Freelance consultancy in Robotics*
Designed, produced and commissioned robotic arms for international clients

*03.2004 - 06.2004* *Institute for Product Development and Machine Elements, TU Darmstadt*
Organized and coordinated "International Design Contest 2004", Germany

*06.2001 - 10.2001* *Kurtz Holding GmbH & Co. KG, Kreuzwertheim*
Completed technical internship in all stages of production and assembly

## Education

*02.2010 - present* *Technical University of Darmstadt, Germany*
Pursuing PhD in Mechanical Engineering

*10.2003 - 03.2009* *Technical University of Darmstadt, Germany*
Completed Diplom Wirtschaftsingenieurwesen - Maschinenbau
with studies in *St. Petersburg University of Economy and Finance, Russia* and *Pontificia Universidad Catolica Argentina S. M. d. l. Buenos Aires*

*10.2001 - 09.2003* *Technical University of Darmstadt, Germany*
Achieved Vordiplom in Wirtschaftsingenieurwesen - Maschinenbau

*05.1996 - 06.2001* *Friedrich-Koenig-Gymnasium in Würzburg*
Completed schooling with Abitur, major in Physics and Mathematics

## Achievements

* Received, "*ZARM Förderpreis"* from University of Bremen in 2009
* Finalist in, "*CEO of the Future"* competition from McKinsey in 2008
* Awarded, "*e-fellows.net grant"* in 2008
* Selected through the, "*International Design Contest"* to represent Germany at the "*RoboCon"* robot competition in Nagoya, Japan in 2003
* First winner in the, "*Stahl fliegt!"* contest for aircraft models in 2002
* Won the, "*TUMMS"* grant from TU München in 2000

## Technical Skills

* Advanced knowledge of CAD/CAM, including AutoCAD, UG NX, CATIA
* Solid knowledge of bash, C, FPGAs, LabVIEW, Matlab, µC's and VBA
* Administrative knowledge of LINUX, MS Windows, IP Networks
* Certified on, "Boiling Heat Transfer and Boiling Equipment"
* Certified on, "Optics Design with Zemax"
* Certified Class A Amateur Radio Operator